



Bioinspired Nanocomposites: Materials for the Regeneration and Tissue Engineering of Bone

Promotionsschrift

zur Erlangung des akademischen Grades

Doktor-Ingenieur (Dr. -Ing.)

vorgelegt der

**Zentrum für Ingenieurwissenschaften
der Martin-Luther-Universität Halle-Wittenberg**

von

Herrn M.Sc. Imam Khasim Hadimani Rajasaheb

geb. am 17.10.1977 in Ilkal (India)

Gutachter:

1- Prof. Dr. rer. nat. habil. Goerg H. Michler (Halle/Saale)

2- Prof. Dr.-Ing. Birgit Glasmacher (Hannover)

Halle (Saale), 19 January 2012

DEDICATED
TO
MY SISTER

Acknowledgements

With the expansion of the international relations, the world is becoming smaller and concern for developing countries is growing. The Developed countries, including Germany, which had produced many earliest thinkers of the world in almost every area of knowledge, have been receiving students from the developing countries, training them in the latest scientific skills and thereby contributing to the human resource development of these countries. In the present context, Germany has lent her helping hand to India by selecting me for advanced courses (MSc and PhD) in engineering, for which I am deeply indebted to Germany. In particular, the oldest and prestigious Martin-Luther University, Halle Wittenberg deserves to be profusely thanked for registering me as a doctoral student.

While receiving higher education within the country itself is sometimes unaffordable to the weaker sections of the country, receiving such education in the intellectual climate of Germany is just not possible for them. But the Translational Centre for Regenerative Medicine (TRM), Leipzig and BMBF have made it possible by giving me financial assistance (Stipendium) for doing PhD. I express my heart-felt thanks to both for this kind of gesture.

Headless family and teacherless students have no proper destiny. I was the most fortunate to have become a student of Prof G.H. Michler, so great scholar and distinguished professor, whose unstinted personal care, continuous encouragement and thought-provoking guidance at every stage of my research, have stood by me in all critical moments of my stay and education in Germany. I respectfully, remember him with all gratitude.

I deem it a great pleasure and rare privilege to express my cordial gratitude to Dr. Sven Henning for his guidance, persistent interest, skilled advice and patience throughout my research work. His affectionate behaviour, useful discussions and suggestions were of great help in completing my research work timely. He has helped me in every step of my work from the beginning to the end, in planning the experimental part, discussing and interpreting the results and also in writing the thesis. He had also helped me in other problems of my stay in Halle. His endless support and instructive discussions are sincerely acknowledged.

I have been accompanied and supported by many others in my research work. Now comes the pleasant moment to express my gratitude to all of them. I would like to record my appreciation to Dr. Joerg Brandt for helping me to carry out cell culture experiments even with his busy schedule

I also thank Ashraf for his support both in academics as well as in personal matter. I stood with me like a brother. Without him, it was very difficult for me to finish my degree. I would

like to show my appreciation to Dr. G.M. Kim for teaching electrospinning, which is one of its kind and his guidance in understanding the concept of electrospinning. I wish to acknowledge Dr. Reinhold Godehardt, Mr. Werner Lebek, Ms. Cornelia Becker, Ms Sylvia Goerlitz, Ms Stefanie Scholtyssek, Mr. Volker Seydewitz, Dr. Rameshwar Adhikari and other staff in Allgemeine Werkstoffwissenschaften for their support throughout my thesis.

I would also acknowledge Prof. Thomas Groth for constantly helping me in the PhD work by providing me with many facilities. I would also like to acknowledge Herr. Wolfgang Schurz and Ms Birgit Erfurt for their support. Also, I thank Dr. Ralf Lach for helping me in giving me an opportunity to do microhardness measurements.

Additionally I thank Dr. Andre Wutzler for his help in DSC experiments, tensile testing and many other experiments.

I would like to thank all my family members and well wishers especially my parents and my brother in India. Their endless love and instructions led to the PhD in engineering. I want to thank my wife, Fouziya, for her love and support. Finally I would like to express my special thanks to all Indians in Halle for their continuous support during my stay in germany.

Declaration

I certify that this work has been entirely carried out by myself. I undertake that all the material presented in the PhD thesis is my own work and has not been written for me, in whole or in part, by any other person. I also undertake that any quotation or paraphrase from the published or unpublished work of another person has been duly acknowledged in the work.

Halle (Saale)

Date: 26/01/2012

Imam Khasim Hadimani Rajasaheb

TABLE OF CONTENT

Acknowledgements	iii
List of Abbreviations	ix
1. Introduction.....	1
2. Basics.....	4
2.1 Materials for bone replacement and bone tissue engineering	4
2.1.1 Requirements and strategies for bone tissue engineering	5
2.1.2 Selection criteria for materials in bone tissue engineering	7
2.1.3 Bone replacement materials: State of art	9
2.2 Semi Crystalline Polymers.....	24
2.2.1 Morphology, mechanical properties and micromechanics of semicrystalline polymers	25
2.2.2 Biodegradable semicrystalline polymers	27
2.2.3 Polyhydroxybutyrate	28
2.2.4 Hydroxyapatite.....	29
2.3 Nanocomposites.....	32
2.3.1 Bone as a model nanocomposite.....	32
2.3.2 Particulate filled polymer nanocomposites	35
2.3.3 Transition from micro to nanoparticles.....	35
2.3.4 Biomimetic nanocomposite – A new approach	37
2.3.5 Hybrid nanofibers	38
3 Materials and Methods.....	40
3.1 Materials	40
3.1.1 Polymers	40
3.1.2 Nanoparticles	40
3.1.3 Chemicals and auxiliary materials	40
3.2 Fabrication of Materials.....	41
3.2.1 Synthesis of Biomimetic hydroxyapatite	41
3.2.2 Preparation of simulated body fluid.....	42
3.2.3 Synthesis of nano-hydroxyapatite by wet chemical method.....	42
3.2.4 Preparation of nanocomposites	43

3.2.5 Preparation of porous films by immersion precipitation	43
3.2.6 Preparation of porous structures by freeze drying and particulate leaching	44
3.2.7 Preparation of porous scaffolds using melt infiltration technique	45
3.2.8 Preparation of nanofibers via electrospinning	45
3.3 Methods	47
3.3.1 Microscopy	47
3.3.2 Thermal analysis (DSC).....	50
3.3.3 Mechanical testing	50
3.3.5 Micromechanical analysis.....	51
3.3.6 Surface characterization: Contact Angle.....	52
3.3.7 Cell culture tests.....	53
4 Results and Discussion.....	57
4.1 Morphology of nanoparticles.....	57
4.1.1 Morphology of nanoparticles from chemical precipitation process.....	57
4.1.2 Morphology of nanoparticles from Wet precipitation process	60
4.2 Dispersion	61
4.2.1 Dispersion of nanoparticles in polymer matrix.....	61
4.2.2 Effect of Dispersion on filler content.....	62
4.3 Morphology of nanocomposites	64
4.3.1 Defects in spherulites.....	65
4.3.2 Deformation in PHB spherulites.....	68
4.3.3Morphology of Spherulites	70
4.4 Differential Scanning Calorimetry.....	75
4.4.1 Nonisothermal melt crystallization behaviour of PHBHV/HA nanocomposites	75
4.4.2 Nonisothermal Crystallization kinetics.....	79
4.4.3 Avrami analysis	82
4.4.4 Ozawa analysis.....	84
4.5 Mechanical Properties.....	85
4.5.1 Correlation to Halpin-Tsai Model.....	87
4.6 Micromechanical Deformation Processes of nanocomposites	93
4.7 Microhardness.....	97
4.8 Contact Angle	103
4.9 Cell Culture.....	106
4.9.1 Cell adhesion and morphology of MG-63 cells.....	106

4.9.2 Evaluation of Cell Proliferation	109
4.9.3 Cell adhesion and morphology of primary osteoblast cells	113
4.9.4 Immunohistology of primary osteoblasts.....	116
4.10 Porous Scaffolds	118
4.10.1 Morphology of porous scaffolds by immersion precipitation.....	118
4.10.2 Morphology of porous structures by freeze drying and particulate leaching .	120
4.10.3 Morphology of porous structures by melt infiltration technique	122
4.11 Nanofibers.....	124
4.11.1 Morphology of nanofibers using conventional electrospinning technique.....	124
4.11.2 Effect of molecular weight on fiber morphology	126
4.11.3 Effect of Solvent on fiber morphology	127
4.11.4 Dispersion of nanoparticles in nanofiber nanocomposites	128
5. Summary.....	129
6. References.....	133

List of Abbreviations

AFM	Atomic force microscopy
HA	Hydroxyapatite
ECM	Extracellular matrix
BTE	Bone tissue engineering
MSC	Mesenchyma stem cells
BMSC	Bone marrow stromal cells
PGA	Poly glycolic acid
BMP	Bone morphogenetic proteins
TGF- β	Transforming growth factors
DBM	Demineralized bone matrix
CDC	Centre for disease control
Y-TZP	Yttria stabilized zirconia
Nano HA	Nano hydroxyapatites
α -TCP	α -Tricalcium phosphate
β -TCP	β -Tricalcium phosphate
BCP	Biphasic calcium phosphate
SBF	Simulated body fluid
ELI	Extra low interstitial
Bcc	Body centered cubic
GPa	Giga pascals
MPa	Mega pascals
FDA	Food and drug administration
UHMWPE	Ultra high molecular weight polyethylene
HDPE	High density polyethylene

PMMA	Polymethyl methacrylate
PLLA	Poly (L-lactic acid)
ALP	Alkaline phosphatase
PHB	Polyhydroxy butyrate
PNC	Polymer nanocomposite
FI	Fluorescence intensity

1. Introduction

Bone is a paradigm for a dynamic tissue because it has a unique capability of regenerating or remodelling throughout its life. However, many circumstances call for bone grafting owing to bone defects arising from either traumatic or nontraumatic damage. Bone grafting is a field of intensive investigation in human health care, as it directly affects the quality and length of human life. Basically, it is a surgical method that repairs or regenerates the defective bone with the help of bone grafting materials.

Of course, the need for such bone grafts truly depends on the complication of bone defects. For example, if a defect is minor, bone has its own capability to self-regenerate its functions within a few weeks time concerning applied stress of cellular and other metabolic components. Therefore, bone grafting is not required in such a situation. But, in case of severe defect, when the loss of volume is too high, bone will not heal by itself. Under these circumstances, bone grafting is actually required to repair or regenerate the defective bone into normal healthy bone without damaging living tissues. There are several methods available for the treatment of bone defects, including customary methods of autografting (bone from the same patient) and allografting (bone from a different patient). Although they are clinically considered as good therapies, they still encounter some practical complications. For example, supply of an autograft is limited and there is a possibility of pathogen transfer from allograft. Accordingly, there is a great need for engineering synthetic bone grafts equivalent to natural bone tissue in all aspects. Currently, numerous synthetic bone grafts are available for clinical use, which are capable of alleviating some of the practical complications associated with autografts or allografts. Although there has been good progress in bone grafting using synthetic bone grafts, the way in which they execute their functions in vivo is quite different from one another. The characteristics of currently available synthetic bone grafts are drastically different from those of natural bone tissue in many aspects, in particular, molecular interaction between minerals and organic components. This is mainly due to the absence of peculiar self-organizing interactions between the apatitic crystals and the proteic components occurring in natural bone tissue. Furthermore, the most synthetic bone grafts available today are considerably different from natural bone either compositionally or structurally or in combination. It is well known that natural bone tissue is a nanocomposite material, constituted of nanosize bladelike crystals of hydroxyapatite (HA) grown in intimate contact with a proteic matrix rich in collagen nanofibers [1, 2], thereby choosing the

HA/collagen as a precursor for making synthetic bone grafts. This will give an additional feasibility in adapting to the body environment.

There are several methods currently employed for the processing of bone grafts. The biomimetic approach is one among them that has recently gained much interest. It is perceived that, this method is more beneficial than conventional methods owing to the possibility of processing synthetic bone grafts by mimicking the biological mechanism of natural bone tissue.

As mentioned before, alternative therapies other than autografts and allografts, have very low success rates in bone grafting procedures. This has resulted in emerging new technologies, utilizing different materials such as metals, ceramics and polymers. Nevertheless, it is known that none of the synthetic materials has been hundred percent successful. Some of the polymers especially biodegradable polymers have gained much attention, because of their very rich functionalities and properties. Microbial polyesters like polyhydroxybutyrate (PHB) and its copolymers have been studied extensively for biomedical applications because of their biodegradability and biocompatibility. However homopolymers of PHB alone are not the preferred choice when targeting for high load bearing applications because of their brittle behaviour caused by high crystallinity, poor thermal stability and low processability [3-5]. On the contrary, copolymers show wide variety of chemical and structural functionalities with different comonomer units as well as comonomer compositions. It is known that increasing hydroxyvalerate content in PHB reduces the brittleness of the matrix. Nevertheless, this trade off is accompanied by decrease in stiffness and biocompatibility. Thus, it is imperative to find an alternative ways to improve stiffness and strength without compromising the toughness, so that the mechanical properties are just suitable for load bearing applications.

One such alternative is by using particulate filled systems in which, hard filler is incorporated in soft polymer matrix with the aim of increasing strength, stiffness as well as toughness. For an application involving cells and tissues, it is often expected that the contributing phases in a composite should be hundred percent biocompatible. It is very critical in selecting fillers which can not only improve mechanical properties, but can also increase cell specific properties like osteoinductivity or osteoconductivity. HA is a well established material for implant coating and also as filler for composite materials used in orthopaedic surgery [6-18]. Often there is a great deal of challenge especially for polymer composites systems like PHB and HA where both the phases have some limiting factors. PHB on the other hand being a semicrystalline polymer is a bacterial product and due to its natural origin it is highly stereospecific. HA on the other hand is also hard filler which is capable of initiating multiple

cavitations, when evenly dispersed. This can eventually increase toughness of the composite. Although, toughening enhancement using rubber toughened polymer matrix is well documented, strength and stiffness is drastically reduced. Approach of adding hard nanofillers in soft polymer matrix have been established in many systems like polymer nanoclay systems with pronounced increase in properties like mechanical, barrier, thermal and electrical properties when dispersed uniformly as said earlier. It has been repeatedly verified that the properties suites comparable to those common for the traditional composites can be achieved using polymer nanocomposites containing substantially less (typically less than 5 vol %) amount of filler. Thus the nanocomposites enable greater retention of the inherent processibility thereby retaining the toughness of the polymer matrix. The nanoscopic dimension and extreme aspect ratio inherent in the polymer nanocomposites (PNC), regardless of the filler type (tubes, platelets, or spheres), endow these composites with some fundamental characteristics such as very low percolation threshold, particle-particle interactions at low volume fraction, extremely large interfacial area per unit volume of fillers, short inter-particle distance etc [19-21].

Also it is established that morphology governs mechanical properties. So, in order to get preferred set of property profile, it is important to get favourable morphology. Semicrystalline polymers like that of PHB have great influence on processing conditions. Also morphology of the polymers is governed by contributing phases such as fillers which may affect either in crystallization process by acting as nucleating agents or will influence mechanical properties by contributing to micromechanical processes. Hence, this work is mainly focussed on the morphology, mechanical properties and micromechanical processes of nanocomposites varying in different filler size, shape and loading. Also considerable amount of work is addressed in applying the fabricated nanocomposites to bone tissue engineering applications by evaluating different invitro properties.

2. Basics

2.1 Materials for bone replacement and bone tissue engineering

The ultimate goal of bone tissue engineering is to manufacture synthetic biomaterials that are capable of replacing natural bone tissues with respect to all functional aspects *in vivo*. As, only living bone cells can ultimately generate new bone tissue, a unique approach is to develop bone grafts that are cell-responsive upon implantation. A new wave of advances in nanotechnology and cell biology enables the production of novel cell/tissue-engineered bone grafts, quite resembling autogenic or living bone. Bone tissue engineering is a nascent multidisciplinary field that applies the principles of bioengineering and biosciences towards the development of novel biological substitutes which are capable of restoring, maintaining, or improving a tissue function that fails to regenerate or heal spontaneously.

This method offers a new kind of therapy that differs from conventional implants in that the engineered bone tissue becomes integrated within the patient, affording a potentially permanent and specific cure of the disease state. The prime objective of tissue engineering is; (1) to isolate a small biopsy of specific cells from a patient, (2) to allow them to culture on a perfect scaffold, (3) to transplant the cell-engineered scaffold into the defective site of the patient's body that needs bone regeneration and (4) to guide or direct new tissue formation into the scaffold that can be biodegradable over time. In this respect, three key factors have to be considered for the success of bone tissue engineering. They are cells, scaffold, and cell-matrix (scaffold) interactions (Figure 1). This section briefly summarises the role of these three factors pertaining to the bone tissue engineering.

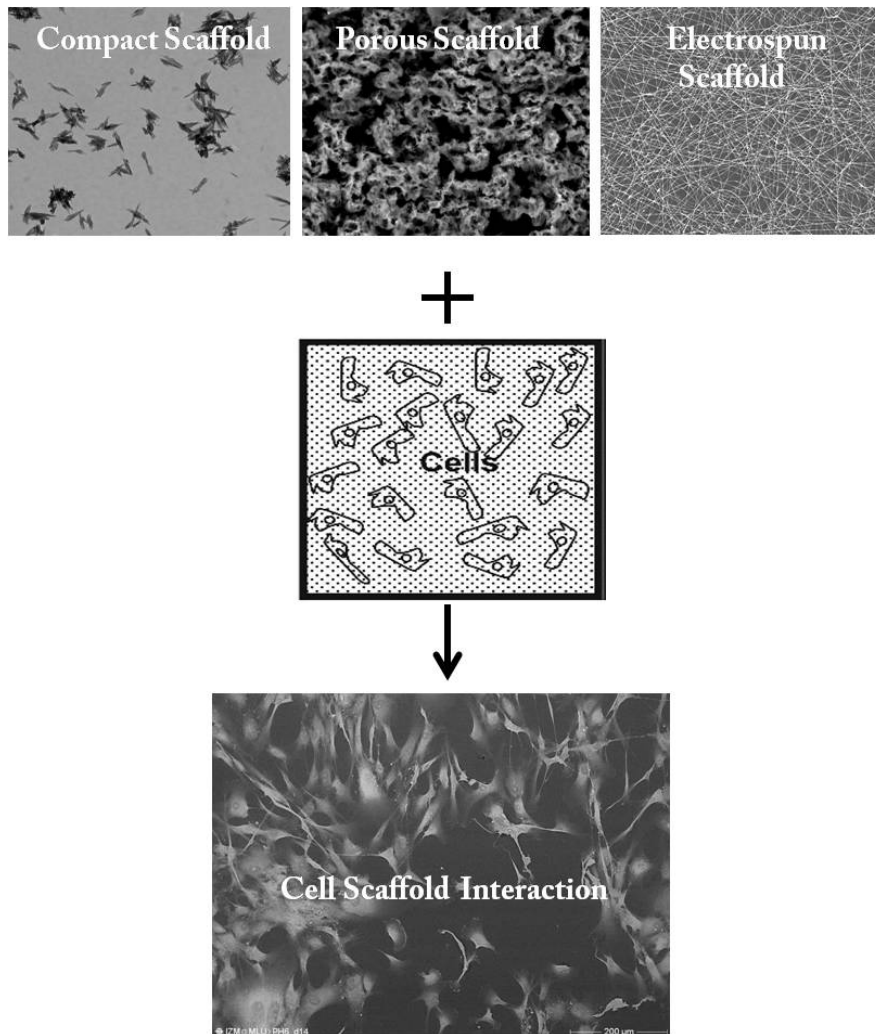


Figure 1: Factors contributing to the success of tissue engineering

2.1.1 Requirements and strategies for bone tissue engineering

Different strategies are adopted for tissue engineering applications. Currently, these strategies are classified as; a) cell based strategies, b) growth factor based strategies and c) matrix based strategies [22, 23]. In reality, sometimes these strategies may work alone or in combination, as they are interdependent on one another. An example of such a system is, a biodegradable scaffold with appropriate mechanical properties, capable of carrying cells and growth factors, leading to osteogenesis (bone growth).

Cell based strategies for bone tissue engineering involves in transplanting osteogenic cells in the defect site, capable of matrix formation and mineral deposition. This could be realized by using suitable cell source like differentiated osteoblasts [24] and osteogenic cell lines [25]. Primary osteoblasts from donor site are difficult to isolate in sufficient quantities resulting in

limited proliferation. Immortalized osteogenic cell lines are clonally derived and well characterized, but exhibit abnormal regulatory mechanisms that may lead to tumorigenic growth. Limitations of the above have focused attention towards other cell sources such as embryonic stem cells (ESC) and bone marrow stromal cells (BMSC). These contain haemeopoitic stem cells and mesenchyma stem cells (MSC) capable of differentiating to osteoblastic lineages. Nevertheless ethical issues concerning ESC have made BMSC the only potential source for MSC. Studies on BMSC injected *invivo* revealed significant reunion and mineralization of femoral defects in comparison to that of autografts [26]. Richards et al. demonstrated the osteogenic capabilities of cultured MSC in a collagen gel carrier injected into distraction gaps of rats femora [27]. Yoshikawa et al. observed rapid bone formation by rat marrow stromal cells cultured on porous HA scaffolds with osteogenic supplements [28]. Breitbart et al. demonstrated that progenitor cells from the periosteum cultured with dexamethasone could be delivered to a rabbit cranial defect via a degradable poly(glycolic acid) (PGA) scaffold generating significant quantity of bone compared to cell free implants [29]. Yet, clinical relevance of these precursors has not been realized because of the nonavailability of large population of fresh cells which can induce bone formation *invivo*.

Therefore, to enhance the rapid production of cellular extra cellular matrix (ECM), a variety of novel *ex vivo* strategies have been investigated. Among them, the most promising strategies are growth factors delivery, bioreactor system and gene therapy.

Growth factors are signalling polypeptide molecules that can activate specific developmental processes in controlling cell migration, differentiation and proliferation. They induce specific response by binding to receptors on the cell surface. Osteoinductive growth factors are a preferable choice for bone tissue engineering applications. Among them, bone morphogenetic proteins (BMP-2 & BMP-7) and transforming growth factors (TGF) from TGF- β family have been considered for clinical applications. Growth factors responses are recognised to be dependent on concentration and time. In order to induce desired osteoinductive effect, higher dosages have to be applied. Nevertheless, development of this strategy for clinical relevance is in preliminary stage due to associated factors such as high costs coupled with complicated mechanisms and related side effects.

The success of matrix based strategies relies on the fabrication of suitable scaffolds that can serve as a substrate, having inductive/conductive microenvironment for cells as well as delivery vehicle for relevant proteins. According to Hutmacher et al., strategies for polymer matrix is further systematically divided into two strategies [30]. In the first strategy, a scaffold should support the cell/tissue from the time of cell harvesting upto to the time of

transplant remodelling in the host tissue. In the second strategy, the mechanical properties of the scaffolds used in exvivo cultures should be able to support the seeded cells to proliferate and differentiate. The degradation and resorption kinetics of the scaffold are designed to allow the seeded cells to proliferate and secrete their own extracellular matrix in the static and dynamic cell seeding phase (weeks 1-12), whereas, the polymer scaffold gradually vanishes leaving sufficient space for new cell and tissue growth. The physical support by the 3-D scaffold is maintained until the engineered tissue has sufficient mechanical integrity to support itself.

2.1.2 Selection criteria for materials in bone tissue engineering

Although most of the synthetic grafts available today possess favourable characteristics for bone regeneration, none of them now resembles autogenic bone, which further stimulates research in bone grafting.

Selection of bone grafts also contribute in achieving clinical success. It depends in part on the characteristics of these grafts. Essentially they must satisfy a few characteristics, particularly osteoconductive, osteoinductive and osteogenic, which are summarised in Table-1.

Any material that holds all these key factors can probably be considered as an ideal bone graft. Although several synthetic grafts satisfy some of these factors, none has the ability to satisfy all these factors together, except for autogenic bone. Therefore, investigations are still in action to recognize an ideal synthetic bone graft

Table 1: Basic characteristics of ideal bone graft (Reproduced from[31])

Characteristics	Comments
Biocompatible	Biologically compatible to host tissue (i.e., should not provoke any rejection, inflammation, and immune responses).
Bioactive	To facilitate a direct biochemical bonding to host tissue
Biodegradable in a controlled fashion	The rate of biodegradation has to be adjusted to match the rate of bone tissue formation
Degradation time	Preferably less than six months, but depends on case by case.
Mode of degradation	Bulk or surface erosion.
Osteoconductive	Capable of supporting in-growth of sprouting capillaries, perivascular mesenchymal tissues, and osteoprogenitor cells from the recipient host into the 3-D structure of a graft that acts as a scaffold.
Osteoinductive	A process in which biomolecules enriched within the graft convert the patient's cells into cells capable of forming a new bone
Vascular supportive	Should provide channels for blood supply for fast and healthy bone regeneration
Nontoxic	Should not evoke toxicity to host tissue.
Nonimmunogenic	Should not evoke immunogenic response to host tissue
High porosity with interconnected pores	To maximize the space for cellular adhesion, growth, ECM secretion, revascularization, adequate nutrition, and oxygen supply. However, it should not compromise mechanical strength of the graft
Pore size	To allow cell penetration.
<50 μm	Sufficient to in-growth of fibrous tissue
>100 μm	Needed for new bone generation
>200 μm	Required for mature osteons to form
3-D structure	For the assistance of cellular in-growth and transport of nutrition and oxygen
High surface area-to-volume ratio	Needed for high density of cellular attachment.
Surface modifiable	To functionalize additional chemical or biomolecular groups in order to enhance cellular adhesion and bone tissue growth
Adequate mechanical strength	To withstand in vivo stimuli
Ultrapure	Needed for better performance of graft
Sterilizable	To avoid toxic contamination
Cost-effective	Affordable to all

There are a variety of bone grafting methodologies available, including autografting, allografting, xenografting, and alloplastic or synthetic bone grafting, each varying in their advantages and disadvantages. A diagrammatic representation of typical bone grafting in humans, evolved chronologically is shown in below (Figure 2). The selection of the grafting method is purely dependent on the nature and complication of the bone defects as well as the choice of available bone grafts. And, of course, the key decision depends on the surgeon's own experience and wisdom.

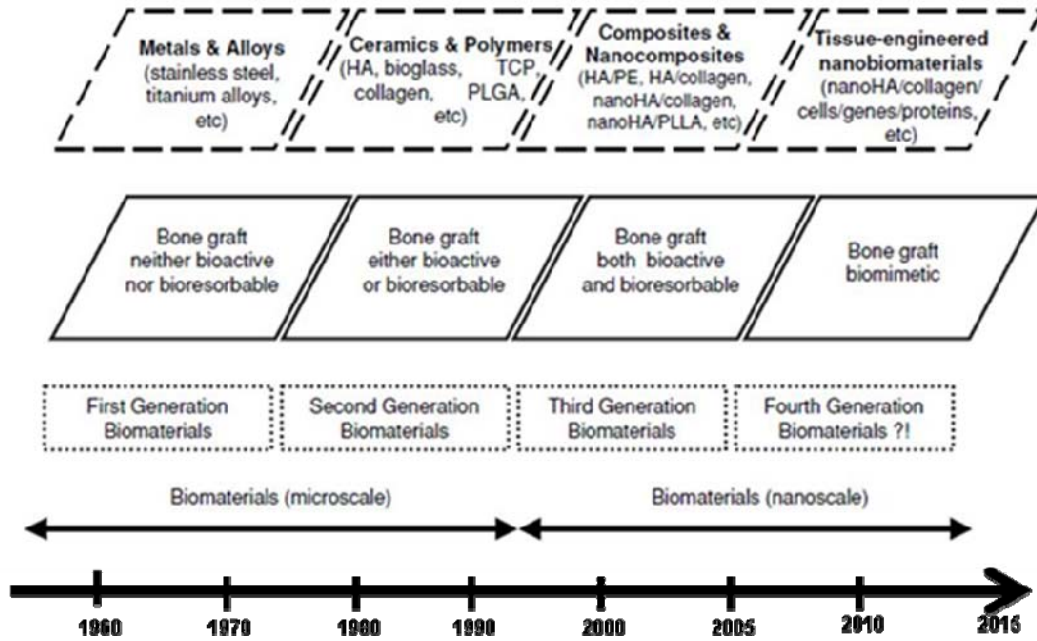


Figure 2: Evolution of bone grafts in chronological order (Reproduced from[31])

2.1.3 Bone replacement materials: State of art

Bone derived materials

Bone derived materials are gifted with osteoinductive capacity that can convert patient's cell into cells that are capable of forming new bone tissue. They include autografts, allografts and demineralised bone matrix (DBM). Successful grafting of autograft from cancellous bone on iliac crest was first reported by Mowlem. Since then autogenous grafts have become the gold standards for skeletal reconstruction [32]. They are the most widely used materials for orthopaedic surgeries and have gained high clinical relevance because of osteoconductive, osteogenic and osteoinductive properties. Also there is an absence of immunological rejection in autografts. Autogenous grafts have pre-existing viable osteogenic cells for immediate osteogenesis (Figure 3).

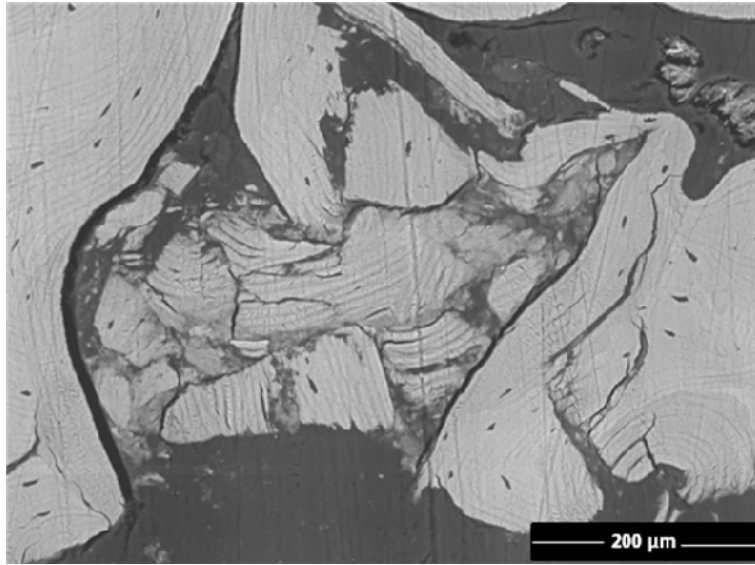


Figure 3: Bone chips filled in a cavity of compact bone; ESEM image, BSE material contrast

However autogenous grafts have several disadvantages. First and the foremost is their limited availability which restricts the repair of large sized defects. Second, a separate operation is required to harvest the bone from iliac crest or ribs that may result in complications like donor site morbidity.

Allografts are the second choice of materials preferred by orthopaedic surgeons. The first usage of allograft bone was documented by Sir William MacEwen in the year 1879 [33]. These transplants are mainly obtained from donors. Donated bones are usually preserved by bone banks. These banked bones are available in different forms. They are then processed, which lowers the risk of virus (transferring from the donors) at the cost of weakened mechanical and biological properties. It is, however, also possible to harvest femoral heads of patients who have been implanted with artificial metallic hip replacement. Allografts have osteoinductive and osteoconductive properties. But they lack osteogenic properties because of the absence of viable cells [34]. Allografts are prepared in fresh, frozen and freeze dried forms. Frozen and freeze dried allografts are osteoconductive, but are considered to have weak osteoinductive properties compared to the fresh ones. The Center for Disease Control (CDC) which published in the year 1988, the first case of an infection with the HI-Virus (Human Immunodeficiency Virus) by cryoconserved allogeneous bone fabric [35]. There after many reports have been published concerning the disease transmission.

Xenografting is a method of transplanting tissues from one species to another. This type of bone transplant was first documented by Job van Meekren who tried to fill a defect site in human skull using dog's skull [36]. The feasibility of using xenograft bone transplants is still

under trial, because of very high mortality rates associated with this type of transplantation. Most profound barrier in xenograft transplantation is associated with immunological rejection either by antibody mediated rejection or by innate or immune cell mediated rejection. However, the shortage of tissues from autogenous transplants has prompted to continue research in this field.

Other than autografts, allografts and xenografts, DBM is also considered as a potential candidate for skeletal tissue repair. DBM is allograft bone that has been demineralized and processed to denatured form of protein matrix. Urist et al. observed the potential of DBM, which induced bone formation in animals [37]. Since then many studies have shown that these materials can induce bone formation, when properly processed. DBM can be extracted both by cancellous as well as cortical fractions of bone. But recent research as shown cortical bone as preferred choice for DBM synthesis because of its higher osteoinductivity and lower antigenic potential than cancellous bone [38].

Table 2- FDA approved materials currently on the market

Product	company	Material	Application
Accell	Integra Life Science (Iso Tis)	DMB	Bone graft substitute
Bone Graft	Medtronic	Collagen and rhBMP-2	Lumbar spinal fusion/tibial fracture/oral maxillofacial
Collagen Bone Graft	Zimmer/Collagen Corp	HA/calcium phosphate	Long Bone fracture osseous defect
Grafton DMB (Gel, Putty, Flex)	Osteotech	DMB in glycerol	Bone void filler
OSTEOSET® Bone graft substitute	Wright Medical Technology	Calcium sulfate	Bone graft substitute
Polygraft TM TCP Bone graft Substitute	Osteobiologics, Inc	PLGA, β -TCP and PGL fibers	Bone void filler
Pro Osteon® 200R	Biomet Osteobiologics	HA and calcium carbonate	Bone graft substitute
Plexur™ P	Osteotech	Cortical fibers suspended in PLGA	Bone void filler
VITOSS	Orthovita	β -TCP	Cancellous bone void filler
DUOWEDGE	Kasios	HA 60% and TCP 40%	Wedge for high tibial Osteotomy
Polygraft BGS	SMITH and NEPHEW Inc		Bone void filler
Cortoss™	Orthovita®	non resorbable composite resin	Bone augmentation material
Healos	DePuy Orthopaedics Inc	composite of collagen and hydroxyapatite	Spinal Fusions

DBMs are commercially available with the trade name (Table-2) *Grafton* DBM (Osteotech, Inc, Eatontown, NJ) which has several formulations in glycerol carrier. Though manufacturers report that there were no disease transmission reported in 1.5 million surgical procedures, however some reports evidenced a mild carrier toxicity in animal models [39]. *Osteofil* (Regeneration Technologies Inc, RTI) is DBM in a gelatin and water medium. *Dynagraft* (GenSci Regeneration Sciences Inc., Toronto, Canada) is another form of DBM, with its carrier, a combination of a polymer (ethylene oxide and propylene oxide).

Metallic biomaterials

Metallic materials continue to play an essential role as biomaterials to assist in the repair or replacement of bone tissue that has become diseased or damaged [40]. Metals are more suitable for load-bearing applications compared to ceramics or polymeric materials due to their combination of high mechanical strength and fracture toughness. Other than their mechanical performance, these materials can be fabricated to high precision end products. There are certain requirements for metallic biomaterials to perform inside the body. They should possess excellent mechanical and biological biocompatibility, resistance to corrosion, mechanical properties like fatigue and tensile strength. Currently approved and commonly used metallic biomaterials include stainless steels, cobalt alloys and titanium. With the ever increasing ageing population and limited number of alternative substitutes, there is demand for properties and functionalities like low modulus, shape memory and super elasticity in metallic materials. This has led to design and fabrication of a wide variety of materials including magnesium and their alloys, nickel-titanium alloys etc.

Among the metallic materials, stainless steel is resistant to a wide range of corrosive agents due to its high Cr content (more than 12 wt %), which allows the formation of a strongly adherent, self-healing and corrosion resistant coating oxide of Cr_2O_3 . Several types of stainless steel are available and the most widely used for implant manufacturing is austenitic stainless steel. In order to be austenitic at room temperature, stainless steel should contain certain amount of austenite stabilizing elements such as Ni or Mn. AISI 316 L is the only stainless steel that has been used in clinical practice. Its chemical composition is 0.03 wt% C, 17–20 wt% Cr, 12–14 wt% Ni, 2–3 wt% Mo and minor amounts of nitrogen, manganese, phosphorus, silicon and sulphur. Since, there is considerable amount of nickel in this grade; there are possibilities of steel causing nickel allergy [41-44]. This had led to the development of nickel free stainless steel [45]. Earlier developments of nickel free stainless steel have

resulted in partial substitution of nickel by N and Mn. N stabilizes the austenitic phase and induces an increase in both corrosion resistance and the mechanical properties (yield stress). However, cytocompatibility of Mn is not yet clear. Kuroda et al. have developed austenitic stainless steel free of Ni and Mn. Yet, the use of stainless steel as an implant materials have certain limitations because of its poor wear resistance. This can result in the release of wear debris particles causing detrimental effect on implant failure due to aseptic loosening and also leads to infections [46].

Co-Cr alloys are considered to be superior compared to stainless steel because of their properties like excellent corrosion resistance, good wear resistance and significant fatigue strength. Basically two types of Co-Cr alloys are used for fabricating implants a) cast CoCrMo alloy (cast alloy) and 2) wrought CoNiCrMo alloy.

Ever since the introduction of bone plates and screws in 1965, cp titanium has found various applications as an implant material in the field of medicine. Commercially pure (cp) titanium and extra low interstitial (ELI) Ti-6Al-4V alloy are the two most common titanium based implant biomaterials. Cp titanium has high corrosion resistance and outstanding biocompatibility compared to stainless steel and cobalt based alloys. Moreover it doesn't cause allergic reactions *invivo* [47]. These properties are in some sense attributed to the formation of protective passive layer on the surface, in the presence of oxygen. Mechanical properties of cp titanium depend on the amount of trace elements present. Nevertheless the presence of vanadium in the existing grade has proved to be toxic [40]. To address the potential concern over vanadium toxicity, two $\alpha+\beta$ Ti-6Al-7Nb, Ti-5Al 2.5Fe alloys were introduced. Elastic modulus of these vanadium free Ti alloys was reported to be around 110 GPa. This large mismatch in modulus will cause insufficient loading of the bone adjacent to the implant, which results in stress shielding. Hence, research effort in developing low modulus Ti alloys are been extensively carried out.

All the existing metallic materials approved by FDA has some limitations, which include a) release of toxic metallic ions and/or particles through corrosion and wear b) mechanical mismatch of elastic modulus compared to that of bone (Table 3), leading to stress shielding and c) inertness in *invivo* in long term application leads to inflammation and cost of second surgery for implant removal. With the aim of overcoming these limitations, efforts have been made to apply new materials and new fabrication methods. Among them the most interesting metallic material is magnesium.

Magnesium is an exceptionally lightweight metal. With a density of 1.74 g/cm³, magnesium is 1.6 and 4.5 times less dense than aluminium and steel respectively. The fracture toughness

of magnesium is greater than ceramic biomaterials such as hydroxyapatite, while the elastic modulus and compressive yield strength of magnesium are closer to those of natural bone. Moreover, magnesium is essential to human metabolism and is naturally found in bone tissue [48-50]. The level of magnesium in the extracellular fluid ranges between 0.7 and 1.05 mmol/L, where homeostasis is maintained by the kidneys and intestine [51]. The major drawback of magnesium in many engineering applications is its low corrosion resistance, especially in electrolytic, aqueous environments, which becomes an intriguing property for biomaterial applications, where the *in vivo* corrosion of the magnesium-based implant involves the formation of a soluble, non-toxic oxide that is harmlessly excreted in the urine. Nevertheless efforts have been made to coat magnesium surface with nontoxic metals like silver, tantalum, titanium etc.

Table 3-Summary of physical and mechanical properties of various implant materials in comparison to bone (reproduced from [52])

Properties	Natural bone	stainless steel	Co-Cr alloy	Ti alloy	Magnesium
Density (g/cm ³)	1.8-2.1	7.9-8.1	8.3-9.2	4.4-4.5	1.74-2.0
Elastic modulus (Gpa)	3-20	189-205	230	110-117	41-45
Compressive yield strength (Mpa)	130 -180	170-310	450-1000	758-1117	65-100
Fracture toughness (MPam ^{1/2})	3-6	50-200	N/A	55-115	15-40

Ceramic Biomaterials

Ceramics are the class of inorganic, non-metallic biomaterials intended to be used for medical applications, especially orthopaedic and dentistry. Preliminary application of these materials was thought to be an alternative to metallic material because of their bone bonding capability. With the ever increase in knowledge about these materials, it is now thought that these materials are also osteoinductive as well. These findings have made possible the development of various kinds of ceramics for tissue engineering applications. Based on the chronological development and their properties, ceramics can be broadly classified as a) nonresorbable (relatively inert) which includes alumina, zirconia, silicone nitrides, and carbons, b) biodegradable or resorbable ceramics, which includes calcium phosphates and calcium aluminates [53, 54] and c) bioactive or surface reactive (semi inert), which include glass ceramics and certain dense hydroxyapatites [12, 55]; these are summarized in Table 4.

Alumina and Zirconia are considered as inert bioceramics because of stability in their mechanical and physical properties. Their major use in orthopaedics is in total hip and knee replacement as femoral heads and acetabular cups. These bioceramics are relatively very hard

accompanied by low friction and wear resistance, which make them suitable materials as bearing components. The clinical success associated to the use of ceramics led to the implantation of more than 3.5 millions alumina components and more than 600,000 zirconia femoral heads worldwide since 1990 [18].

Pure zirconia has properties which are inferior to those of alumina. This led to development of new generation ceramics known as Yttria stabilized zirconia (Y-TZP). Y-TZP are popular alternative for alumina because of their high strength and fracture toughness accompanied by extremely low friction wear (less than 0.1 mm^3 per million cycles) as measured under normal hip simulation conditions [56]. Implants from these ceramics were introduced for clinical use because of their good mechanical properties and high crack resistance [57]. The second generation ceramics includes bioresorbable ceramics. These ceramics when applied to *in vivo* can degrade without causing inflammatory response. Most important bioresorbable ceramics are calcium phosphates (Table 4). They are salts of orthophosphoric acid. Their physical properties are dependent on the composition and crystal structure. The application of this material started around 1970s and has mainly been used as bone void fillers.

Hydroxyapatites, especially bioactive hydroxyapatite (HAp, $\text{Ca}_{10}(\text{PO}_4)_6(\text{OH})_2$) are the most widely used bone substitute material [58] due to their similarity in chemical composition to the mineral portion of the bone. Polycrystalline hydroxyapatite has a high elastic modulus (40-110 GPa) and a Poisson's ratio of about 0.27, which is very close to that of bone (≈ 0.3). Due to their brittleness, they are often targeted to non load bearing applications such as bone void filler or a coating material for metallic implants. Recent advancement in nanotechnology has made possible the use of nanohydroxyapatites as filler in polymer matrix.

Tricalcium phosphate is a non stoichiometric ceramic compound, which exists in two distinct crystal phases (α -TCP & β -TCP) and has Ca to P ratio 1.5:1. The α -TCP crystallizes in the monoclinic space group, and β -TCP crystallizes in the rhombohedral space group. Despite their similar chemical composition, their different crystallographic features confer different resorption features: α -TCP is more soluble than β -TCP, and it is obtained after heating the β -TCP to more than 1170°C . Variation in atomic ratios and crystal structure has pronounced effect on biodegradability. It is probably because of this biodegradation behaviour that biodegradable TCP ceramics gives rise to extensive bone remodelling around the implant [59]. *In vivo* studies on ceramic (TCP) implants carried out in our group showed a positive influence on new bone formation. It was observed that, with the resorption of TCP, a new bone was formed at that site (Figure 4).

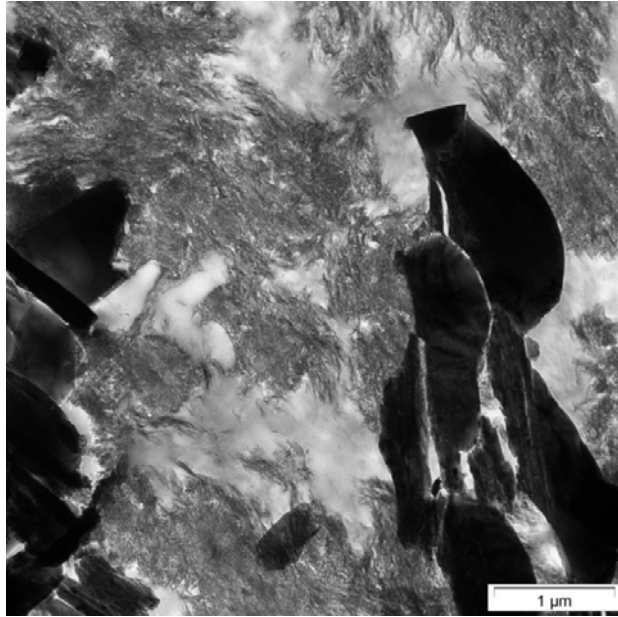


Figure 4: EFTEM image showing new bone formation close to TCP ceramic implant (ultrathin sections)

Biphasic calcium phosphates are the mixture of hydroxyapatite and tricalcium phosphates. Compared to α -TCP & β -TCP, the stability of HA is more under physiological conditions, as it has lower solubility and slow resorption kinetics. BCP was thought of as an optimum balance between more stable HA and more soluble TCP. Thus the kinetics and bioresorbability of BCP can be tuned to required degree by changing the composition of TCP/HA [6].

Corals are among another interesting class of ceramic materials that have been widely experimented in the current biomaterial research. Coral mineral, either in its natural form or converted to hydroxyapatite, has gained considerable success in bone graft applications due to its porosity (which ranges from 100–500 μm). It is similar to cancellous bone in morphology and is one among the limited number of materials that will form a chemical bond with bone and soft tissues in vivo [60]. Corals are preferred as bone substitution materials because of their structural similarity to that of bone [61]. The main component of corals is calcium carbonate, which is gradually resorbed by the body [62]. Natural corals from genus *Porites sp.* consist principally of calcium carbonate in the structural form of aragonite, mixed with impurities such as Sr, Mg and F ions and an organic matrix. Guillemin et al reported the biodegradability and biocompatibility of commercially available BiocoralTM which is used as bone grafts material [63]. One of the major disadvantages of natural corals lies in their fast resorption rate. Stability of corals is presently achieved by commercially manipulating the corals, which are known as Coralline HA. Pro Osteon[®] is a commercially

available coral-derived material. Until now efforts have not been successful to achieve its stability.

Table 4: Biological relevant calcium phosphates

Name	Formula	Abbreviation	Ca/P
Monocalcium phosphate anhydrate	$\text{Ca}(\text{H}_2\text{PO}_4)\cdot\text{H}_2\text{O}$	MCPA	0.5
Dicalcium phosphate anhydrate	$\text{CaHPO}_4\cdot 2\text{H}_2\text{O}$	DCPA	1.0
Octacalcium phosphate	OCP	C	1.33
α -Tricalcium phosphate	$\alpha\text{-Ca}_3(\text{PO}_4)_2$	α -TCP	1.5
β -Tricalcium phosphate	$\beta\text{-Ca}_3(\text{PO}_4)_2$	β -TCP	1.5
Amorphous calcium phosphate	$\text{Ca}_x\text{H}_y(\text{PO}_4)_z\cdot\text{H}_2\text{O}$, n=3-4.5	ACP	1.2-2.2
Hydroxyapatite	$\text{Ca}_{10}(\text{PO}_4)_6(\text{OH})_2$	HA	1.67
Tetracalcium phosphate	$\text{Ca}_4(\text{PO}_4)_2\text{O}$	TTCP	2.0

The third generation ceramics are the bioactive or surface reactive ceramics. They include bioglass and dense hydroxyl apatites. Due to their surface reactivity, they contribute in bone bonding and enhance the effect on bone tissue formation. Bioceramics in this regard have gained much attention because of its capability to make direct contact with living bone after it has been implanted. The first bioactive ceramic developed after Hench et al. was bioglass (Bioglass[®]) with the composition $\text{Na}_2\text{O}-\text{CaO}-\text{SiO}_2-\text{P}_2\text{O}_5$. In vivo studies revealed that bioglass forms a layer of biologically active bone like apatite on their surfaces [12]. A similar bone like apatite layer was found to be formed on the surface when immersed in simulated body fluids (SBF) [64].

Polymers

Although polymers are widely used as implants in various applications in medicine such as vascular prostheses, drug delivery, nerve regeneration etc, only a limited number of polymers have been used for bone replacement purposes due to the limitations in their mechanical properties and biodegradability. The choice of polymer as bone replacement material largely depends on the following factors (besides the general requirement of biocompatibility): (a) mechanical properties of the polymer if the polymer is going to be used as load bearing material; (b) biodegradation behaviour of the polymer if the implant has to be eliminated after certain period. (c). ability to bond with bone or to induce bone ingrowth.

Based on these criteria, polymers for bone regeneration are classified into a) synthetic non resorbable polymers, b) synthetic resorbable (biodegradable) polymers and c) resorbable natural origin polymers.

However, all polymers which have been tested for their biocompatibility are not accredited by FDA as implantable materials due to some limitations. Hence, only polymers with clinical relevance will be discussed.

a) Synthetic nondegradable polymers

Polyethylene is the most widely used synthetic polymer for bone tissue engineering. Especially ultra high molecular weight polyethylene (UHMWPE) has potential applications in joint endoprostheses because of its advantages such as good sliding properties [65], good impact strength, good fatigue resistance and good biocompatibility [66]. However, particle migration due to friction and wear and high creep compliance has made this polymer inefficient for applications requiring high load transfer. Attempts to enhance mechanical performance of UHMWPE, either by crosslinking [67] or by reinforcing with carbon fibers has been reported [68]. In another report self reinforced fibers of UHMWPE has also been reported. HDPE is another interesting polymer used as implantable material for bone substitutes and was mainly established by Bonfield et al. There are very few reports on HDPE alone as a bone substitute material because of its low strength and toughness compared to bone. Nevertheless HDPE/HA implants developed by him was accepted because of its promising cytocompatibility and mechanical performance.

Another synthetic polymer widely used in orthopaedic application is PMMA. This acrylic have played great role in anchorage of prostheses to the surrounding bone in cemented arthroplasties. Several different methods are adopted to fit artificial joints to bone. The conventional method is to press-fit joint prostheses using grouting material called acrylic cements [69]. They are two component self polymerizing systems containing PMMA as solid powder and MMA as liquid monomer. The mechanism of cement interface with bone is not chemical. Adhesion between cement and bone in reality is established by a rough surface on either of the surfaces, which upon setting will mechanically interlocks. Release of unreacted monomers during cross linking has been debated regarding its applications. It was also reported that exothermic reaction associated with polymerization will produce elevated temperatures in tissues that may lead to bone necrosis [70].

A study initiated in our group on PMMA bone cements showed promising results. The results of the animal study proved excellent biocompatibility, osteocompatibility and bioactivity of

the PMMA bone cements with surrounding tissues, which stimulated the formation of new bone growth with an Haversian system (Figure 5). Furthermore, it enhanced the rate of bone-healing within a short period. Also, it was found that PMMA cement pierced the trabecular structure of bone and thereby established a good mechanical interlocking between bone and cement surface. Also there was absence of immune response in those cements.

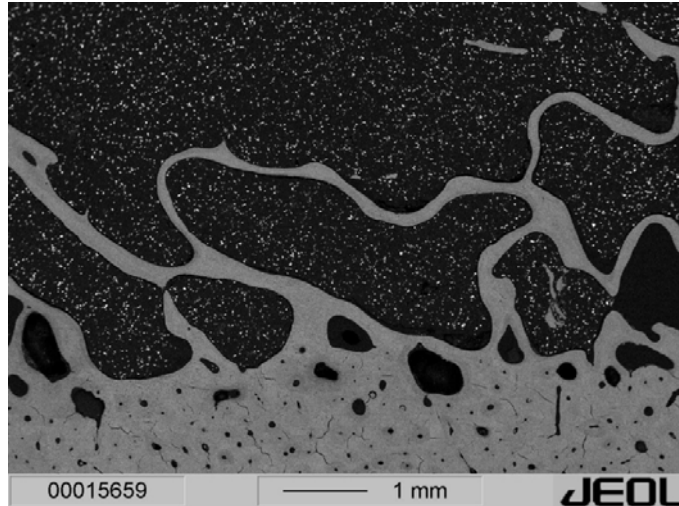


Figure 5: PMMA bone cement is intruding trabecular structures of bone ensuring mechanical interlocking. The cement contains X-ray opacifier particles that appear as white dots; SEM image, BSE material contrast

Nevertheless, applications involving long term implantation using cements have not been satisfactory because of mechanical failure caused by fatigue failure. This is assumed to be a predominant *in vivo* failure. In order to enhance the bonding efficiency of cements, bioactive bone cements along with PMMA are also been experimented.

b) Synthetic biodegradable polymers

Synthetic biodegradable polymer gained significant importance in the scientific community because of its associated properties. Primary and the most important property is the biodegradation. This property has revolutionized the way of thinking, especially for surgeons. Conventional metallic implant and nonbiodegradable systems when implanted should be removed from the body after complete healing of the defect site. This necessitates a second surgical event for implant removal. Moreover bone does not carry sufficient load during the healing process, because the load is carried by the rigid stainless steel which may result in refracture during implant removal. However an implant prepared from biodegradable polymer can be engineered to degrade at a rate that will slowly transfer load to the healing bone [71]. Another possible application concerning biodegradability is in controlled drug

delivery systems. BMPs are established bioactive substance, which improves bone growth and these biodegradable systems can be used as suitable carriers thereby releasing them at the rate of degradation. Nevertheless many of biodegradable polymers with good cytocompatibility and biodegradability are still not been approved by FDA, due to their poor mechanical properties. Poly (α -hydroxy esters), such as poly (L-lactic acid) (PLLA), poly(glycolic acid) (PGA) or their copolymers, poly(DL-lactic-co-glycolic acid) (PLGA) are among the few synthetic polymers approved for human clinical uses, including those for small load-bearing applications [71-73].

Porous PLGA scaffolds with average pore size of 150-300 or 500-710 μm were seeded with rat calvarial osteoblasts. There was very good proliferation and there was increased ALP activity which is a marker for osteogenesis. Also cell penetration inside the pores were upto 200 μm . Similar results were also found with rat bone marrow stromal cells [74].

In another study Böstman and Päivärinta observed new bone formation in polyglycolide screws implanted into femora and tibiae of rabbits. They concluded that no specific osteogenic capacity of PGA could be found. [75]. A later study on self reinforced PGA membranes, which was fabricated by rapid hot pressure compression was implanted in femoral of Wistar rats. Periosteal new bone formation was detected in the samples [76].

Like PGA, PLLA is also widely used material for bone tissue engineering. Gogolewski's et al. used a poly-L-lactide (PLLA) membrane to cover 1-cm defects that they created in the radii of skeletally mature rabbits [77]. They chose a polymer with pore sizes of 5-15 μm diameter, a thickness of 250 μm , and an in vivo life span of 18-24 months. At the conclusion of the study, they had grossly and histologically demonstrated that cortical bone had regenerated to span the defect [77].

Another possible material is poly- ϵ -caprolactone- *co*-lactide. This material has been applied in nonosseous applications [78, 79] but is newly applied to bone tissue engineering as a paste or wax. Ekholm and coworkers evaluated the absorption and biocompatibility of this copolymer using a rat femoral defect model [80]. The copolymer was specifically a paste of 40:60 poly- ϵ -caprolactone- *co*-D,L-*co*-L-lactide with a 50:50 D-lactide to L-lactide ratio. The material elicited a moderate inflammatory response in bone and was still present after 1 yr in this preliminary study.

Rabbit bone marrow cells were inoculated on PLA, PHB, or PHBHHx 3D scaffolds to evaluate their in vitro biocompatibilities. It was found that PHBHHx had the best performance on attachment, proliferation of bone marrow cells. The cells on PHBHHx scaffolds presented typical osteoblast phenotypes: round cell shape, high alkaline

phosphatase (ALP) activity, strong calcium deposition, and fibrillar collagen synthesis. After incubation for 10 days, cells grown on PHBHHx scaffolds were approximately 40% more than that on PHB scaffolds and 60% more than that on PLA scaffolds. ALP activity of the cells grown on PHBHHx scaffolds was up to about 65 U/g scaffolds, 50% higher than that of PHB and PLA, respectively. SEM results showed that PHBHHx scaffolds had the appropriate roughness for osteoblast attachment and proliferation comparing with PHB and PLA, indicating that PHBHHx was a suitable biomaterial for osteoblast attachment, proliferation and differentiation from bone marrow cells [81].

Natural polymers have also been studied and suggested for orthopaedic applications. These include polysaccharides (starch, alginate, chitin/chitosan) or proteins (soy, collagen, fibrin gels). But none of them can be used for load bearing applications because of their poor mechanical properties. Infact some of the proteins like collagen has been extensively for orthopaedic repair. Explanation of these materials is beyond the scope of this review.

Composites Materials

Composite materials may be defined as those materials that consist of two or more fundamentally different components that are able to act synergistically to give properties superior to those provided by either component (D.F.Williams). By varying the type and distribution of reinforcing phase in composites, it is possible to obtain wide range of mechanical properties as well as to optimize the structure of implant and its interactions with the surrounding tissues. In other words it is possible to avail both the properties of interacting systems. This has led to increased interest in using composite materials for orthopaedic applications [82-84]. Accordingly there are myriad of matrix and reinforcing phases used for orthopaedic applications. Based on type of reinforcing component used, composites may be broadly classified into a) fiber reinforced composites and b) particulate reinforced composites Carbon fibers have been used in orthopaedic applications to successfully reinforce thermoplastic polymer matrix like polyethyletherketone (PEEK) [85, 86], polyaryletherketone (PAEK) polysulphone[87], polybutyleneterephthalate (PBT) [88] etc. Successful application of these fibers lies in the mechanical properties it delivers to respective matrix. Orthodesign, a commercially available carbonfiber thermoplastic hip prosthesis has flexural stiffness about one-fifth of conventional stainless steel implants (Figure 6). Nevertheless, the main problem associated with these fibers is the release of carbon debris into the surrounding tissues. It has been shown that they elicit adverse cell

response in some cases, such as collagenase synthesis, cell detachment and lysis [89] and the release of cell activating factors, which then activate other cells in the culture. Another issue concerning the nonresorbable polymer matrix is their physical stability in invivo environment. Mckenna et al investigated the stability of glassfiber/epoxy and carbon fiber/polystyrene simulated invivo conditions (i.e invitro testing in saline conditions).



Figure 6: Carbon fiber reinforced thermoplastic hip prosthesis and conventional titanium equivalent. (Reproduced by courtesy of Orthodesign Ltd, Christ church UK.)

They showed only small changes in strength and stiffness of GF/epoxy composites whereas there was significant reduction in properties of CF/PS composites, which was attributed to poor fiber- matrix interfacial bond strength [90].

Thermosetting polymer matrix like epoxy reinforced with fibers are been evaluated for their use in orthopaedic applications [91]. Due to their variable biocompatibility and durability characteristics, they are left aside from mainstream applications [92]. In invivo applications of cured systems has some disadvantages associated with the release of unreacted monomer entities, if the polymerization is incomplete. Other reinforcing materials used in general composite technology like glass and aramid fibers, have gained less importance in orthopaedic applications. Recently bioglass fibers have gained more attention as possible reinforcement [93, 94].

Another type of reinforcing materials widely used are, particulate filler such as bioglass and calcium phosphates. They were primarily designed for dental application like GTR (guided

tissue regeneration). But due to osteoconductive properties of these fillers (HA), they have been widely used with all types of materials either by filling (polymer composites) or by coating (metal-ceramic). Among them, HAPEX™, which was developed and patented by Bonfield et al. consist of inert polyethylene matrix containing 40 vol% bioactive synthetic hydroxyapatite. HAPEX™ with different formulations have been tried from this group and has been successful. Resulting mechanical properties of these composites systems, especially modulus were 1-6 GPa, with highest values achieved for higher filling ratios. Tensile modulus and tensile strength increased significantly with increase in HA, while fracture strain reduced [83]. Cytocompatibility studies performed on these composites showed enhanced osteoblastic activity in terms of adhesion and proliferation, with increasing HA volume % [95]. Fillers like HA, which are considered to be bioactive, when used in matrix like PE shows low bonding efficiency. This is due to low surface area of HA available to bond with the neighbouring bone fragments. Recent advancement in ceramic technology has led to development of bioactive glass [96]. They are typically silicate glasses[93]. They react with physiological body fluids forming silica rich and apatite rich layers and form a tenacious bond to hard and soft tissues. Bioactive glass as reinforcing materials can improve high bone bonding efficiency with suitable matrix systems.

Inspite of large groups of materials which have been utilized for bone grafts, none of them are proved to be applied for clinical practice. Major drawbacks experienced are loosening of implant surface to that of bone and related inflammatory response associated with them. The latter is associated with the formation of membrane at the interface of bone and joint. Often there is giant cell reaction which causes inflammations [97].

Porous Structures

The structure and properties of three-dimensional polymeric scaffolds are of critical importance for their applications in tissue engineering. Scaffolds should possess maximum possible factors mentioned in table 1 [98, 99]. It should be possible to process these scaffolds into a variety of shapes and sizes. Furthermore, high porosity and high interconnectivity are required to minimise the amount of implanted polymer and to increase the specific surface area for cell attachment and tissue ingrowth, facilitating uniform distribution of cells, adequate transport of nutrients and cellular waste products. In addition, as specific cells require different pore sizes for optimal attachment and growth [100], much of the research is being aimed at obtaining polymeric scaffolds with a very high porosity and simultaneously, good control over pore size and morphology. Furthermore, the pore morphology can affect

the growth of cells and even alter its functions. Interconnected pores larger than the dimensions of the cells are essential for allowing infiltration of the cells into the scaffold, whereas smaller pores may positively influence the exchange of nutrients and cellular waste products. Therefore, an appropriate pore size range and distribution of pore sizes is beneficial to the viability and function of the cells within the tissue-engineering scaffolds.

Various methods have been used for the preparation of porous polymeric structures for biomedical applications and tissue engineering. Techniques involving phase inversion processes such as liquid–liquid phase separation and liquid–solid phase separation have been explored. Solvent removal by freeze-drying has frequently been used in the preparation of porous polymeric structures [101]. The morphologies and properties of the resultant scaffolds largely depend on the phase separation mechanism [102]. Liquid–liquid phase separation gives rise to isotropic pores of 1–30 μm in diameter, depending on the process parameters and the thermodynamics of the polymer/solvent system. Solid–liquid phase separation (with crystallisation of the solvent) leads to ladder- or sheet-like anisotropic morphologies, which strongly depend on the quenching rate [103]. In general, freezing at a relatively high temperature induces a low nucleation rate and a low crystal growth rate, which leads to a small number of large size solvent crystals. As a result, the average pore size obtained by freeze-drying increases with increasing freezing temperature [103, 104]. In methods based on the leaching of soluble particulates [105], the porosity can be effectively controlled by variation of the amount of leachable particles and the pore size of the porous structure can be adjusted independently of the porosity by using particles of different sizes. To improve the structure and increase the pore interconnectivity of the porous scaffold, particulate leaching has been used in combination with gas foaming [106], solvent casting [107], freeze-drying [108], immersion precipitation [109], and compression moulding [110].

2.2 Semi Crystalline Polymers

Semicrystalline polymers are the polymers, due to their regular structure, able to crystallize to a certain extent, yielding ordered structures. Crystallization takes place at temperatures well below the melting temperature with internal or external, e.g. stress induced, nucleation. Crystallization behaviour is strongly temperature dependent and freezes when the system reaches the glass transition. The overall mechanical properties of a semicrystalline polymer are strongly dependent on the degree of crystallinity as well as the size and orientation distribution of the crystallites. The chains between the crystallites remain amorphous. They are in their dynamical behaviour slightly restricted by the crystallites, mainly in the

immediate surroundings of it. This may increase the glass transition temperature slightly. If recrystallization occurs the dynamical behaviour can be changed drastically. In particular the behaviour during plastic deformation is strongly determined by changes in the confinement of amorphous chain segments by the crystallites due to recrystallization.

2.2.1 Morphology, mechanical properties and micromechanics of semicrystalline polymers

One common feature of semicrystalline polymers is a hierarchical morphology. The scales of structural details within them range from nanometers (or even less, i.e. angstroms) to millimetres. Under certain conditions these form periodic structures that involve adjacent chains or chain segments. Such preconditions include sufficient flexibility of chains, stereochemical regularity (tacticity) and others. In specific these segments in semicrystalline polymers like crystalline lamellae are arranged in different ways, from the parallel arrangement of a few shorter lamellae into sticks or bundles and longer lamellae into dendrites or sheaf-like structures, up to the radial arrangement observed in so-called “spherulites”, with diameters of up to several tens of microns. If the radial lamellae (or the radial segments) show periodic changes in their orientation, banded spherulites will arise.

These different hierarchical structures result from the contributing crystalline and amorphous phases present in the system. Different hierarchical structures varying in size and shape will ultimately lead to mechanical properties that are of technical interest. Nevertheless the mechanical behaviour demonstrated by the semicrystalline polymers is in turn related to morphology and micromechanical deformation processes. Figure 8 shows different mechanical behaviour experienced by semicrystalline polymers as observed in uniaxial tensile testing. Brittle behaviour at low temperatures is mainly characterized by fracture at low elongation, as shown in stress-strain curve (Figure 7b). The micromechanical mechanism that is typically associated with the brittle fracture of semicrystalline polymers is crazing. The craze structures that occur depend strongly on the type of brittle behaviour involved. Brittle fractures occur when a semicrystalline polymer is deformed at temperatures below the glass transition temperature of amorphous fractions (T_g). The lack of chain mobility limits the ability of the polymer to undergo plastic deformation, which is largely governed by the amorphous phase. This typically leads to embrittlement when ductile semicrystalline polymers are cooled to service temperatures.

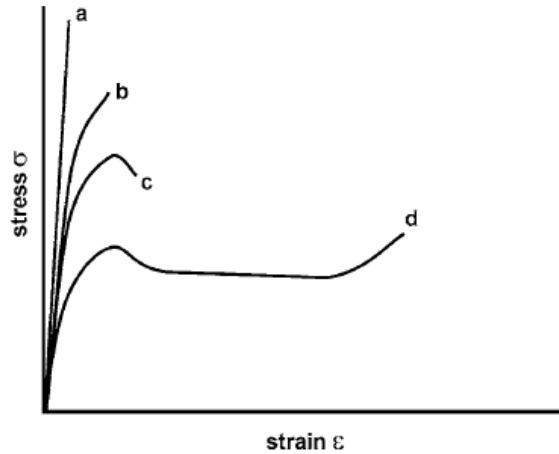


Figure 7: Typical Stress-Strain curves for semicrystalline polymers observed during tensile testing a) oriented fibers of high strength and modulus, b) semi brittle fracture, c) necking, d) cold drawing (Reproduced from [111])

Crazes propagate perpendicular to the direction of the applied load. The craze propagation is not influenced by morphological items like lamellar structures or spherulite boundaries. The structure of a craze in a semicrystalline polymer is similar to that of a craze in an amorphous polymer, like polystyrene.

Also brittle fracture is experienced with materials with low molecular weights. The craze propagation as in low molecular weight isotactic polypropylene (iPP) is comparable to the crazing observed at low temperatures. There is no influence of the lamellar orientations or spherulitic structures on the craze propagation. Brittle fractures are also influenced by morphological defects which may lead to early failure of the samples. Such a defect is interspherulitic defects. A weak interface, especially one involving large spherulites, results in brittle behaviour of semicrystalline polymers (Figure 7). Interlamellar defects-A lack of tie molecules that link the crystalline lamellae and an absence of entanglements in the amorphous portion leads to brittle behaviour. This defect type occurs at very high degrees of crystallinity (e.g. in PHB) or at low molecular weights. The crack path is clearly determined by the lamellar orientation (Intralamellar defects). There are several morphological defects of the crystalline portion resulting from polymer-specific factors, such as low molecular weight fractions, chain ends, and chain branching, that can initiate fracture at temperatures above T_g . Also brittle fracture is influenced by environmental stress cracking and also in many cases by physical aging.

The ductile behaviour of semicrystalline polymers is usually linked to neck formation, cold drawing and strain hardening. In the stress-strain curves (c) and (d) in Figure- 7 these events are reflected by a distinct yield point that is followed by a plateau region where the sample is

elongated by up to several times the original length. Under certain conditions the plastic deformation will proceed until strain hardening due to ongoing molecular orientation results in a significant increase in the mechanical stress. All of these escalating phases of plastic deformation proceed along with drastic changes in the semicrystalline structures on all hierarchical levels. Micromechanical mechanisms include conformational changes of macromolecules in the interlamellar (i.e. amorphous) as well as in the lamellar (i.e. crystalline) regions, the destruction and/or reorganisation of the crystalline phase, and the orientation of macromolecules.

2.2.2 Biodegradable semicrystalline polymers

Polyhydroxyalkonates (PHA) are the class of polyesters of hydroxyalkanoic acids (Has) (Doi 1990a). Steinbuechel and Valentin [112] reported 91 different PHAs incorporated into the biopolymer backbone and this number has now increased to 150. PHAs are reported to be biosynthetic, biodegradable and potentially biocompatible polymers with interesting properties similar to conventional petroleum derived plastics [113, 114]. Various microorganisms intracellularly produce PHAs as carbon and energy reserves, especially in harsh conditions, such as limited essential nutrients [115]. The general formula of PHAs is shown in Figure (8). PHAs can contain 3-5 methylene groups in the backbone (Doi et al. 1987) while various other substituent's can be incorporated into the side chains [116].

PHA's are diverse form of optically active biopolyesters synthesized by a wide range of microorganisms, usually under unfavourable growth conditions. Under such conditions PHA's are accumulated intracellularly as a carbon and energy reserve and may also serve as ion sinks [117]. As a consequence of their physiochemical properties and biodegradability, PHA's have received considerable attention to alternative thermoplastic polymers.

With ever interesting applications in the field of biomedical science, PHA's have been experimented with number of parameters. Since PHA's are sensitive to processing temperatures, efforts have been put to render the polymer system processable to conventional processing techniques either by blending or by chemical modification. PHA's can be separated into three groups depending on the number of carbon atoms in the side chain. Short chain length (scl) PHA's are composed of 3-5 carbon atoms, while medium chain length (mcl) PHA's consists of 6-14 carbon atoms and long chain length (lcl) PHA's comprise 15 and above carbon atoms [118]. However their monomers can be produced and randomly mixed in one polymer chain.

2.2.3 Polyhydroxybutyrate

The first PHA was discovered in *Bacillus megaterium* and classified as polyhydroxybutyrate (PHB) by Lemoigne [119]. PHB is scl PHB containing only 4 carbon atoms in monomer units which are joined together through ester bonds between 3-hydroxyl and carboxylic group [120] (Figure 8). It is a naturally occurring intracellular storage polymer with similar functionality to fat or glycogen for mammals and starch for plants. The inclusion bodies generally contain about 98% polymer and the rest is protein and phospholipids. PHB is the mostly characterized PHB. PHB and polypropylene (PP) have pendant methyl groups as side chains. Its physiomechanical properties were found to be similar to PP the exception of its percentage elongation to break, which is much less. Thus PHB is a brittle, crystalline material [113]. PHB has a right handed helix with a twofold screw axis and a fiber repeat unit of 5.56 to 5.90 Å. The helix is stable with methyl-carbonyl group interactions and represents as one of few exclusions of a helix found in nature that does not depend on H-bonding for its stability and synthesis. Other HAs, such as hydroxyvalerate (HV) and hydroxyhexonate (HX) were subsequently found in microorganisms from activated sludge [121]. Copolymers of PHB can be synthesized by co-feeding of substrates and the synthesis of HV or HB monomers was possible. PHBHV copolymers exhibit a phenomenon of isodimorphism, co-crystallization of the two monomer units in either of the homopolymer crystal lattice. It is also possible to alter copolymer fractions (HV) from 0 to 100 mol% by biosynthesis. The mechanical and physical properties of PHBHV copolymer vary widely depending on their comonomer composition. The raised level of HV content decreases the tendency to break during elongation but with reducing both tensile strength and young's modulus [122].

The families of PHAs exhibit a wide range of physiomechanical properties. The molecular weight (M_w) of PHB synthesized by wild type bacteria is in the range of 1×10^4 - 3×10^6 g/mol with a polydispersity index of around 2-3 depending on species, growth conditions, carbon source and polymer isolation method [113]. PHB is found to be an amorphous to a highly crystalline material with a degree of crystallinity (X_c) of 30-90% which has been influenced by its storage conditions [123]. In contrast at least 70% of PHB is amorphous and water soluble when it is in inclusion bodies within bacterial cells [124]. The crystal may be formed during purification step or after the pre-treatment with solvent and heat. The water removal of inclusion bodies may also promote the crystallization process. When the polymer is extracted, rapid crystallization takes place prior to cell disruption [115]. The densities of PHB in its amorphous and crystalline states are 1.18 and 1.23-1.26 g/ml respectively. The density of PHBV in the amorphous state is 1.177 g/mol and in the crystalline state is 1.20-1.25 g/mol

[125]. The X_c of PHBV copolymers with varying HV content is in the range of 30-80 mol% which is similar to PHB and is not dependent on monomer composition. Nevertheless Engelberg and Kohn[122] found that the copolymer with 22mol% HV was almost completely amorphous.

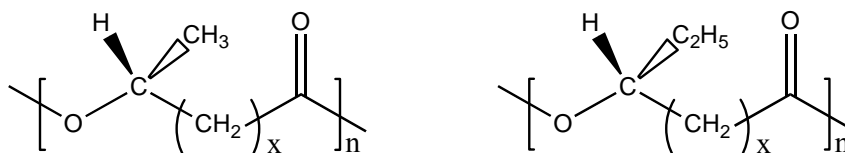


Figure 8: Formula for PHB and PHBV

2.2.4 Hydroxyapatite

Hydroxyapatite is a class of calcium phosphate-based bioceramic material, frequently used as a bone graft substitute owing to its chemical and structural similarity with natural bone mineral [126]. The HA derived either from natural sources or from synthetic sources is regarded as a bioactive substance because it forms a strong chemical bond with host bone tissue, and hence it is recognized as a good bone graft material. HA is not only bioactive but also osteoconductive, nontoxic, nonimmunogenic, and its structure is crystallographically similar to that of bone mineral. All the critical properties of the HA such as physiochemical, biomechanical, and biological are compiled and listed in Table 5, which makes HA a possible and perhaps the most appropriate bone graft material. The stoichiometric HA has a chemical composition of $\text{Ca}_{10}(\text{PO}_4)_6(\text{OH})_2$ with a Ca/P ratio of 1.67. Crystallographic studies are one of the important parameters for the selection of stoichiometric HA. A complete understanding of the crystal structure of HA can be acquired from the in-depth knowledge of the spatial orientation or organization of a small number of constituent ions. The unit cell, a basic structural pattern of the constituent ions, of HA is a right rhombic prism that forms a simple hexagonal crystal lattice (Figure 9).

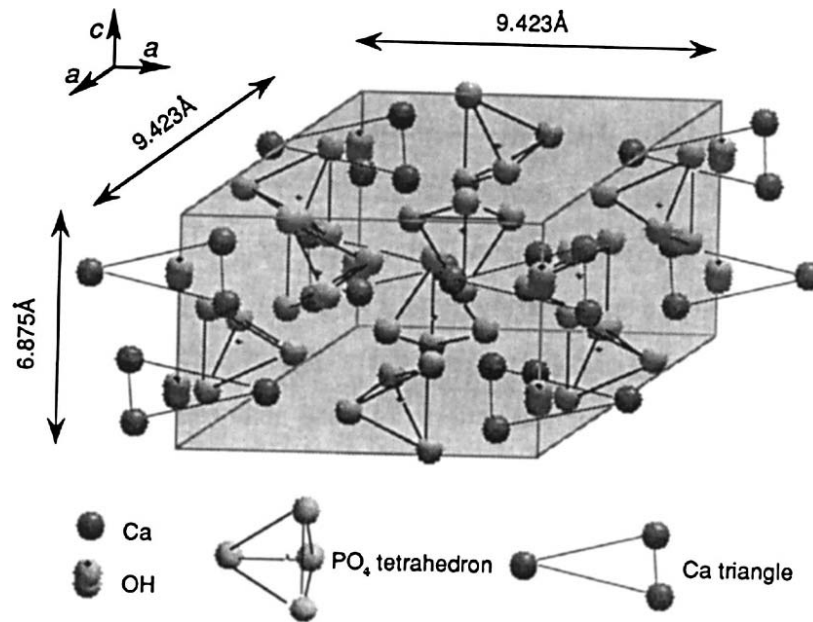


Figure 9: A diagrammatic view of crystal structure of HA. (Courtesy: Prof. H. Aoki, Tokyo Denki University, Japan)

The length along an edge of the basal plane of the unit cell is $a = b = 9.42 \text{ \AA}$ and the height of the unit cell is $c = 6.88 \text{ \AA}$ [127]. The spatial symmetry (i.e., space group) symbolized as $P6_3/m$, cannot be completely specified with fewer than this number of atoms. The arrangement of these constituent atoms is projected along the c -axis onto the basal plane. A schema of the crystal structure of HA viewed diagonally is shown in Figure 12 [127].

For simplicity, the chemical composition of HA can be written as $\text{Ca}_4(\text{I})\text{Ca}_6(\text{II})(\text{PO}_4)_6(\text{OH})_2$, where the Ca atoms occupy two series of nonequivalent sites. The Ca(I) atoms are on the fourfold symmetry 4(f) positions and the Ca(II) atoms are in the sixfold symmetry 6(f) position. The P atom is surrounded by four atoms and forms a tetrahedron. The PO_4 tetrahedron is almost regular with only slight distortion. The hydroxyl ions lie, in projection, at the corners of the rhombic base of the unit cell. Furthermore, hydroxyl ions are always perpendicular to the nearest plane of calcium with the hydrogen ion facing away from this plane in such a way that the O–H band never overlaps the plane. Of course, the crystal structure and crystallization behaviour of HA are strongly dependent on the substitution nature of the ionic species and the pattern ordering. Even the crystal structure can be changed by the manipulation of the calcium to phosphorous (Ca/P) ratio, which leads to possible changes in their solubility. As per a literature survey, HA has a long history of being used as a good bone graft.

Table 5. Critical properties of HA (Compiled from [12, 128-131])

Properties	Experimental data
Chemical composition	$\text{Ca}_{10}(\text{PO}_4)_6(\text{OH})_2$
Ca/P molar	1.67
Color	Mostly white
Crystal system	Hexagonal
Space group	$\text{P6}_3/\text{m}$
Cell dimensions (Å)	$a = b = 9.42, c = 6.88$
Young's modulus (GPa)	80–110
Elastic modulus (GPa)	114
Compressive strength (MPa)	400–900
Bending strength (MPa)	115–200
Density (g/cm^3)	3.16
Relative density (%)	95–99.5
Fracture toughness ($\text{MPa}\cdot\text{m}^{1/2}$)	0.7–1.2
Hardness (HV)	600
Decomposition temp.(°C)	>1000
Melting point (°C)	1614
Dielectric constant	7.40–10.47
Thermal conductivity ($\text{W}/\text{cm}\cdot\text{K}$)	0.013
Biocompatibility	High
Bioactivity	High
Biodegradation	Low
Cellular compatibility	High
Osteoinduction	Nil
Osteoconduction	High

It is possible clinical usage range from augmenting atrophic alveolar ridges to repairing long bone defects, un-united bone fractures, middle ear prostheses, spinal fusions, cranioplasty, craniofacial repair, and vertebral fusions, which has been discussed earlier. Basically, HA is a family of apatite phase. The name apatite was derived from the Greek word, meaning “to deceive,” which was coined by Werner in 1786 [132]. Apatite belongs to a family of components having similar structure but not necessarily having identical phase composition. The first synthesis of apatite was carried out by Daubree in 1851 [133], in which apatite was produced by just passing phosphorous trichloride vapour over red hot lime. Since then numerous methodologies have been established for the synthesis of micron sized HA. In the past few years, significant research efforts have been devoted to the production of nanosize HA in order to obtain high surface reactivity with adequate physical, chemical, and biological properties similar to natural bone mineral. The nano HA has unique advantages over

conventional micro HA in terms of high surface area-to-volume ratio and ultrafine structure, which are the most imperative properties essential for cell–substrate interactions in vivo. For example, compared to conventionally crystallized HA, nanocrystallized HA promotes osteoblast cell adhesion, differentiation, proliferation, osteointegration, and deposition of calcium-containing minerals on their surface, thereby enhancing new bone growth within a short period. The nano HA can be synthesized by many different methods, which include solid state, wet chemical [134], hydrothermal [135], mechanochemical [136, 137], pH shock wave [138] , and more recently microwave processing [139].

2.3 Nanocomposites

2.3.1 Bone as a model nanocomposite

Bone is a complex dynamic tissue, which is structurally and mechanically heterogeneous, owing to spatial distributions in the shape, size and composition of its constituent building blocks. This varied arrangement of material structures at different length scales makes it a hierarchical nanocomposite (Figure 10). Bone has diverse mechanical, biological and chemical functions; such as structural support, protection and storage of healing cells, and mineral ion homeostasis. The homeostasis refers to the fact that bone is a repository of various ions such as calcium, potassium, carbonate, magnesium, strontium, chloride or fluoride. Macroscopically, bone shows significant variations in mechanical properties at different anatomical locations, [140] and are thought to develop in response to applied stress. (Wolff's Law) The internal architecture is adapted in terms of change in density and in disposition of trabecules and osteons and the external conformation in terms of shape and dimensions. Hence, bones like scapula and hip bones, which are designed to take less damping loads are broad and flat; whereas long bones like tibia and femur, which are hollow, can withstand higher bending forces, a design optimized for their function.

Bone is composed of varied number of substance, which makes it a complex natural composite. It consists of approximately 70% of mineral and the remaining 30% is accounted for proteins. Bone, in general, is a well-organized connective tissue made of several building blocks at multiple levels that consist of, in decreasing proportions, minerals, collagen, water, noncollagenous proteins, lipids, vascular elements, and cellular components. The strength and stiffness of bone is due to its hierarchical organization of building blocks, which are self assembled into unique structures. Collagen acts as structural framework in which HA crystals are embedded (Figure-11)

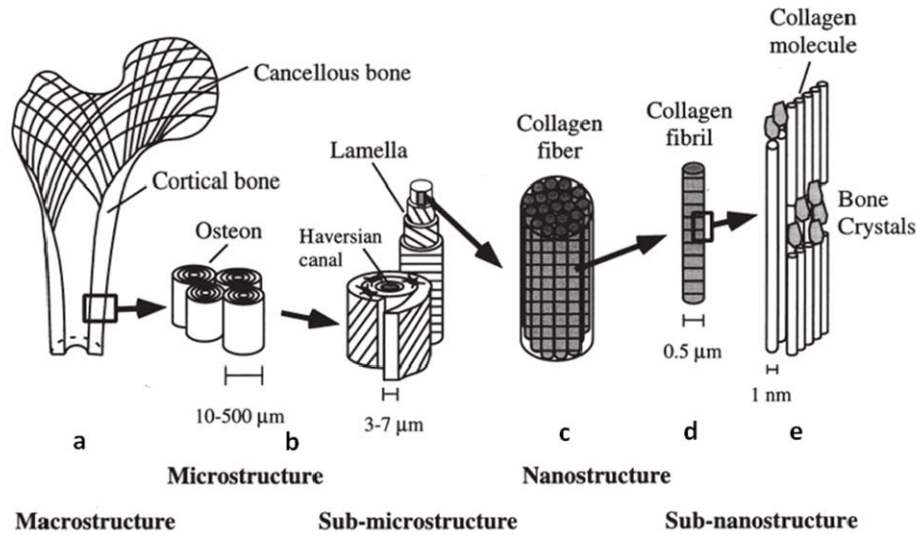


Figure 10: Hierarchical structural organization of bone: (a) cortical and cancellous bone; (b) osteons with Haversian systems; (c) lamellae; (d) collagen fiber assemblies of collagen fibrils; (e) bone mineral crystals, collagen molecules, and non-collagenous proteins. (Reproduced from [141])

Also, there is unique arrangement of nanocrystals inside the collagen matrix where the crystals are not directly bounded to collagen, rather they are connect to the matrix through non collagenous proteins. This arrangement of nanocrystals is accomplished by a process called biomineralization, where noncollagenous proteins server as primary nucleation sites for crystal growth.

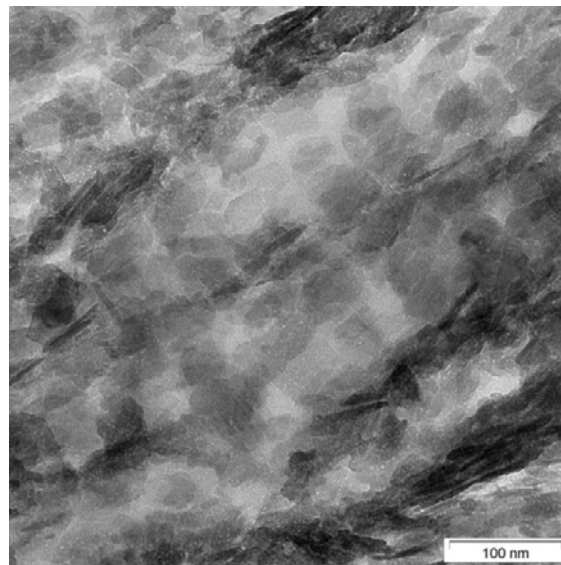


Figure 11: Bone nanostructure: Arrangement of hydroxyapatite nano-platelets in the collagen matrix; EFTEM image[142]

Bone at macrostructural level can be distinguished as cortical (compact) and cancellous bone (fibrous). The dimension-dependent hierarchical structure of the bone tissue is shown in Figure-10. The spongy bone occupies about 20% of the total bone. It is also often called

trabecular or cancellous bone. It is lighter and lesser dense than compact bone. It has high porosity and a higher concentration of blood vessels compared to compact bone. The porous architecture is easily visible under the lower-power microscopes and/or even to the naked eyes if the pores are very large. The diameter of the pores may be from a few micrometers to millimeters. On the other hand, compact bone is much denser than spongy bone. It is also called cortical or dense bone. It occupies about 80% of the total bone. It has less porosity and thus it has less concentration of blood vessels. Its porous architecture is not visible to naked eyes owing to less porosity. They may be perhaps 10–20 μm in diameter and are mostly separated by intervals of 200–300 μm . Compact bone functions mechanically in tension, compression, and torsion, whereas spongy bone functions mainly in compression.

The microstructure of cortical bone comprises of mineralized collagen fibers, which are in the form of planar arrangements called lamellae (3–7 μm wide). Figure 12 shows the architecture of cortical bone. The dark field in TEM images are the individual osteon. In some cases these sheets (lamellae) of mineralized collagen fibers wrap in concentric layers (3–8 lamellae) around a central canal to form what is known as an *osteon* or a *Haversian* system. The osteon looks like a cylinder about 200–250 μm in diameter running roughly parallel [143] to the long axis of the bone. Other forms of cortical bone where the mineralized collagen fibers are less well registered and no pattern can be distinguished are called *woven* bone. In some forms of bone, the lamellae are overall tangential to the outer surface of the bone (without forming osteons), and together with woven bone tissue, form a larger plywood-type stacking of thicker layers (150–300 μm) around the complete circumference of the bone in what is called *lamellar* bone (Figure 12).

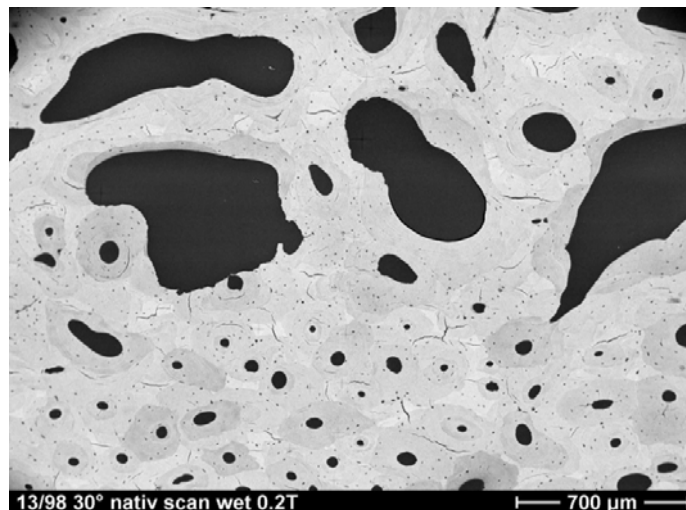


Figure 12: Architecture of compact bone: Osteons of different mineralization density; ESEM image, BSE material contrast.[142]

Cancellous bone is made of an interconnecting framework of trabeculae in a number of combinations, all comprising the following basic cellular structures: rod–rod, rod–plate, or plate–plate. A trabecular rod is about 50–300 μm in diameter.

2.3.2 Particulate filled polymer nanocomposites

Particles used to reinforce polymers include ceramics and glasses such as small mineral particles (e.g. Al_2O_3 , CaCO_3 , talc etc.), quartz or glass powder, metal particles such as Ni, Cu, Ag, Al or Fe, and occasionally also organic particles of wood, rice hulls or starch [111]. Most mineral particles are typically used to increase the modulus of the matrix, to increase wear and abrasion resistance and surface hardness, to improve performance at elevated temperatures, to reduce friction and shrinkage, and to decrease the permeability of the matrix. Sometimes they are also just used to reduce the cost of the polymer. In contrast, metal particles are mainly used to improve the electrical conductivities of most insulating polymer matrices. The diameters of the particles vary from several μm up to <100 nm, and information on the shapes and types of particles present can be discerned. Such broad diameter distributions are advantageous for realising high filler contents, since the spaces between the large particles are filled with smaller particles. A general problem encountered during the preparation of highly filled polymers is incompatibility between fillers and polymers, which impedes the uniform dispersion of particles.

2.3.3 Transition from micro to nanoparticles

The transition from microparticles to nanoparticles yields dramatic changes in physical properties. Nanoscale materials have a large surface area for a given volume [144]. Also the transition from nanodimensions to micron particles influences the filler to volume ratios. For eg, the number of filler particles at a given volume fraction rapidly increases as the size of particles decreases (Figure 13). As a consequence, compared to polymer composites with the conventional fillers (in the micron range), which nominally requires loading of 20 wt% or more, the distances between nanoparticles are drastically reduced to the nanometer range, even when relatively low concentrations of nanofillers are used. Also the sizes of the nanoparticles are comparable to the radius of gyration of the macromolecules in the polymer matrix, so that the morphological development of polymer matrix can be substantially affected by the dispersed nanoparticles (morphology under constraint condition). Finally, the nanoparticles provide ultrahigh specific surfaces, and this huge interfacial area permits strong interactions with the polymer matrix. As a consequence, the amount of modified polymer

interface relative to the total volume will be significantly increased, corresponding to the transition from a polymer matrix material to a quasi-polymer interfacial material.

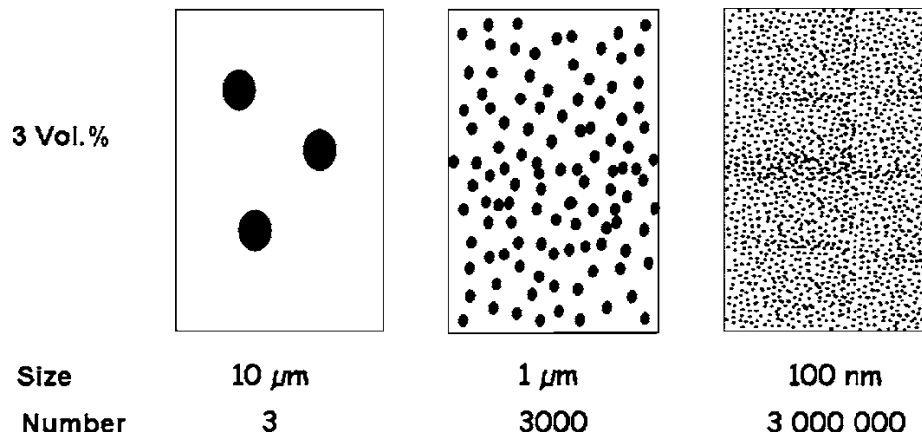


Figure 13: Illustration of how the number of particles increases as the particle size decreases at a constant volume content [111].

Shape factor may also account for differences in the properties, since many important chemical and physical interactions are governed by surfaces and surface properties, a nanostructured material can have substantially different properties from a larger-dimensional material of the same composition. In the case of particles and fibers, the surface area per unit volume is inversely proportional to the material's diameter, thus, the smaller the diameter, the greater the surface area per unit volume [144]. Common particle geometries and their respective surface area-to-volume ratios are shown in Figure-14. For the fiber and layered material, the surface area/volume is dominated, especially for nanomaterials, by the first term in the equation. The second term ($2/l$ and $4/l$) has a very small influence (and is often omitted) compared to the first term. Therefore, logically, a change in particle diameter, layer thickness, or fibrous material diameter from the micrometer to nanometer range, will affect the surface area-to-volume ratio by three orders of magnitude. In general, nanomaterials provide reinforcing efficiency because of their high aspect ratios [144]. The properties of a nanocomposite are greatly influenced by the size scale of its component phases and the degree of mixing between the two phases. Depending on the nature of the components used (layered silicate or nanofiber, cation exchange capacity, and polymer matrix) and the method of preparation, significant differences in composite properties may be obtained [145].

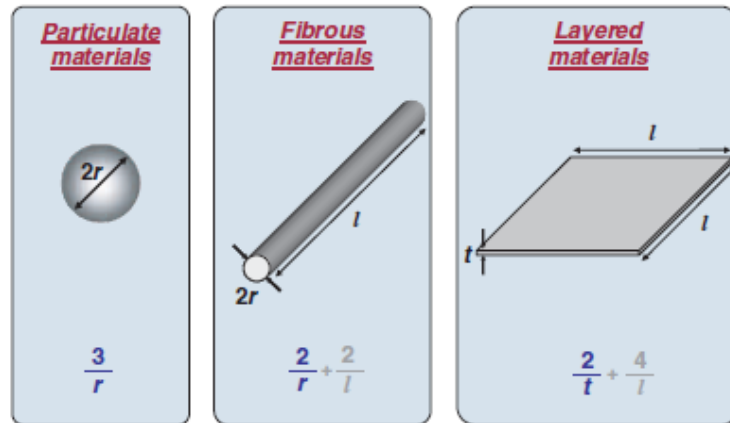


Figure 14: Common particle reinforcements/geometries and their respective surface area-to-volume ratios. (Reproduced from [146])

2.3.4 Biomimetic nanocomposite – A new approach

The application of synthetic single-phase graft components has always been limited by their property combination necessary to serve as bone implant. Thus, considerable attention has been paid to composites. The term composite can be defined as a heterogeneous combination of two or more materials, differing in morphology or composition on a microscale, in other words, a microcomposite [147]. Composite grafts are a good choice among the synthetic bone grafts owing to the possibility of incorporating most of the favourable features of various single-phase components and to eliminate or minimize the problems associated with the monolithics as discussed in previous sections. The composite, therefore, can be treated as the only material that uniquely exhibits a range of properties equivalent to bone, and thus it could be possible to eliminate some of the problems associated with current synthetic bone grafts. As bone is a dynamic living tissue, it should be noted that unless we make bioactive bonelike composites with intact favourable osteoinductive and/or osteogenic components, synthetic bone grafts would only have limited survivability. Accordingly, much attention has been paid to the manufacture of bioactive composites over the past two decades. An important advantage of the bioactive composite lies in its strong interfacial bonding ability with host tissue and its improved mechanical strength. It is, therefore, possible to match certain properties of the bioactive composites to natural bone.

Considerable attention has been paid in the past two decades to bioactive composite grafts that consist of bioactive ceramic filler in a polymeric matrix. As previously discussed, bioactive composite based on HA and PE developed by Bonfield et al. was used as bone substitute [148, 149] Unfortunately, it is not successful as a bone graft, which limited its wider usage in clinical medicine. Now, it is primarily being used as a middle ear implant,

which is one of the promising bioactive composite grafts used for such an application. Simultaneously, bioresorbable composites are developed and investigated as bone grafts. A composite based on HA and collagen has been developed and investigated [150]. It shows great promise because of its resemblance to natural bone in terms of biocompatibility and bioactivity.

Biomimetic nanocomposites have gained much interest and are perceived to be beneficial over microcomposites in many aspects as bone grafts, which, of course, open a new arena in the field of bone grafting. Nanocomposites play a pivotal role in bone grafting as a new class of bone graft material owing to their amazing characteristics, including larger surface area-to-volume ratio and superior mechanical strength, which uses a combination of several nanoscale bone graft materials and/or in conjunction with osteoinductive growth factors and osteogenic cellular components. The latter are supplement stimuli for bone growth. The term nanocomposite can be defined as a heterogeneous combination of two or more materials in which least one of those materials should be in a nanometer-scale range. It is surprising to realize that most biological systems begin with a nanoscale mechanism that might be the basis for the success of their unbelievable characteristic functions. For example, bone is the toughest natural nanocomposite, precisely evolved by nature's proficiency in using a nanoscale hierarchical assembly with the basic ingredients of HA and collagen; therefore researchers are trying to imitate such a process, through so-called biomimetics, for making nanocomposite materials into synthetic bone grafts and perceiving these to be the right choice over microcomposites. Therefore, it is considered that engineering nanocomposite bone grafts through the biomimetic approach is a somewhat new class of method.

2.3.5 Hybrid nanofibers

A new class of nanocomposites nanofibers based on organic and inorganic species combined at a nanoscale has recently obtained more attention. These so called organic-inorganic hybrids have both the advantages of organic materials, such as light weight, flexibility and good moldability, and inorganic materials, such as high strength, heat stability and chemical resistance. These nanocomposite nanofibers have been fabricated by many different processes and electrospinning is the most important cost effective process. These nanocomposite nanofibers are expected to find applications in semiconductor devices, tissue engineering, aerospace and others. Larsen et al. were the first to combine electrospinning with sol-gel methods to design vesicles and nanofibers made from inorganic oxides and

hybrid (organic/inorganic) materials with diameters in the micrometer and submicrometer range [151].

Xia and co-workers [152] extensively studied the formation of polymeric and ceramic nanofibers as uniaxially aligned arrays as well as the fabrication of composite and ceramic hollow nanofibers by electrospinning. One main advantage of fabrication of nanofibers via electrospinning is that, using electrospinning it is possible to combine different materials (hybrid materials) to form fibers with different structural arrangements. For eg, nanofibers composites have been fabricated by ES with very good dispersion of nanoparticles inside the matrix fiber. Also it is possible to fabricate core-shell structures with controlled ratios. Hollow and porous nanofibers can be produced for different applications.

3 Materials and Methods

3.1 Materials

3.1.1 Polymers

Poly (3-hydroxybutyrate) PHB, a biodegradable polymer was used as matrix polymer. Three different PHBs varying in molecular weight and source have been used in this work for various experiments. Additionally a copolymer, Poly (3-hydroxybutyrate-co-hydroxyvalerate) (PHBHV) with 12 mol% hydroxyvalerate was also used. Table-1 shows different matrix polymers and their molecular weights.

Table 6: Properties of polymers from different source

Polymer	Source	Mw (g/mol)	Form
PHB (Methanomer)	UFZ (Leipzig)	1.2×10^6	dissolved in chloroform
PHB (Sigma)	Sigma-Aldrich	4.4×10^5	granules
PHB(Biomer)	Biomer AG	4.5×10^5	fine powder
PHB 12% HV	Sigma-Aldrich		granules

3.1.2 Nanoparticles

Two different nanofillers of HA varying in shape and size were used as particulate filler. a) OSTIM[®]-HA, a needle shaped nanoparticle as a 35% suspension in water and with a mean diameter of 18-30 nm was purchased from Heraeus, Deutschland and b) HA nanopowder (spherical shape) with the average particle diameter of 150-200 nm was obtained from Sigma Aldrich, Germany. Surface area and aspect ratio of fillers were calculated based on the L and D values specified by the manufacturer and also were compared by our laboratory investigations of by image analysis of TEM micrographs of nanofillers using image analysis software. These fillers were also used without further processing. Additionally nano HA synthesized from wet chemical method were also used. (Section 4)

3.1.3 Chemicals and auxiliary materials

Solvents

The number of solvents used in this work depends on the type of polymer and also the mode of fabrication. All the solvents used were of analytical grade and were used without further processing steps like purification. Table 1 gives the list of solvents used in this work.

Table 7: List of solvents for different polymers used.

Polymer	Solvent	Fabrication
PHB	Chloroform	nanocomposite film
PHBHV	Chloroform	nanocomposite film
Nanoparticle	Ethanol	Dispersion
PHB	Chloroform, Dichloromethane	Electrospinning
PHB	Dimethyl Formamide	Etching
Nanoparticle	Methanol, ethandiol ammonia	nanoparticle synthesis

Simulated Body fluid (SBF)

Simulated body fluid (SBF) was used as it contains inorganic ion concentrations close to those in blood plasma[153].

3.2 Fabrication of Materials

3.2.1 Synthesis of Biomimetic hydroxyapatite

A solution of 0.125M $\text{Ca}(\text{NO}_3)_2 \cdot 4\text{H}_2\text{O}$ (analytical grade) prepared in SBF, whose composition is shown below in figure 16 was used as the calcium source, the pH of which was raised to 9 using 1:2 solutions of aqueous ammonia and SBF respectively. A solution of 0.75M $(\text{NH}_4)_2\text{HPO}_4$ prepared in SBF was added drop wise to the calcium source under constant stirring until it reached the physiological pH of 7.4. The reaction temperature was maintained at 37°C. The resulting product was centrifuged, washed thoroughly with double distilled water and dried in air oven at 80°C. The dried cakes were powdered using mortar and pestle. The powders were then sintered at various temperatures for characterisation (Figure 15).

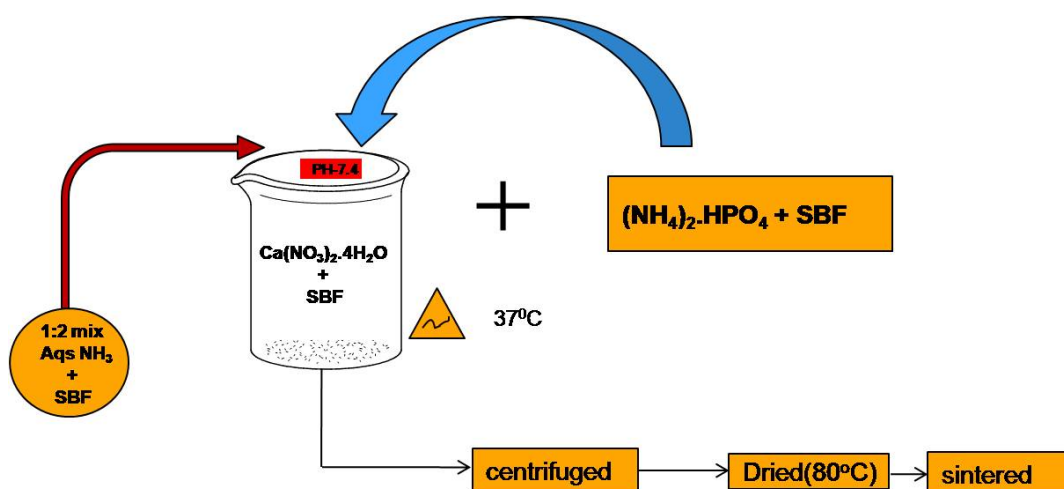


Figure 15: Synthesis of HA by precipitation method

3.2.2 Preparation of simulated body fluid

Simulated body fluid (SBF) was prepared by dissolving reagent grade chemicals of sodium chloride (NaCl), sodium hydrogen carbonate (NaHCO₃), potassium chloride (KCl), dipotassium hydrogen phosphate (K₂HPO₄ · 3H₂O), magnesium chloride hexahydrate (MgCl₂ · 6H₂O), calcium chloride dihydrate (CaCl₂ · 2H₂O), sodium sulfate (Na₂SO₄) and tris-(hydroxymethyl) aminomethane, into distilled water and buffered to pH 7.25 at 37°C with hydrochloric acid (HCl). Synthesized HA particles were again immersed in SBF for specific time at controlled temperature (Figure 16)

Preparation of simulated body fluid (SBF)

Recipe

NaCl

NaHCO₃

K₂PO₄·2H₂O

MgCl₂·6H₂O

CaCl₂

Ionexchange water

50 mM (CH₂OH)₃CNH₂ (trishydroxymethyl aminomethane)

45 mM HCL

buffered at 7.4pH

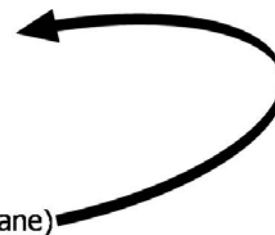


Figure 16: Preparation of simulated body fluid (SBF)

3.2.3 Synthesis of nano-hydroxyapatite by wet chemical method

The nano-HA particles were synthesized from calcium and phosphorous precursors by wet chemical method as follows [154] Briefly 1.82 g amount of Ca(OH)₂ (95%, Sigma) was suspended in 4 ml milliQ water using a stirrer. The Ca (OH)₂ suspension was heated to 70°C, and the pH of the suspension was adjusted to pH 11-12 with the addition of 60 ml of NH₃ (32%, CarlRoth). 1 ml of H₃PO₄ (85% CarlRoth) was added drop wise to the rapidly stirred suspension over a period of 5 min. The HA suspension obtained was covered and kept stirring at 70°C for a period of 2 hr. Then the suspension was centrifuged to collect the nanoparticles. Obtained nanoparticles were further vacuum dried at 80°C (Figure 17).

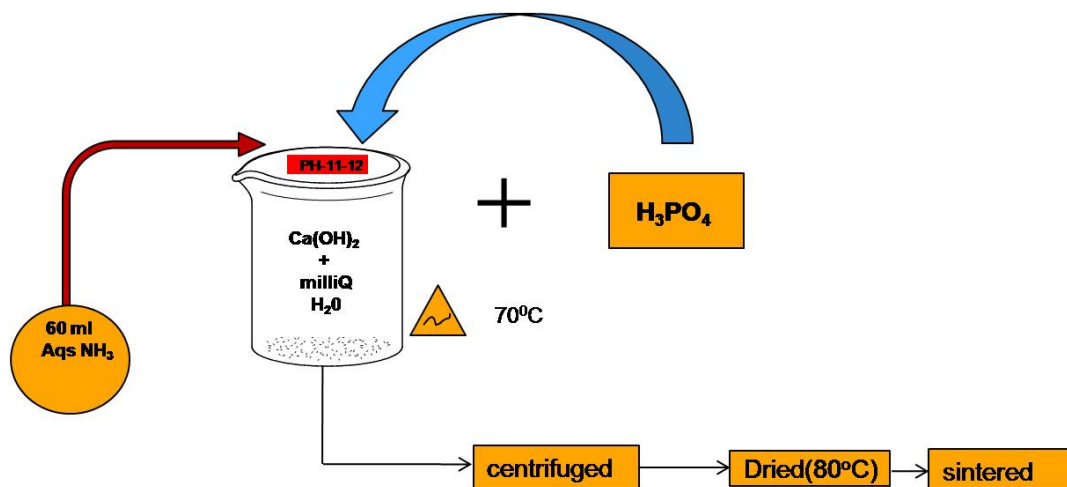


Figure 17: Synthesis of nano HA by wet chemical method

3.2.4 Preparation of nanocomposites

Nanocomposites with different filler loadings (10 and 20 wt %) were prepared as follows. Briefly the polymers, PHB and PHBV were dissolved in chloroform at 60°C for until it is homogenized. HA nano crystals in the form of paste were dispersed in a solvent by sonicating for 20-30 minutes at minimum amplitude (Vibrosonic Sonicator) of 21% just to avoid thermal degradation due to increase in temperature of sonicated solution. The dissolved solution of PHB was transferred in the sonicated solution of HA at slow rate and again sonicated for another 10 minutes. HA was dispersed in ethanol because the OSTIM nanoparticles are obtained from the producer in the form of suspension in water and as a result only polar solvents can help splitting of nanoparticle agglomerates effectively. The resulting nanocomposite solution was casted on a petridish and evaporated at room temperature until the last traces of solvents are removed. Additionally the nanocomposite was redissolved in chloroform just to make sure the phase separation caused by ethanol and chloroform which results in micrometer sized pores, which can cause decreased mechanical properties. Nanocomposite films were casted on a fine glass plates using film applicator for desired thickness (ELCOMETER 3570) or by using in-house designed film applicator which uses a glass rod and the metal wire spacers tied to them. Finally the nanocomposite films were vacuum dried for 24 hrs to remove traces of solvents.

3.2.5 Preparation of porous films by immersion precipitation

Films were prepared by casting chloroform-PHB solution on a glass plate, normally used as sample holders for optical microscopy and immediately introduced into the coagulation bath.

The temperature of the bath was kept at $25\pm 2^{\circ}\text{C}$. The initial casting thickness was maintained at 200 μm . Coagulation baths with the following ethanol-chloroform (wt %) compositions were used: 100:0, 90:10, 80:20, 70:30, 60:40 and 50:50. Ethanol-chloroform solutions were prepared by mixing different amounts of ethanol and chloroform in order to obtain the final desired composition. The mixture was stirred for 10 min at room temperature before use. Solvents were used as it is, without any purification.

3.2.6 Preparation of porous structures by freeze drying and particulate leaching

Predesignining of sugar/salt template

Sugar or salt templates were prepared as follows. Commercially available salt granules of cell culture grades were finely powdered in Laboratory high speed mixer (Analysenmühle A10, Janke & Kunkel GmbH). Obtained powder was then sieved for different grain sizes. To obtain various shapes, these powders were gently stuffed PTFE plastic o-rings in the size range of Id-5mm and t-2mm. Then they were fused with either of the two methods as suggested by Jan Feijen et al.

1. Sugar or salt particles with certain size ranges were first soaked in a mixture of acetone and water (4.5/0.5 v/v), then gently packed into a PFFT rings with the shape in the form a disc. After drying, they were gently transferred in desiccators with relative humidity of 75% for 2 days. The templates were then removed from the rings.
2. Sugar or salt particles with certain size ranges were first soaked in a mixture of acetone and water (7.5/2.5 to 9/1 v/v), then gently packed into a plastic container with desired shape and size. After drying, the sugar or salt template could be removed from the container.
3. Commercially available sugar cubes were also used for comparison.

Freeze drying and particulate leaching

Porous polymeric scaffolds were first prepared by a combination of freeze-drying and particulate leaching. PHB or PCL was dissolved in chloroform at 48°C temperature to make a 10 w/v% solution. The nanocomposite solution was prepared in the same way as that prepared for compact films. Then the sugar or salt templates were dipped in nanocomposite solution fixed to Rotavapor R-210 equipped with vacuum pump. Vacuum was applied repeatedly by varying the pressure in between 200-350 mb for a period of 1 hr. Subsequently the sugar /salt templates in which polymer was forced to penetrate were frozen using liquid

nitrogen for few minutes and then transferred to deep freezer maintained at $-80\text{ }^{\circ}\text{C}$ for 24 h. After phase separation, the solvent crystals were removed by freeze-drying for a period of 2–3 days in vacuum using ALPHA 1-4 LSC at a vacuum of 0.04mb and temperature $-41\text{ }^{\circ}\text{C}$. Subsequently the structures were gently stirred in demineralized water with repeatedly changing the water three times a day for about a week to leach out the sugar/salt. The resulting 3 dimensional porous nanocomposite scaffold was vacuum dried.

3.2.7 Preparation of porous scaffolds using melt infiltration technique

PCL (Aldrich, Germany) was melted at $60\text{ }^{\circ}\text{C}$ and then the melted polymer along with nanohydroxyapatite was sonicated for few minutes to disperse the filler uniformly. Then the suspension was transferred in a metal mold containing commercially available sugar templates which was preheated at $60\text{ }^{\circ}\text{C}$ inside a heating chamber (MEMMERT PM 200) equipped with vacuum pump. Repeatedly vacuum was applied in the range between 50-15mb just to force the melt inside the pores. After complete solidification of melted PCL/HA composites, they were removed and then subsequently leached out the sugar particles in demineralized water for about a week.

3.2.8 Preparation of nanofibers via electrospinning

Experimental setup for electrospinning

Electrospinning was performed on nanocomposites solutions in two different mode. The composite solution was prepared as described in section 2.1. A known amount of nanocomposite material which was prepared as described in the previous section, was dissolved in suitable solvent and then sonicated again for few minutes without allowing more solvent to evaporate. Different solution parameters were investigated and will be discussed in the later sections. A typical electrospinning setup consists of following different components. A high voltage source with one end (positive) attached to syringe tube with a needle and other end attached to collector which is grounded. Polymer solution is forced at constant flow rate through infusion pump. Figure 18 demonstrates typical electrospinning setup.

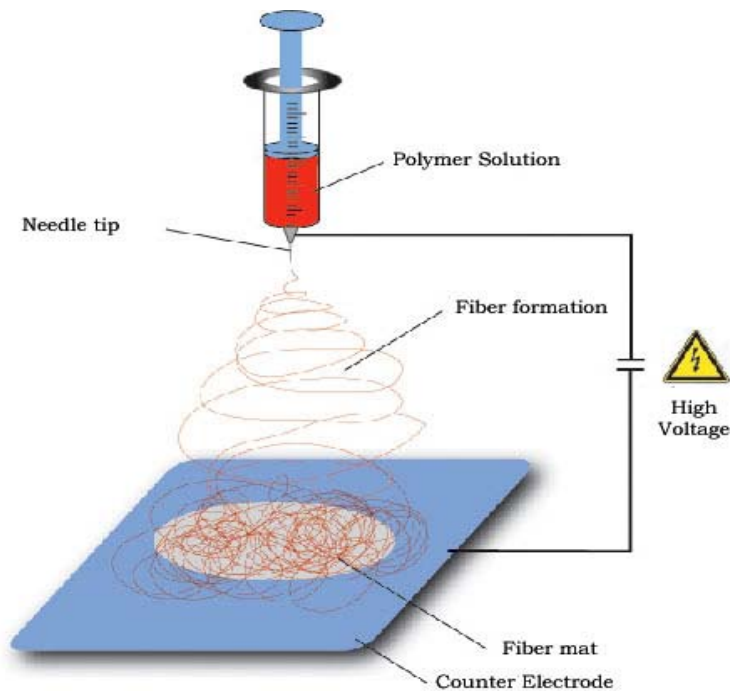


Figure 18: Schematic diagram of electrospinning apparatus

Conventional electrospinning setup

The polymer nanocomposite solution was filled in a 1 ml syringe equipped with a blunted steel needle of 0.8 mm inner diameter, which was finely grinded using sandpaper. A wooden plank was covered with thin copper sheet, which was used as collector plate. The distance of the needle to collector plate was varied according to the need. Electrospinning was carried out at room temperature in a vertical spinning configuration, using applied voltages in the range from 7 to 20 kV, driven by a high voltage power supply (HEINZINGER PNC, Germany) with a flow rate of 100 ml/h. Electrospun fibers were collected on various substrates for investigations. Samples for SEM was spun on glass slides while carbon coated copper grids were used for TEM investigations. Also spun fibers were collected on nonwoven steel fabric for further analysis.

Setup for aligned nanofibers

For aligned nanofibers, the collector plate is constructed by using two parallel electrode. Two parallel copper electrodes were fixed on the insulated plank. These two electrodes were connected through wire from behind and this was connected to ground terminal via alligator clip. The distance between the parallel electrodes was predefined for a particular collector distance (Figure 19).

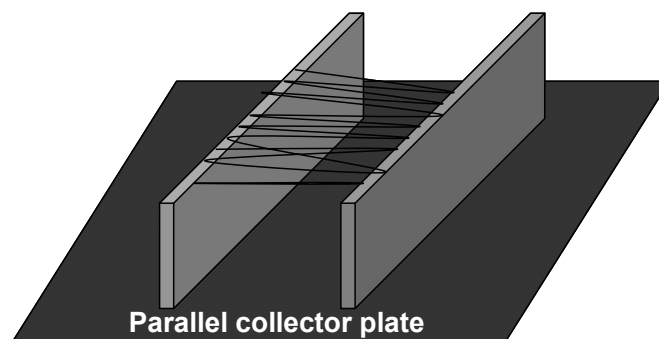


Figure 19: Schematic representation of parallel plate electrodes for aligned nanofibers

3.3 Methods

3.3.1 Microscopy

Light microscopy

Morphological observation of banded spherulites was analyzed by Leica DMLP microscope (Germany) with CCD camera attached to the system. In the first step PHB/HA and PHBHV/HA solution casted nanocomposite films which were prepared by glass casting were used. A 6x6 mm film from that were cut and fixed to standard optical microscopy cover glass slide. These samples were then melted on a hot stage maintained at $198\pm 2^\circ\text{C}$ for 2 min and then immediately transferred onto another hot stage maintained at specified temperature for isothermal crystallization. A set of four crystallizations temperatures (25°C , 90°C , 110°C and 130°C) were selected. All the samples were crystallized at specified temperatures for about 24 hrs. Samples were kept in desiccator until the investigations were performed. Then observation of spherulite growth was performed by Leica DMLP microscope (Germany) with CCD camera attached to the system. Measurement of spherulite diameter and bandwidth were performed using image analysis software.

Scanning electron microscopy and EDX

Morphology of nanocomposites, nanofibers and porous scaffolds were performed on scanning electron microscopy JEOL JSM 6300 equipped with tungsten cathode. Accelerating voltage was selected as a function of mode and sample sensitivity and was maintained between 15 and 25 KV. The images were recorded and stored with digital picture archiving (BOERDER), coupled with the instrument. Both secondary electron (SE) and backscattered imaging was used for topography and contrast.

Samples of nanocomposite films were prepared by standard procedure. Thin solution cast

films were fixed using double sided carbon tape and then coated with gold or carbon for SE and BSE imaging. Fractured surface of the same films were done using cryofracture (using liquid N₂) due to their ductile behaviour.

Additionally melt crystallized samples were etched prior to imaging. The etching procedure used was according to Olley et al. and was modified to the required conditions. In brief, the etching was done as follows.

- PHB and PHB/HA nanocomposite films were pressed on a hot stage and then quenched in hot water which was maintained at 70°C
- These samples were shaken in a reagent (etchant as in table-4) at room temperature for specified time.
- Samples were then washed with 20% glacial acetic acid in water and then rinsed with distilled water until the traces of reagents were removed.
- Then the samples were allowed to dry at room temperature.

Table 8: Composition of etching reagents

Number	Composition and procedure	Etching time (in min)
1	600 mg KOH in 4 ml methanol + 2ml ethandiol	90
2	600 mg KOH in 4 ml methanol + 2ml ethandiol	30
3	300 mg KOH in 4 ml methanol + 2ml ethandiol	60
4	300 mg KOH in 4 ml methanol + 2ml water	105

Electrospun nanofibers which were spun directly on standard optical glass slide was fixed to specimen stub and then coated with gold. Nanofiber mats were transferred directly on glass support on a double sided carbon tape.

Porous scaffolds prepared from freeze drying were quenched in liquid nitrogen before fracture. This allows the morphology of pores to be retained. Additionally surface topography of the porous scaffolds was prepared slicing the sections after they were quenched and then by transferring the scaffolds directly on to the specimen holder.

The elemental analysis and x-ray mapping for the samples were performed by energy dispersive X-ray analysis (*energy dispersive X-ray microanalysis*, EDX) from Typ NORAN VOYAGER

Transmission electron microscopy

TEM investigation of samples was done under TEM JEOL JEM 2010 with 200 KV operating voltage and LEO 912 EFTEM operating under 120 KV after ultramicrotomy and staining of the samples.

a) Ultramicrotomy

Ultramicrotomy of thin sections was performed under LEICA Ultra cut using diamond knife at room temperature. Ultrathin sections around 80-100 nm was obtained. Some of the parameters are listed in the table below.

Table 9: Parameters for ultramicrotomy

Parameter	Ultrathin sections	Semithin sections
Wedge size	0,1 mm×0,1 mm	5 mm × 5 mm
Knife	Diamond	Diamond
Knife angle	45o	45o
Free angle	5o	5o
Cutting sped	0,5 mm/s	0,5 mm/s
floating liquid	Distilled water	Distilled water
Cutting temperature	RT	RT
Section thickness	60-100 nm	300 nm
Grid	copper	copper

b) Staining

Ultrathin sections of PHB/HA and PHBHV/HA nanocomposite films were stained with RuO₄ vapours for 1-2 hours and then imaged

Samples for electrospinning was directly spun under copper grids and used for imaging and for nanoparticles, a very dilute suspension of nanoparticles with ethanol was prepared. A drop of this suspension was floated on carbon coated copper grid. This was allowed to dry in room temperature and then imaged.

Scanning force microscopy

Morphology of lamellar structure of spherulites was observed by TMAFM. Samples for AFM were prepared either by spin coating a dilute nanocomposite mixture in chloroform solution or by dip coating on mica substrates. Thin films were then floated on ultrapure water and the sections were then caught on different substrates for melt crystallizing. All the AFM observations were carried out under tapping mode by using Nanoscope III MultiMode AFM (Digital instruments). Both the height and phase images were measured simultaneously.

Typical values for the set point amplitude ratio (rsp is defined as the ratio of the cantilevers oscillating amplitude to its freely oscillating amplitude) were 0.7-0.9.

3.3.2 Thermal analysis (DSC)

Nonisothermal crystallization measurements

The crystallization behaviour of PHB/HA and PHBHV/HA nanocomposites was measured on a Metler Toledo DSC under a flowing nitrogen atmosphere. The sample weight was kept at approximately 8.5-10 mg for all the tests. For nonisothermal melt crystallization, the raw samples were quickly heated to 200°C at a heating rate of 100°C/min and maintained at 200°C for 3 min in the DSC cells to destroy any nuclei that might act as seed crystals. The samples were then cooled to 25°C at constant Φ values of 1.5, 5, 10, 20 & 30°C/min respectively. The exothermic crystallization peaks were recorded as a function of temperature.

3.3.3 Mechanical testing

Minimat tensile testing

Samples for tensile tests were prepared by solution casting as well as compression molding. Solution casted films had a thickness around 30-50 μm . Compression molded films had thickness around 200-300 μm . The samples were heated to 200°C under a pressure of 1-2 metric ton for 2 minutes and allowed to cool at RT. The speed of testing was 0.5 mm/min. Young's modulus was determined from the slope of the stress-strain curve in the elastic region (0-0.4% strain). The toughness was calculated by taking the area under the stress-strain curve. The ultimate strength was obtained from the maximum stress on the stress-strain curve. At least five replicates were tested to obtain an average value. All samples were tested after two days of conditioning at $23 \pm 2^\circ\text{C}$ and $50 \pm 5\%$ relative humidity (RH).

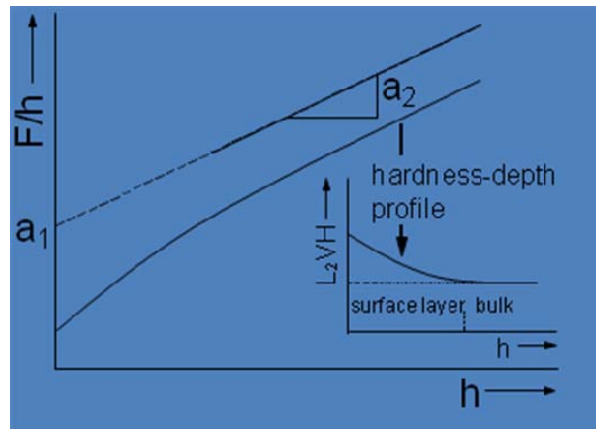
3.3.4 Microhardness

An instrumented ultramicro-indentation system (Microhardness tester Fischerscope[®] H100C) configured with a Berkovich diamond indenter was used to produce the indentations. Calibration of the indenter tip shape was carried out using PMMA plates at peak loads, P_{max} , ranging from 0.2 to 500 mN, to provide an accurate tip profile as a function of penetration depths. The indentation loads and the corresponding displacements were recorded continuously throughout a loading-unloading cycle, enabling measurement of the elastic modulus and hardness of the indented specimen. The indentation load increases with 20

increments up to $P_{max} = 1000$ mN for PHB/HA and PHBHV/HA films PHB films with a dwell at P_{max} of 20 seconds followed by unloading with 20 decrements. At least 20 indentations were made in a number of random locations on each film. The hardness and indentation modulus were determined from the instrument Knowledge of the indenter geometry and from the penetration depth, the contact area, A , could be determined from which the hardness, H , could be calculated.

$$H = \frac{P_{max}}{A} \quad (1)$$

Frequently composites films prepared by solution casting experiences different depth profile due to sample preparation which results in surface roughness. This leads to different indentation values which may leads to false analysis. In order to overcome surface rough by different depth profiles, Load independent Vickers hardness was analysed



L₂VH method

Figure 20: Schematic representation of load independent Vickers hardness (L₂VH) method

$$L_2VH = 0.03784 \cdot a_2 \quad (2)$$

Advantages of L₂VH method is the possibility of physically motivated interpretation of the parameters of a_1 and a_2 . It can also be correlated to young's modulus and yield stress. For polymers $L_2VH \approx 2.5 \sigma_y$ (Figure 20)

3.3.5 Micromechanical analysis

Samples for micromechanical deformations were performed as described below (Figure 21). Nanocomposite solution of very dilute concentration was either dip or spin coated on the glass slides for an average thickness of about 50-80 nm. Thin films thus obtained were

floated on distilled water. These thin films were then transferred to thin mica sheet. Films thus obtained were melt crystallized on a hot stage for about a minute. Samples were allowed to cool. Copper grids for measurements were heated to 800°C for 5 hours in controlled argon atmosphere, which results in phase change making the copper ductile. Ultrathin films on mica were again floated in distilled water and were caught on copper grids after applying a layer of polymer for good adhesion. Floated films were allowed to dry. Copper grid with a film was stretched at very low speed (0.1 mm/sec) in minimat tester, until a first appearance of craze. The whole setup was installed under optical microscopy control for recording the micromechanical events.

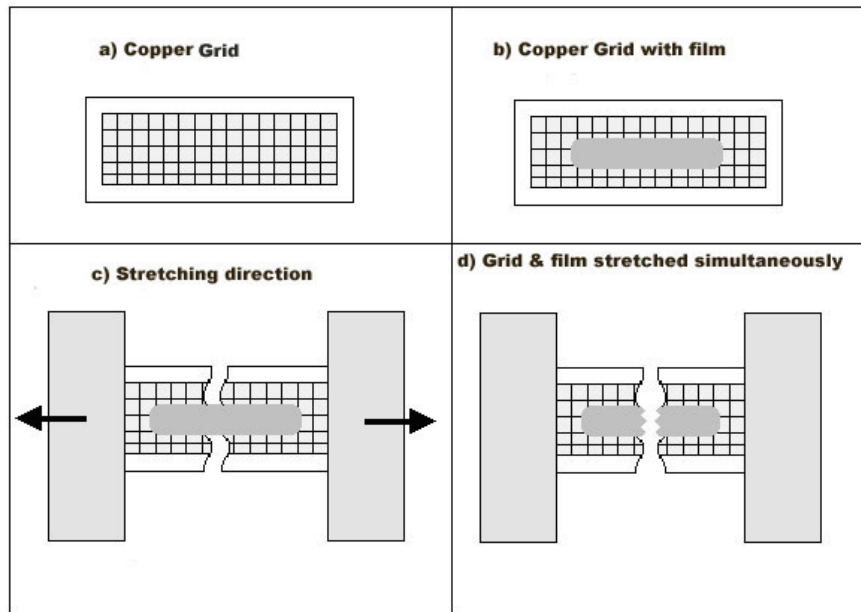


Figure 21: Micromechanical deformation experiments performed on copper grid (Krammers Method)

3.3.6 Surface characterization: Contact Angle

Contact angle was measured on pure and filled nanocomposite films using sessile drop method. Films used for measurement were prepared by dissolving 4 wt% (w/w) of composite in chloroform. Nanocomposite preparation is explained above. These respective solutions were then spin coated on a glass slide using Spin 150 (Wafer Spinner) equipped with software (rev.3.20). A constant rpm of 3500 and spinning time of 30 sec was maintained for all samples. This resulted in a uniform polymer surface suitable for contact angle analysis.

A drop of 30 ml freshly obtained bidistilled water was placed on each sample. The sessile drop analysis was performed with an OCA 20 Data Physics Instruments GmbH (Filderstadt, Germany) contact angle instrument, employing both digital imaging and drop shape analysis. The advancing contact angle was measured for 5 drops on a surface at temperature of 20 °C

and the average was calculated from the data. The apparent contact angle could be measured exactly (accuracy of the method was $\pm 0.2\%$), but as a result of surface roughness of the sample, a typical statistical error was in the range of 1-2%. Similarly, films casted on glass substrate were also used for analysis.

In this study, the surface tension or the free energy (γ) is calculated from contact angle (θ) using iterative method of Li & Neumann[155, 156] based on the results of Good & Girifalco.[157]

3.3.7 Cell culture tests

Cell culture using MG 63

The MG63 cells were cultured in Dulbecco's modified Eagle's medium (DMEM; Sigma) supplemented with 10% fetal calf serum (FCS; PromoCell, Heidelberg, Germany), 1% pen/strep/fungizone (PromoCell) and 1% sodium pyruvate (Biochrom AG, Berlin, Germany), at 37°C in a humidified atmosphere of 5% CO₂ in air. The cells were regularly subcultured. At confluence, the cell monolayer was washed once with PBS and incubated with 0.05% trypsin–EDTA solution (Biochrom AG) for 3–5 min at 37°C to detach the cells. The activity of trypsin was then inhibited by adding culture medium containing serum. This cell suspension was centrifuged for 5 min at 1000 rpm and the supernatant was aspirated.

The cell pellet was resuspended in fresh culture medium and the cell number was counted using a Neubauer chamber (Brand, Wertheim, Germany).

The MG63 cells were seeded at a density of 10^4 cells/ml/well in DMEM containing 10% FCS on plain tissue culture polystyrene (TCP) and on the films in 24-well plates. The medium was changed three times a week. The controls and films were evaluated at days 1, 3 & 7 days for cell viability/proliferation, alkaline phosphatase (ALP) activity, and cell morphologies visualized by fluorescence microscopy.

Cell morphology

Cell morphologies were observed after 1, 3 and 7 days during the experiments. Since the membranes used in this study were not transparent so, the cells were stained with a fluorescent dye called FDA (Fluorescein diacetate) and observed under fluorescence microscope

Cell proliferation measured using LDH assay

In order to measure cell proliferation, the LDH assay as a quantitative colorimetric method was carried out after 1, 3 and 7 days of culture using an LDH Assay Kit (WST-8) (BioCat, Heidelberg, Germany).

Lactate dehydrogenase (LDH) is a cytoplasmic enzyme that is present in all viable cell types. The LDH assay normally serves as a measure of film integrity. LDH released into the medium is used to evaluate cell or tissue damage (Figure 24). The LDH assay is normally used to assess cytotoxicity by measuring LDH concentrations in cell supernatants. However, in the present study, a modified version of the assay that measures the LDH in cell lysates was used in order to provide an estimate of viable cell numbers.

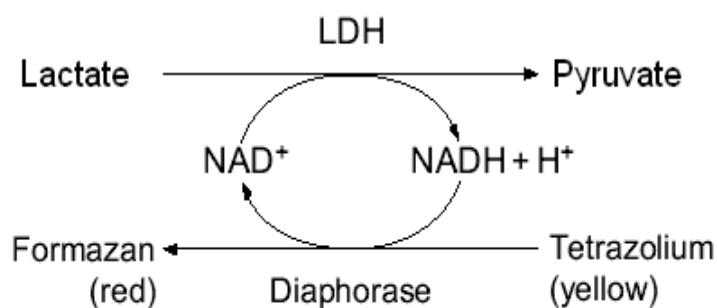


Figure 22: Principle of LDH assay [LDH cytotoxicity detection kit manual; Takara Bio Inc., Shiga, Japan

The LDH assay is non-radioactive and is based on the reduction of the tetrazolium salt INT formazan through an NADH-coupled enzymatic reaction (Figure 22). Diaphorase is a dehydrogenase enzyme that catalyzes the dehydrogenation of the coenzyme NADH. The hydrogen proton liberated then combines with the tetrazolium salt to form a formazan salt. The formazan thus formed is a water-soluble, visible dye. It is therefore detectable at a wavelength of 492 nm by using a plate reader.

The medium in culture wells was removed and the cell layer was washed twice with PBS. Since LDH cannot be detected extracellularly unless cell damage has occurred, living cells were lysed for 30 min at 37°C with 100 μ l/well lysis-solution (0.5 % Triton X-100; Sigma). During the incubation period, the culture plate was gently shaken by hand every 5 min. Ten-microliter aliquots of the cell lysis solution were transferred to individual wells in a 96-well plate. The 0.5 % Triton X-100 solution was used as a blank reference. The LDH reaction mix

comprising 200 µl substrate-mix (WST-8) containing tetrazolium salt in 10 ml LDH assay buffer was prepared in accordance with the manufacturer's instructions. One hundred microliters of the LDH reaction mix was added to each aliquot of the cell lysis solution, mixed, and then incubated in the dark for 30 min at room temperature. The absorbance of the solution was measured at 492 nm using a plate reader (FLUOstar, Optima, Germany). For statistics, quadruplicates of samples were taken for cell proliferation experiment. Mean values and standard deviations were calculated accordingly.

Alkaline phosphatase (ALP) activity

ALP activity is a representative marker for the early stage of osteoblastic differentiation[158]. ALP is expressed at a basal level in MG63 cells cultivated in standard medium. After 1, 3 and 7 days of incubation, ALP activity was determined in cell lysates that were obtained by treatment of cultures with 0.5 % Triton X-100 in distilled water. In this experiment, a portion of the cell lysates prepared for the LDH assay was used. The ALP activity was measured colorimetrically using p-nitrophenyl phosphate (pNPP; Roth, Karlsruhe, Germany) as a substrate. The ALP expressed by the cells hydrolyzes the substrate to p-nitrophenol (p-NP) and an inorganic phosphate. Under alkaline conditions, the p-NP is converted to a yellow-colored p-nitrophenylene anion.[159]

Hydrolysis was performed by incubating 50 µl of the cell lysate from each well with 100 µl of 1.0 mg/ml pNPP solution (pH 10.2) in a 96-well plate for 1.5 h at 37°C[160]. The 1.0 mg/ml pNPP solution was prepared in 0.5 M AMP (2-Amino-2-methyl-1-propanol; Applichem) buffer, pH 10.3. The absorbance of the p-NP released in the reaction solution was read at 405 nm using a plate reader. The ALP-specific activity in the cells was normalized for the total amount of cell lysate. For statistics, quadruplicates of samples were taken for cell proliferation experiment. Mean values and standard deviations were calculated accordingly.

Cell culture using human osteoblasts

An approved method for isolation of primary human osteoblast cells from trabecular bone from the femoral head of patients undergoing hip arthroplasty was performed using a modified protocol. Under sterile conditions, trabecular bone chips were dissected from the femoral head, placed in vials containing calcium-free DMEM/F12K medium (Specialty Media, Lavallete, USA), and minced into small bone chips. The bone chips were then washed several times in fresh medium. To remove the fibrous matrix surrounding the bone chips, the bone chips were placed in a collagenase P enzyme media (Sigma, St.Louis, MO,

USA) under a closed environment, while stirring constantly at 37°C in 5% CO₂ for 3 hrs. Digested chips were then washed repeatedly in sterile sodium chloride solution, vortexed between washes at a low constant speed and placed in a 150mm cell culture flask (COSTAR, Cambridge, MA, USA) containing calcium-free DMEM/F12 medium, supplemented with 10% FBS, 2 mm l-glutamine, 50 mg/ml ascorbate and 50 mg/ml penicillin/streptomycin at 37°C in 5% CO₂. Within 2 weeks, cell migration from the bone chips occurred and the media was then supplemented with 110mm CaCl₂. Cells consistently exhibited osteoblast morphology, osteocalcin and alkaline phosphatase production.

Immunohistology of cells

The collagenous matrix synthesized by primary osteoblast cells cultured on PHB/HA was determined by immunocytochemistry as previously described. After 10 days of culture, the cells were washed in PBS, fixed in cold methanol at -20°C, and stained immunocytochemically for Type I collagen. Collagen produced was revealed by immunofluorescence and the immunocytochemical staining was visualized by fluorescence microscopy using a combination of excitation filter (350-nm wavelength) and barrier filter (530-nm wavelength).

4 Results and Discussion

4.1 Morphology of nanoparticles

4.1.1 Morphology of nanoparticles from chemical precipitation process

Morphology of HA synthesized from precipitation process yielded micron sized particles of the order 5-10 μm (Figure 23). The Ca/P ratios of the synthesized samples were found to be 1.65. Chemical analysis of the sintered samples for Mg and Na revealed 0.033% and 0.09% respectively. Figure 24 depicts the FTIR spectra of HA powders heated at 80°C, 650°C and 900°C respectively. The spectrum shows the characteristic peaks of the adsorbed water, hydroxyl, phosphate and carbonate species. The broad peak with a shoulder around 3100 cm^{-1} to 3250 cm^{-1} for the sample at 80°C corresponds to the adsorbed water. The spectrum clearly indicates a peak at 1640 cm^{-1} (bending mode H_2O) which is attributed with adsorbed water. The absorption bands at 1460 cm^{-1} and 875 cm^{-1} suggest the presence of CO_3^{2-} , which is supposed to have come from SBF and atmosphere during precipitation process.

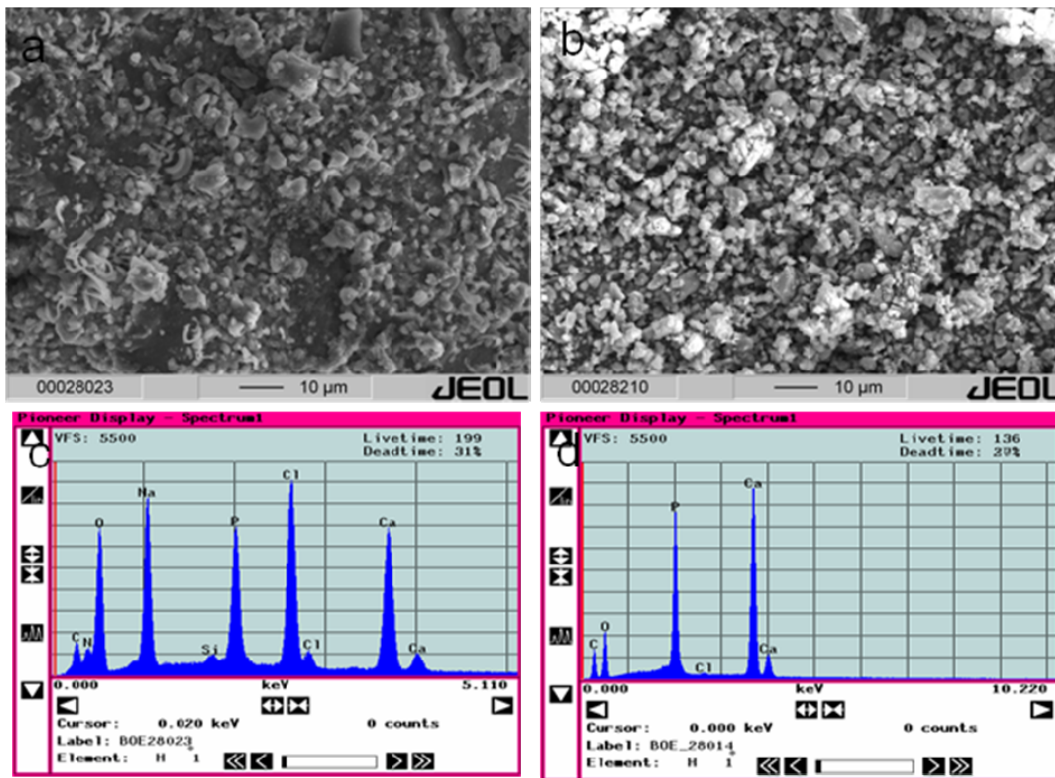


Figure 23: Morphology of HA fillers immersed in simulated body fluid. a) SEM micrograph of HA particles synthesized via precipitation method and image corresponds to as synthesized material, b) SEM micrograph of HA filler sintered at 900°C and c & d are corresponding EDX spectra of as synthesized HA and sintered HA (900°C)

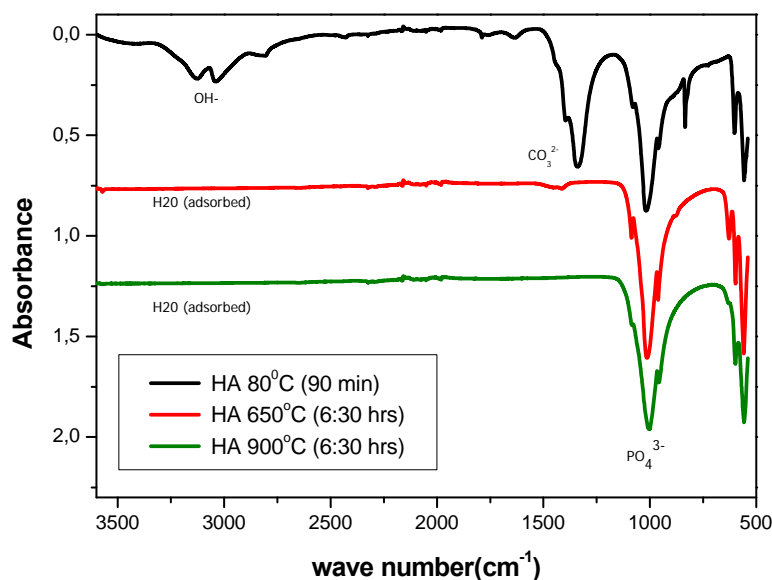


Figure 24: FTIR spectra of HA sintered at 80°C, 650°C and 900°C

The total intensity of these bands gets decreased for the samples calcined at 650°C and 900°C. This confirms the elimination of CO_3^{2-} ion at higher temperatures. Also, bands at 630 cm^{-1} assigned to OH^- ion was not clearly visible for the sample heated at 80°C. The absorption bands at 1040, 1093 and 962 and 571 cm^{-1} detected in the spectra are attributed to PO_4^{2-} ion.

SEM micrographs of HA in Figure 25 shows the morphologies of HA before and after soaking in SBF. After one hour of soaking, precipitated particles could be observed on HA surface. These particles were similar to that of rod like numerous tiny granular apatite particles which grew on the surface (Figure. 25b). Such crystals would be expected to grow and form a layer of calcium phosphate (Ca-P) on the surface that could later crystallize to a bone like apatite crystals. The nucleation of these precipitated crystals prefer to occur in pores rather than on smooth surfaces, where the size of the precipitates is, obviously, much larger than that on the smooth part of the surfaces. The quantity and size of these precipitates increases as the soaking time increases. With further increase in the soaking time, there is no significant change in the surface morphology, and small crystallites can be observed.

EDS analysis of the HA precipitated apatite layer had the peaks of calcium, phosphorus, sodium, chlorine, carbon and oxygen (Figure 26). The presence of Na and Cl in the EDS spectra is attributed to residual element from the SBF solution. The thickness of apatite crystals formed on the HA surface was examined by SEM. It was found that there was no

uniform layer of apatite developed on the HA, instead crystals in the form of rods sprouted from the surface randomly. Formation of apatite layer is also strongly attributed to the time of soaking. Larger soaking time results in uniform deposition. As in the case observed above, the soaking time was only limited to one day.

By morphological analysis it can be confirmed that the extra structure on HA surface is by apatite layer and its existence is also confirmed by the presence of carbon in EDX analysis which also implies that the HA promotes the carbonate apatite layer formation.

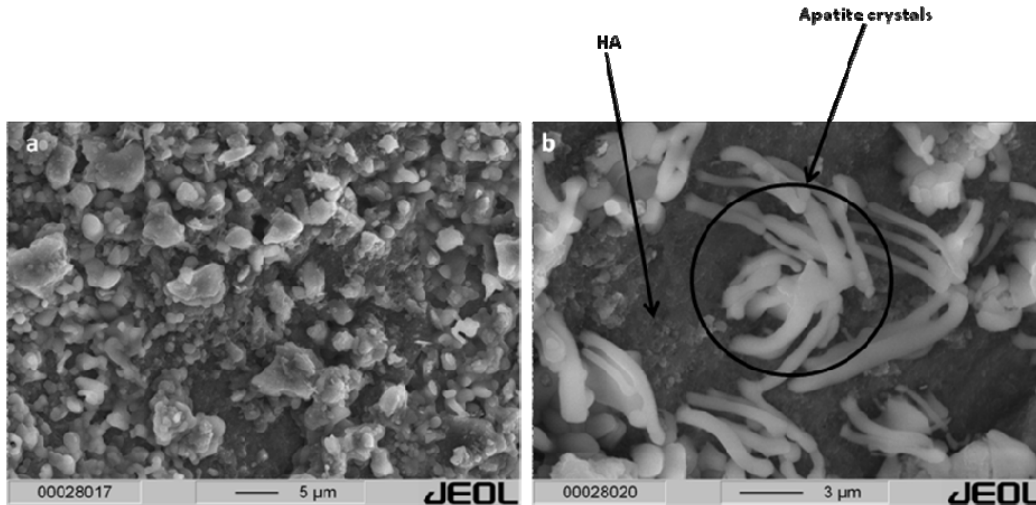


Figure 25: SEM micrograph of Hydroxyapatite powder. a) Green powder of HA & b) After soaking in SBF solution for 2 days some areas are already covered by inorganic crystals of apatite.

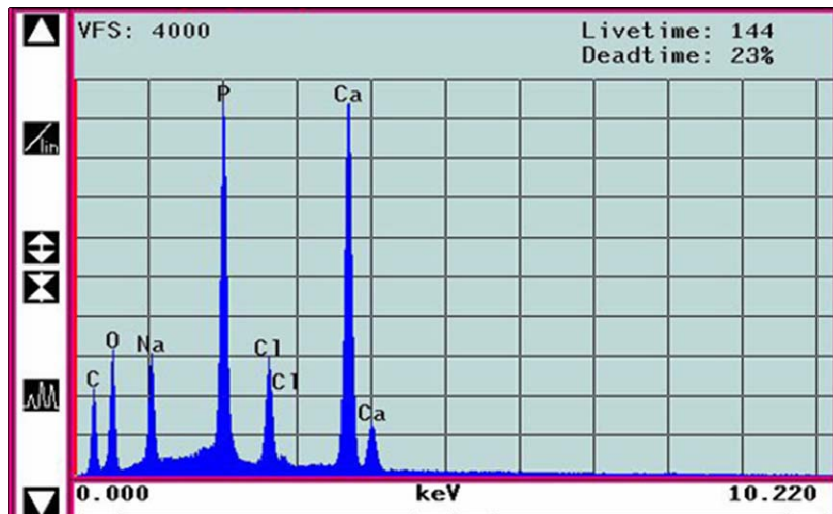


Figure 26: EDX spectra of HA after immersion in SBF (1 day)

4.1.2 Morphology of nanoparticles from Wet precipitation process

Synthesis of hydroxyapatite prepared from wet chemical method resulted in nano sized HA particles which were needle shaped. These nano rods had an average length of about 130 nm and a thickness of about 24 nm. Eventually the calculated aspect ratio account to 5.4. Nano fillers with high aspect ratio has tremendous influence on mechanical properties as well as show significant improvement in osteoblast cell function compared to that of low aspect ratio particles [161]. It is also observed that the stoichiometric parameters also influence to larger extent on the final morphology of the nanofillers formed. With the slight change in these parameters, the morphology can change from needles to spherical or even to whiskers or platelets.

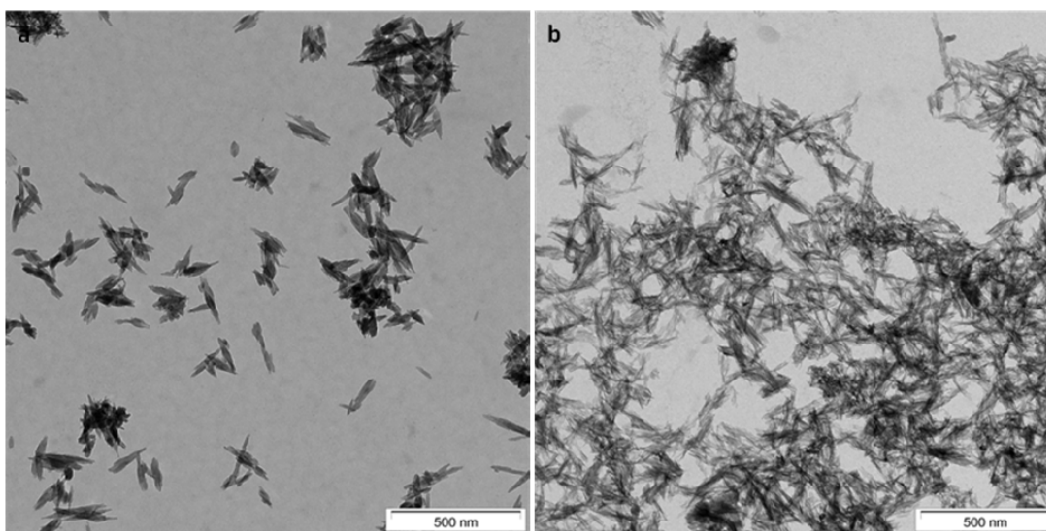


Figure 27: TEM micrographs of HA nano particles obtained by wet chemical method. a) $\text{Ca}(\text{OH})_2$ and H_3PO_4 precursor solution of pH 10.5 and b) $\text{Ca}(\text{OH})_2$ and H_3PO_4 precursor solution of pH 12.

In the present investigation, nanoparticles are synthesized with all the synthetic parameters kept constant except pH and ageing time. Experimental observations indicated that change in pH has pronounced influence on the structure of the crystals produced. Figure 27 shows TEM micrographs of the morphology of nanoparticles produced by varying pH. The pH of the starting solutions can affect chemical precipitation by altering the solubility of the system thereby by effecting crystal growth and powder agglomeration. When the pH was around 10.5, the preferred growth resulted in rod like morphology with the larger average particle dimensions. There was distinct structures formed, which resembles like a rod. The precipitate produced with $\text{Ca}(\text{OH})_2$ and H_3PO_4 precursor solutions of matching pH (10.5) gave rise to stoichiometric HAP powders that was sintered to 98.5% theoretical density. In contrast, the samples prepared by $\text{Ca}(\text{OH})_2$ and H_3PO_4 precursor solutions of pH (12) resulted in undefined morphology where the length and width of the nanoparticles were somewhat scattered. Also

by TEM images, it can be noticed that the hydroxyapatite formed may not be stoichiometric. This was also noticed that the samples when subjected to sintering at 1200°C, nanoparticles obtained from 10.5 pH precursor solutions were stable and those of pH 12, precursor solution underwent decomposition during sintering.

We have found that aging was critical in obtaining well-crystallized HAP particles with uniform morphologies. Occluded impurities are removed and crystal strain is reduced in the aging process, whereas grains with no uniform morphologies redissolve and are re-crystallized into more ordered forms. Longer aging times also ensure that the reagents are fully reacted and precipitated. It was noted that an aging period of 50 hrs led to small crystallite sizes (L-130 nm and W-24 nm) as verified by transmission electron microscopy (TEM). Also, this sample was sintered easily without phase decomposition. In contrast, the sample that was not subjected to aging underwent severe decomposition upon sintering, indicating that the as-precipitated phase was not thermally stable due to its poor compositional uniformity.

4.2 Dispersion

4.2.1 Dispersion of nanoparticles in polymer matrix

Nanoparticles in solutions present typical colloidal systems consisting of a continuous phase, which is a dispersed medium (solvent) and a dispersed phase (nanoparticles). These solutions have relatively low stability which is attributed to large particle size with perceptible free surface energy. Nevertheless, nanoparticle dispersion in polymer matrix in general is thought to be very difficult. This is because of the reason that, there exist Van Der Waal's forces of attraction between the particles. These forces play a vital role in particle agglomeration. Two different nanoparticles varying in shape and size were dispersed in polymer matrix using ultrasonication. Crucial factors determining stability of dispersion depends on many factors like temperature, type of solvent, power applied for dispersions, viscosity of the medium and amount of nanoparticles (wt%) dispersed.

An optimum condition for uniformly dispersed nanoparticles in polymer matrix depends on the interplay between these parameters. Nanoparticle prior to mixing in matrix polymer was dispersed in suitable solvent. OSTIM nanoparticles as mentioned before are in the form of suspension in water. For OSTIM nanoparticles, ethanol was efficient than with chloroform. Using chloroform as solvent, it was not possible to disperse even at higher ultrasonic amplitudes. Nanoparticles rather got clumped and were adhered to the wall of glass bottle. To optimize the dispersion, the sonication time was varied from 0 to 45 mins at 21% and 34%

amplitude. The best result was obtained using a total mixing time of 30 min and for 21% amplitude. Further increment in dispersion time increased the temperature of the polymer solution and in turn increased the viscosity. At higher viscosities the movement of the chains is restricted and this acted as a barrier for nanoparticle movement i.e the nanoparticles should overcome the Van Der Waal's forces to separate itself and then it should overcome the movement of restricted chains. Figure 28 shows the dependence of temperature on sonication time with respect to two different ultrasonic amplitudes. Stability of dispersions was manually observed for their optical clarity. OSTIM nanoparticles which were in the range of 18-30 nm in thickness were stable in dispersions for period of 1 week and also the optical clarity was good for 5-10 wt%, whereas HA nanospheres with average diameter of about 150-200 nm were not stable and the clarity was not achieved. Due to gravity, these larger particles tend to settle down within few hours.

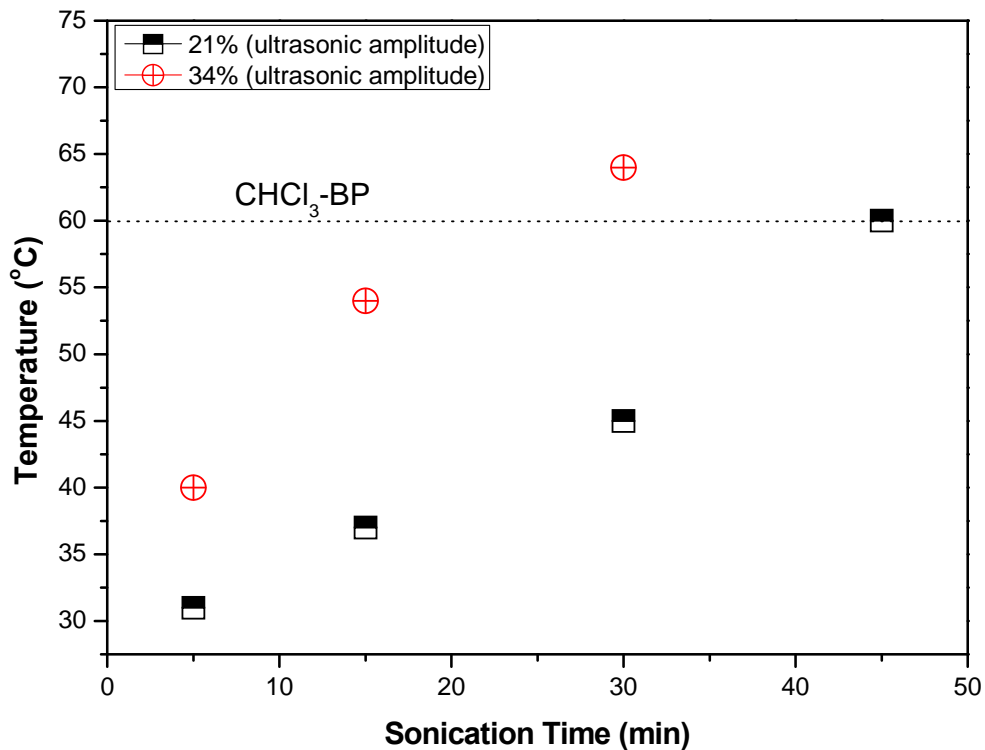


Figure 28: Effect of sonication time (min) on temperature, when chloroform is used as a solvent

4.2.2 Effect of Dispersion on filler content

As we know for nanocomposites, the ultimate mechanical properties are influenced by the morphology it develops while fabricating. Efficiency of nanoparticles dispersion was observed by morphology developed on the nanocomposites films by using SEM and TEM.

Micrographs of PHB/HA nanocomposites with varying filler content and shape are shown in Figure 29 where white color indicates HA nanoparticles in PHB matrix. It is evident that the

nanoparticles are uniformly dispersed in polymer matrix irrespective of filler loading. Figure 29 a & b shows the morphology of nanocomposites with 10wt% and 20wt% nanoneedles. It can be observed that with decrease in nanoparticle size, large ceramic content is accommodated per unit volume. Also there is least possible agglomeration observed in nanoneedles. Whereas for nanospherical particles, which are bigger than nanoneedles, particles seems to be very well dispersed. Size effect of nanoparticles plays an important role for uniform dispersion.

Larger particle size improves dispersion. This could be observed in Figure 29 c & d with same filler loading but with larger filler particles. The reason behind this is smaller size has more Van Der Waal forces between the particles compared to larger particles and that decrease the dispersion capability. The particle–particle interaction is high for smaller size and the applied ultrasonic energy and time of dispersion are unable to separate all particle.

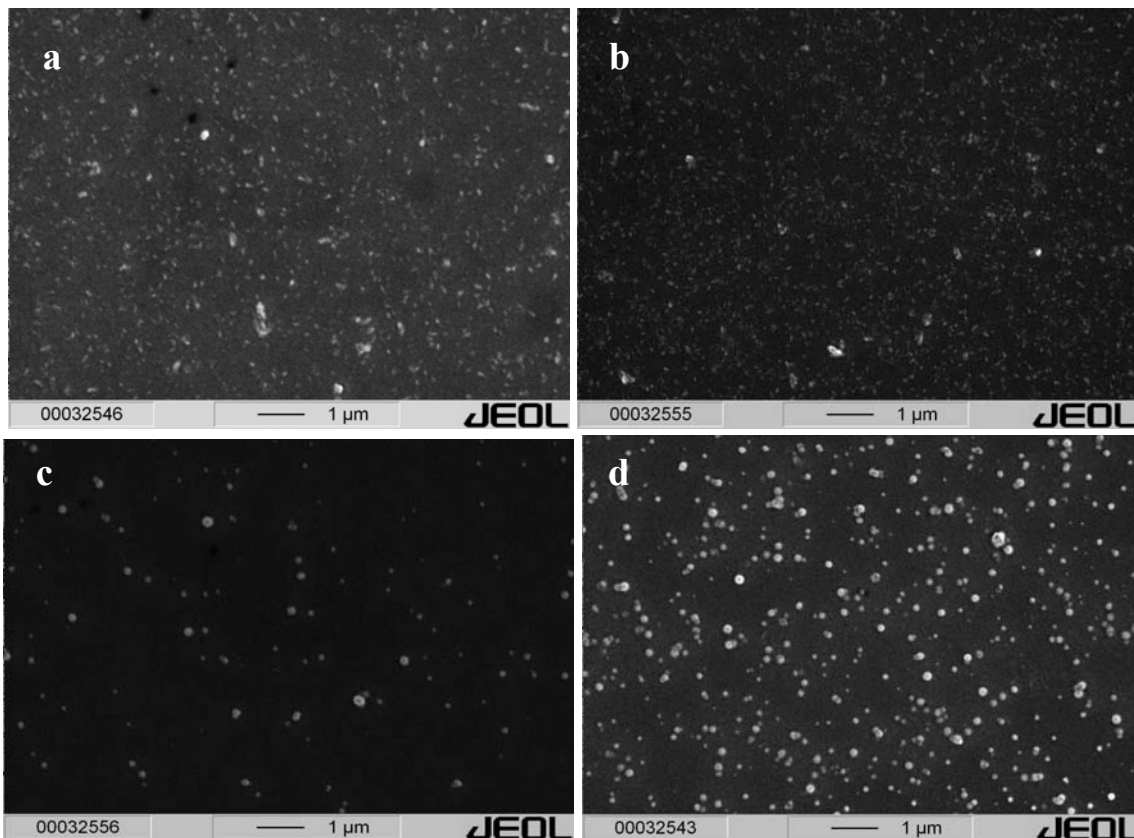


Figure 29: Effect of nanoparticle dispersion in PHB matrix. Sonicated using a tapered tip sonication probe and the amplitude of sonication was kept constant at 21% amplitude. SEM micrographs of nanocomposites, where a & b are PHB/HA rods at 10 and 20 wt% filler loading, c & d are PHB/HA spheres at 10 and 20 wt% filler loading.

Here we can observe very good dispersion of the particles but with the number of agglomerated particles seems to be increased. This increasing in filler loading creates nonuniformity that is clearly observed in Figure 30, in which the size of agglomerates of HA

is in the range from 3-6 μm .

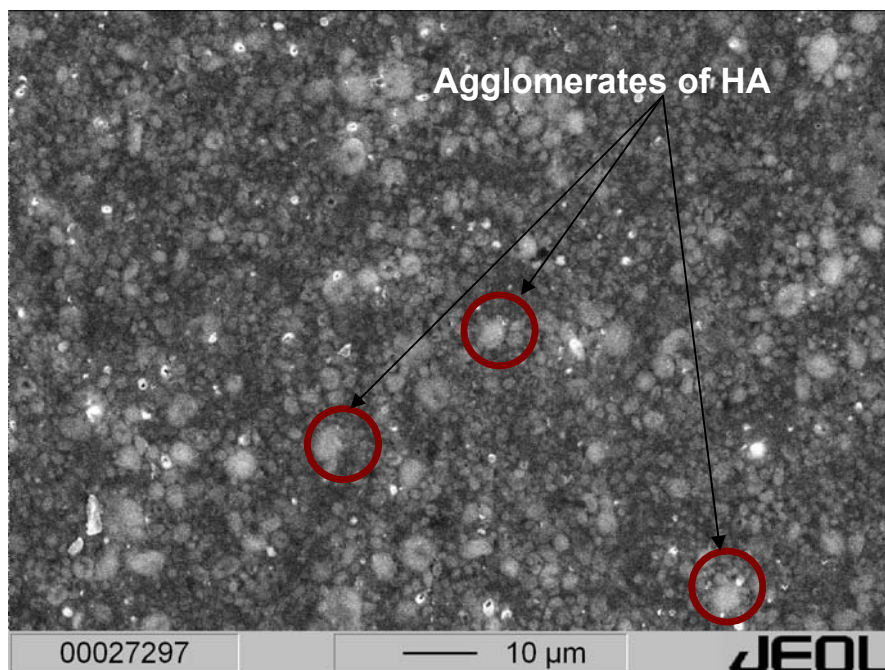


Figure 30: Nanoparticle agglomeration at higher wt% filler loading

4.3 Morphology of nanocomposites

Lamellar features in thin melt films of pure PHB and PHB/HA nanocomposites were characterised using AFM. It was observed that both flat on and edge on lamellae were observed in PHB obtained from different source. PHB obtained from Methanomer (a purest form) had flat on lamellae when melt crystallized at 90°C. Whereas PHB obtained from Biomer and Sigma showed flat on lamellae at all temperatures. The lamellar periodicity was also measured for PHB lamellae at different temperatures. At 60°C, PHB lamellae were in the range of 5-8 nm, whereas at 110°C, they have 8-11 nm and the value tended to increase with increase in crystallization temperature. This was also confirmed by SAXS measurements, where the values of lamellar periodicities of PHB thin melt films were almost identical with the long period or lamellar thickness of melt crystallized films. Another interesting feature observed in AFM images of PHB and PHB/HA nanocomposites are arrangement of crystalline lamellae. Both had similar crystalline lamellar arrangement. But with needle filled systems, some fillers seemed to be excluded from the lamellae which had similar thickness as that of lamellar thickness.

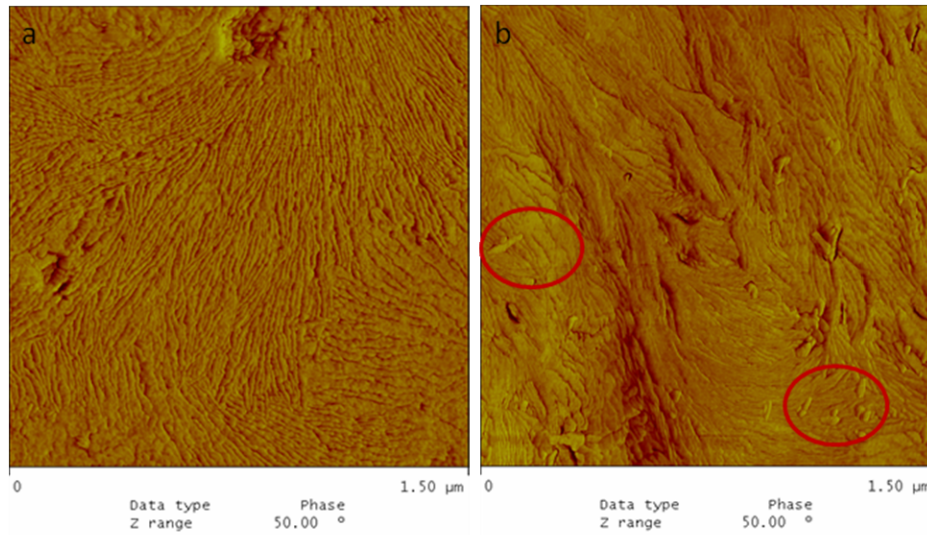


Figure 32: Lamellar morphology of PHB and PHB/HA nanocomposite dipcoated on a mica substrate. a) Pure PHB Thin film and b) PHB/HA(needle) thin film

4.3.1 Defects in spherulites

When PHB is crystallized from the melt, spherulites usually contain cracks, and these cracks are either radial or circumferential. Figure 33 shows two types of defects which usually occur in PHB. Circumferential defects are those of interspherulitic defects which arise in the boundaries of spherulites. These circumferential defects appear principally in the film crystallized at higher temperatures, after they had been cooled to room temperature. This suggested that the stress causing this form of cracking may be due to the spherulites possessing different radial and circumferential thermal expansion coefficients which generate large internal stresses. Another type of defect that is commonly observed in PHB is intraspherulitic defects which are present inside the spherulite. They may appear in between the lamellae and run radially along the diameter of the spherulites.

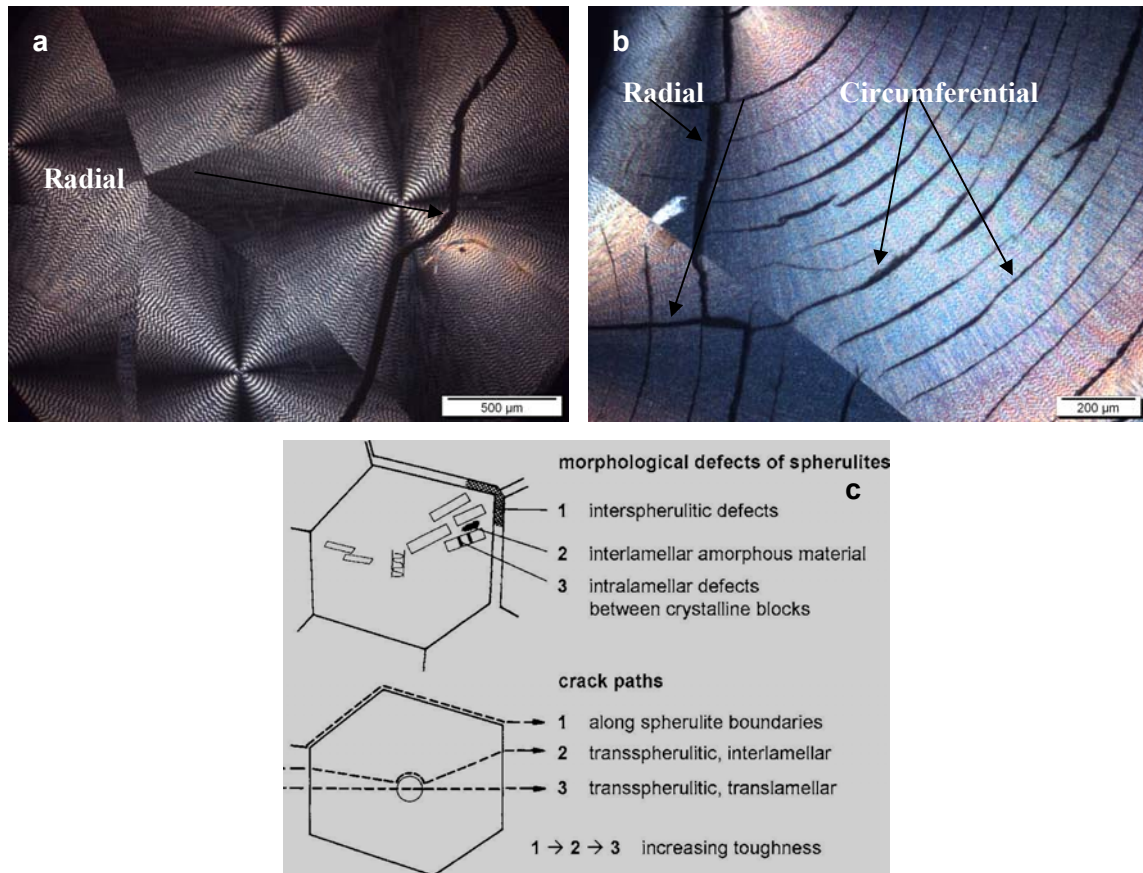


Figure 33: Optical micrographs of Pure PHB demonstrating inter and intraspherulitic defect on prestrained samples which were crystallized at 120°C a) Radial crack in pure PHB b) both radial and circumferential cracks in pure PHB and c) Schematic model for intraspherulitic and interspherulitic defect.

According to Barham and Keller, radial cracks occur in spherulites crystallized at room temperature or more specifically in thin films, which are crystallized below 120°C. But the cracking is somewhat related to temperature regimes which they call as regimes II growth (above 130°C) and regime III growth (below 130°C). Radial cracks according to them occurred usually at regime III that is (spherulites crystallized below 130°C). But in our samples, we observed radial cracks even at higher temperatures. Optical micrographs in Figure 33a shows both radial and circumferential cracks in unstrained samples. Radial crack can be observed in sample 33a which was crystallized at 90°C and both radial and circumferential cracks was observed in samples crystallized at 130°C 33b for pure PHB. The growth regimes as suggested by Barham and Keller et al. are based on relative rates of formation and subsequent spreading of secondary nuclei across the growth face. Thus in regime II the nucleation rate has increased relative to the spreading rate so that several separated nucleated patches are simultaneously spreading across the growth front. The number of such patches increases as crystallization temperature is reduced. Eventually

beyond a certain supercooling, nucleation will be so frequent that the separation between adjacent nuclei will approach the order of the lattice spacing. At this stage regime III takes over. In our samples since the temperature of transition between regime II and regime III are very close, we cannot differentiate between them clearly. Nevertheless, at very low crystallization temperatures of 25°C and 50°C, we could not observe any cracks in unstrained samples suggesting that cracks develop only in bigger sized spherulites. Cracks were even not found in composites filled with HA because of heterogeneous nucleation induced by nanoparticles, which caused the reduction in size of spherulites drastically.

Another reason for these types of cracks to occur was due to surfaces on which spherulites were grown. When stiff surfaces like glass are used, the melt just in front of growing spherulites may be severely constrained by the presence of spherulites, so that a considerable negative pressure may build up. It is possible that the resulting stress on the spherulite may be relieved by it detaching itself from the surface at which growth is occurring, thus partially accommodating the volume change on crystallization. The fact that there is considerable stress in the samples caused by the volume reduction on crystallization can often be seen by the front of bubbles near the growth front. SEM micrographs show spherulite growth front just before features begin to appear (Figure 34). At first, a large number of bubbles are formed. As the growth front continues the smaller bubbles disappear into larger ones, which are later transformed into holes (Figure 34 B). Crack propagation originates from these holes (Figure 34 C). On cooling fully grown spherulites, large cracks are seen to grow circumferentially around and radially across the spherulites (Figure 34 D).

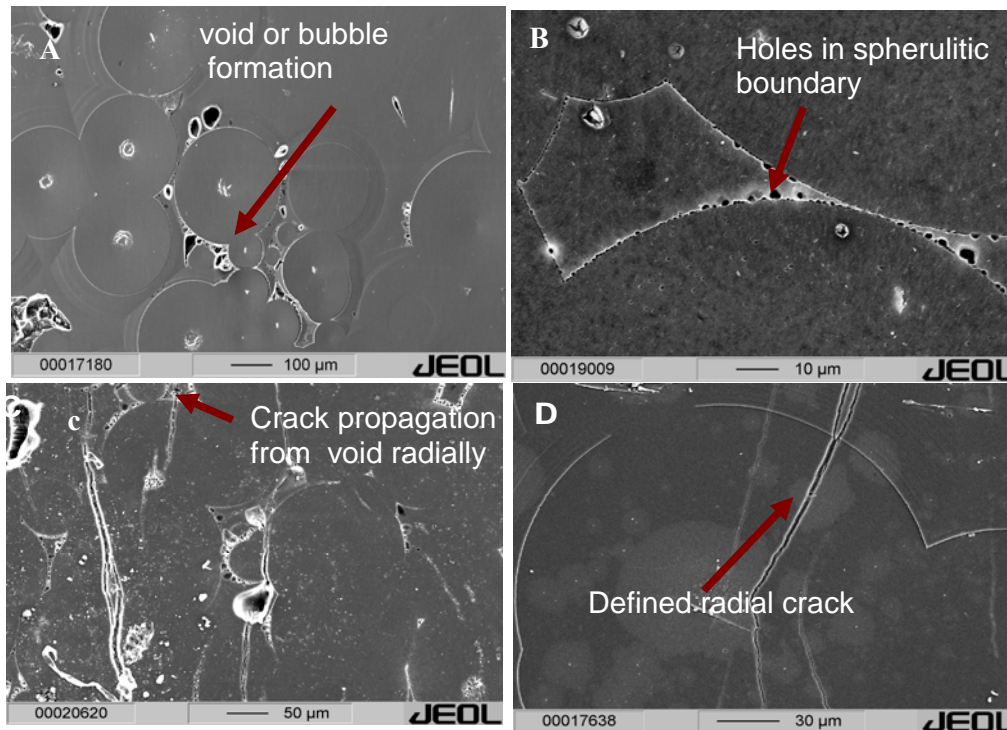


Figure 34: Shows the appearance of interspherulitic defect due to surface effects. A) Spherulite growth front stressed and resulting in voids, b) voids manipulating into holes, c) crack propagation from the hole into the spherulite in radial direction, d) Defined radial crack which passed through the spherulite.

4.3.2 Deformation in PHB spherulites

Two distinct kinds of deformations were observed in spherulites. One in which deformation starts within the spherulites (I) and the other where deformation starts in between the spherulites (II). In number of samples, the yielding first progressed in those boundaries at which spherulites were perpendicular to draw direction. However, when yield zone meets along a boundary which is parallel, that is radial region perpendicular to draw direction, it spreads over the whole spherulite which pulls out inhomogenously over that region. Spherulites which were far from the yield zone, just showed multiple tiny cracks around their borders. In case of deformation in the spherulites, which deformed along the regions where the radii are perpendicular to draw direction. However, due to brittle fracture, it was not possible to observe any finer details of spherulite shape during deformation.

PHB spherulites possess very high degree of crystallinity and when crystallized at higher temperature, they possess very large spherulites due to secondary crystallization which results in the defects mentioned above. When PHB is subjected to external stress, they damage in a particular way and the thermal history and preformed defects acts as stress concentration points for the deformation to take place, which caused ultimate failure in the sample.

In samples which were crystallized at higher temperatures, fracture propagated in the boundaries of spherulites due the circumferential defects present earlier (Figure 35A). Samples which were quenched in liquid nitrogen had no spherulitic superstructures (Figure 35B). Small spherulites were still observed. Deformation pattern in this sample progressed with multiple fibrillation and also minute craze like structure which were observed around the deformation zone. Even though it was impossible to control these defects, but was reduced to a larger extent by rapidly quenching the melt crystallized samples.

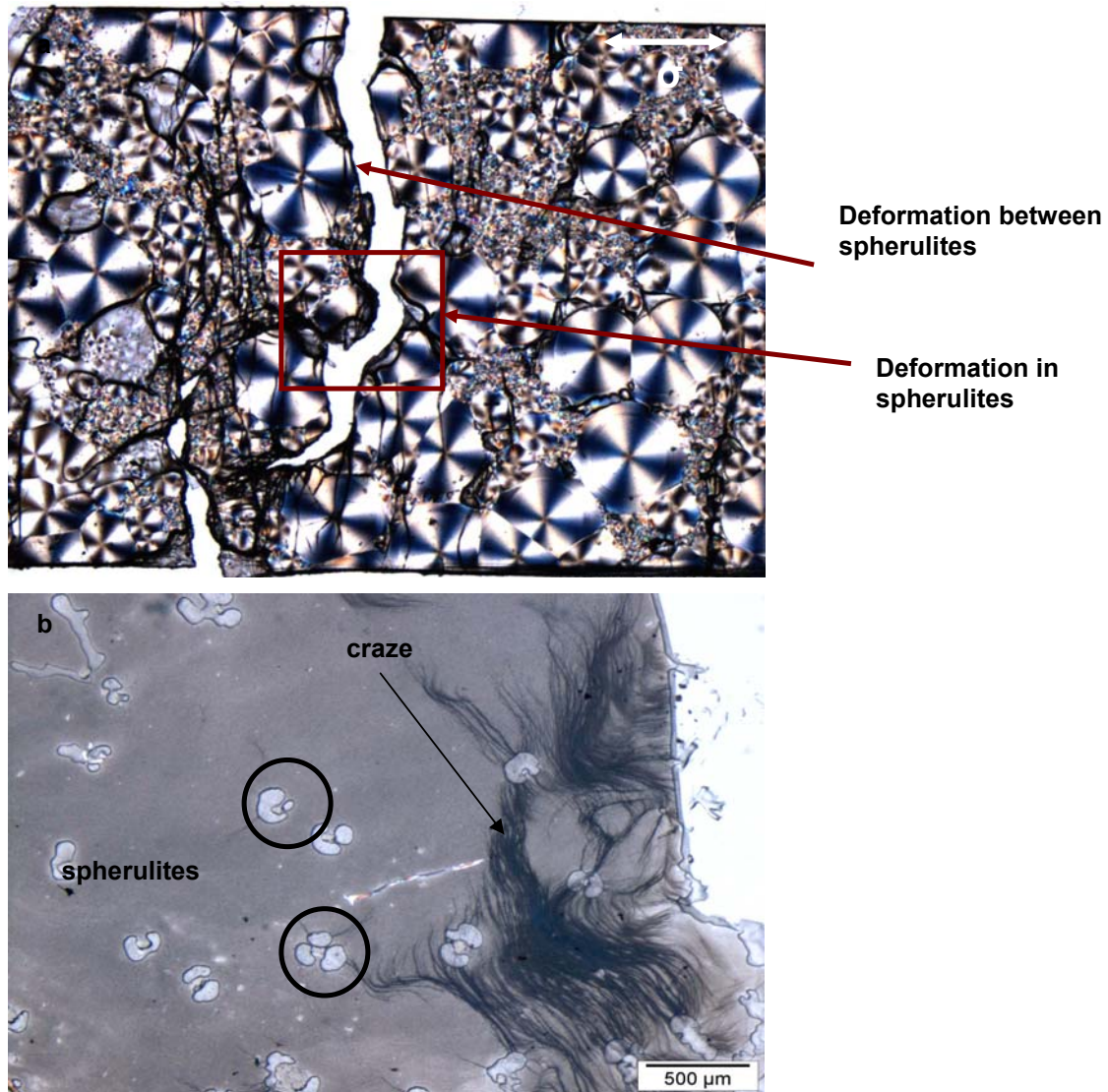


Figure 35: Mode of fracture in PHB. A) Pure PHB crystallized from melt and B) Pure PHB crystallized and quenched in liquid nitrogen.

4.3.3 Morphology of Spherulites

Morphology and growth rate of spherulites of PHB were evaluated with polarized optical microscopy (POM). It is well known that the crystallization of polymer thin film from a melt is controlled by the arrangement of crystalline entities (chain folding) and diffusion of chains from the melt to the crystal front. The actual crystallization morphology and structure of polymer depend on the crystallization temperature of thin melt film with a certain thickness. The morphology of PHB thin melt film with the same thickness crystallized at different temperatures was observed by POM. Interestingly, PHB crystallized at different temperatures had different spherulite morphology. This is because, spherulites were nucleated at different times so that they were different in size when impinging on one another and their boundaries were hyperbolas. Compared to other thermoplastics, the nucleation density of PHB is relatively low mostly because of its natural origin. This leads to very large spherulitic super structures with the diameter ranging from micrometers to millimetres. Figure 36 demonstrates spherulites crystallized at different temperatures. Under the same field, the number of spherulites increases with decreasing the crystallization temperature, due to increase in nucleation density. Consequently, smaller spherulites are observed at lower crystallization temperatures. For example, the diameter of PHB spherulites decreased from 1.5 mm at 90°C to 20 µm at 25°C. A Maltese-cross pattern was clearly observed for PHB samples, where the arms of cross parallel to the directions of polarizer and analyser. Due to the twisting of lamellar crystals, where the crystallographic a axis is radial, while b and c axes rotating about it [162]. PHB spherulites exhibited a banded texture, which shows alternative bright and dark rings under POM. When PHB isothermally crystallized at 25°C, size of the spherulites decreased and number of spherulites increased. At 90°C, banded structure of spherulites could be observed as in Figure 36 (b). However the band spacing decreased markedly, and the surface morphology of the spherulites was obviously different from that crystallized at 110°C and 130°C (Figure 36 (c & d)). For example band spacing measured at 90°C was 39 µm and it gradually reduced to 18 µm at 110°C and 10 µm at 130°C. In PHB (biomer), the bandspacing was 29 µm at 90°C, 52 µm at 110°C and 44 µm at 130°C. This large discrepancy in band spacing is because of the thin films which were used for POM analysis. In thin films, the twist periods are of the same order of magnitude as the sample thickness. Conceivably, the top and bottom surface constraints flatten out the lamellar units in the thin films. When the isothermal crystallization temperature was up to 130°C, PHB formed typical radial growth spherulites (non banded spherulites).

The mechanism of banded spherulites has been explained by many different theories. Keith and Padden attributed banding in polymer spherulites to the twisting of lamellae caused by the significantly different overcrowding in opposite fold surfaces as a consequence of the growth asymmetry introduced by the extant chain tilt. Bassett claimed that it is reordering of the fold surfaces after the growth of crystal lamellae, which initially have no chain tilt that causes S-Bending and drives banding. They also suggested that pressure from cilia trapped between the faces of adjacent lamellae, near giant screw dislocations plays a major role. Schultz proposed that lamellar twisting occurs in order to avoid compositional or stress fields in the melt near the crystallization and they argued that lamellar twisting may be caused by queues of giant screw dislocation of the same band[163].

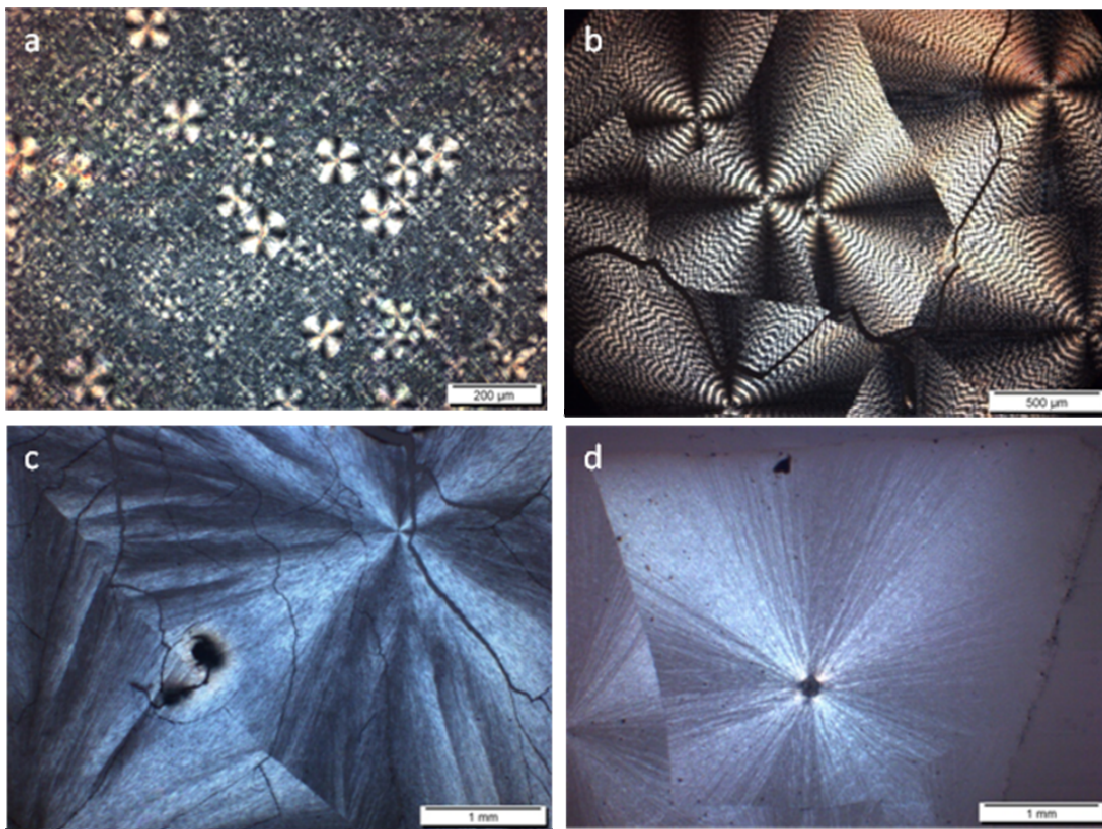


Figure 36: Spherulite morphology of PHB crystallized from a thin melt film at different temperatures (a) T=25°C , (b) T=90°C, (c) T=110°C and (d) T= 130°C

However, a recent study by Xu et al on poly (3-hydroxybutyrate-co-3-hydroxyhexanoate) copolymer showed that the lamellae twisting happened before screw dislocation appear, demonstrating that screw dislocation are not causal of twisting [164]. The ultimate driving force for lamellae twisting is still an open question.

Generally, the actual morphology and the structure of polymer crystallized from a thin melt film depend on the competition of the crystallization rate (ν) of the polymer entities and the

diffusion rate (D) of the melt molecules. Within the range of experimental temperatures, the crystallization rate of the polymer entities decreases with the increase of crystallization temperature while the diffusion rate of melt molecules increases with the increase in crystallization temperature which is schematically shown in Figure 37.

Consequently, at low T_c , $D < v$ is usually observed. In this case, when crystallization occurs in a thin melt film with a uniform thickness, a depletion zone of the polymer melt would form at the growth front of the spherulites due to the slow diffusion rate and the volume shrinkage during the crystallization solidification process, which causes the discontinuous growth of the spherulites to produce the valley and edge structure of the spherulites. This phenomenon has been evidenced by some researchers through AFM observations.[164-167]

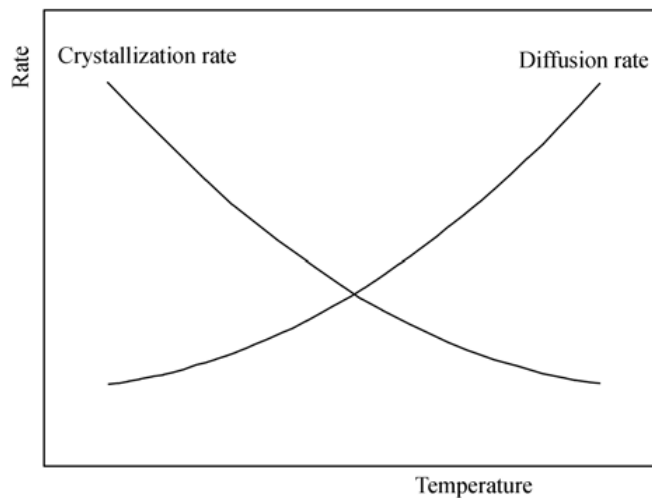


Figure 37: Schematic plots of crystallization rate of polymer entities and diffusion rate of melt molecules versus temperature

With the increase in crystallization temperature the crystallization rate is nearly equal to the diffusion rate. In this case the depletion zone at the crystallization front is too small to observe, but the screw dislocation is still produced by the S-bent lamellae. Therefore, the banded structure of the spherulites can be observed. Bassett et al once reported that the generation of screw dislocation induced by the packing of S-bent lamellae was the main reason for the formation of a banded structure in polyethylene spherulites[168]. With a further increase of temperature the diffusion rate is faster than the crystallization rate. In this case the melt phase at the growth front of spherulites maintains constant and the depletion zone does not appear anymore due to the fast diffusion rate and the surface of spherulite is rather smooth. As a result, no banded structure can be observed. Therefore, it can be concluded that the rhythmic crystal growth and the periodical twisting of the lamellar crystals

are the main reasons for the formation of a banded structure crystallized from a thin melt film.

As it is known from the literature reports on PHB, it is known that the radius (r) of a spherulite linearly increases with time (t)

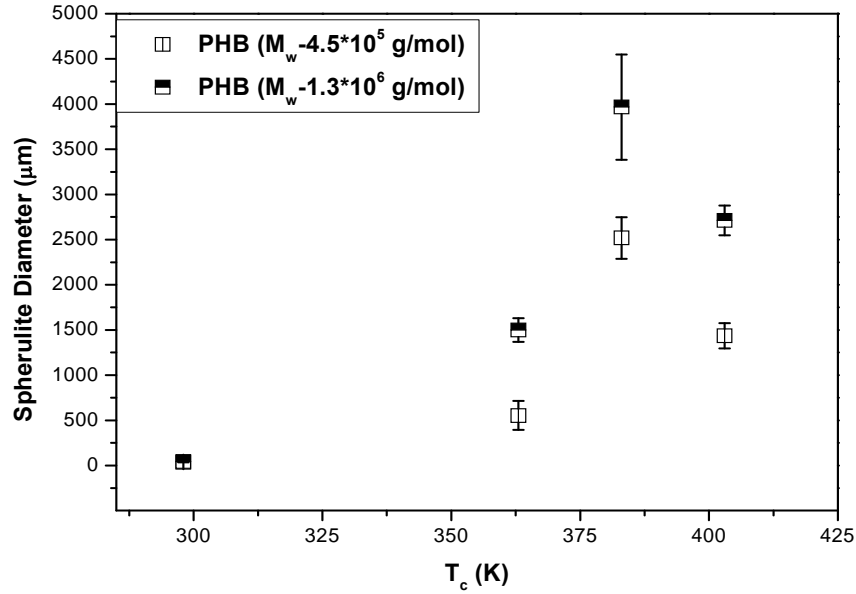


Figure 38: Influence of temperature on spherulite growth rate using polarizing optical microscopy

$$\frac{\partial r}{\partial t} = k(T) \quad (3)$$

In Eq (3) $k(T)$ is a coefficient influenced by temperature. When the volume change is concerned, assuming the thickness of the sample is constant; it can be described as follows

$$V = \pi r^2 H \quad (4)$$

$$\frac{\partial V}{\partial t} = 2 \pi r H k(T) \quad (5)$$

In Eq. (5), H is the thickness of the sample. As H and $k(T)$ are constant when the sample isothermally crystallizes, it is obvious that the volume change rate $\partial V / \partial t$ of the spherulite increases linearly with the increase of radius. The effect of volume change would increase when the radius increases. The maximum growth of spherulite diameter was found at 110°C ($T_{c,\text{max}}$) for pure PHB. It is known that the crystallization window of a crystalline polymer lies

between T_g and T_m^0 . When the crystallization temperature is located toward T_g , the crystallization kinetics is governed by the chain mobility, such that the rate increases with increasing crystallization temperature in this region. In contrast, when the crystallization temperature is located toward T_m^0 , the crystallization rate would be controlled by the thermodynamic driving force for crystallization. Because of interplay of these two factors, a maximum in crystallization rate at $T_{c,max}$ between T_g and T_m^0 would be found.

The acceleration of crystallization at low and intermediate loadings can be explained by the two roles that the nanofillers play in the crystallization: nucleation facilitating the crystallization and physical hindrance slowing growth [169-171]. At low filler concentrations, the distance between dispersed particles is large so it is relatively easy for the additional nucleation sites to incorporate the surrounding polymer. At high concentrations, however, diffusion of polymer chains to the growing crystallite is hindered.

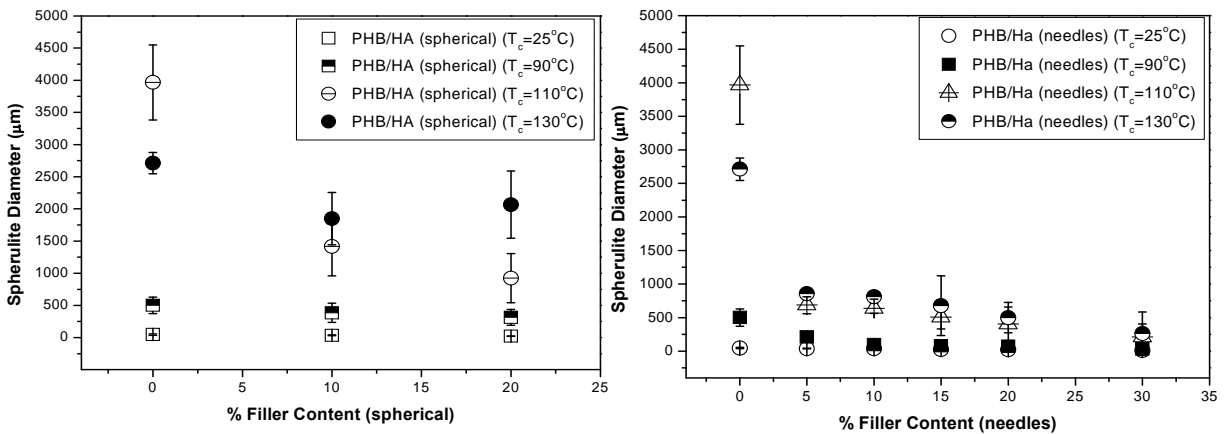


Figure 39: Influence of shape, size and filler content on spherulite diameter for different crystallization temperatures $T_c=25^\circ\text{C}$, 90°C , 110°C , 130°C : a) spherulite diameter on spherical shaped HA Dia-150-200 nm & b) Spherulite diameter on needle shaped HA (L-60-70nm & W-18-30 nm)

The effect of HA nanoparticles varying in shape and size on the spherulite morphologies of PHB was studied by POM. The effect of filler content on spherulite morphology was studied. It can be observed that from optical micrographs, neat PHB has larger spherulites in the range of 500 μm. With the increase in filler content the size of spherulites decreases. As evidenced by the figure (41), nano needles significantly influence in reducing the spherulite diameter than for spherical particles. One of the main reasons for these phenomena is the measure of interparticle distance. Nano needles which are 15-30 nm in thickness can accommodate larger particles in number for a same weight percent compared to spherical particles which are 150-200 nm (diameter). Larger number of particles with small thickness leads to smaller

interparticle distance and this can hinder additional nucleation site for growing crystal and the size of the spherulite is restricted.

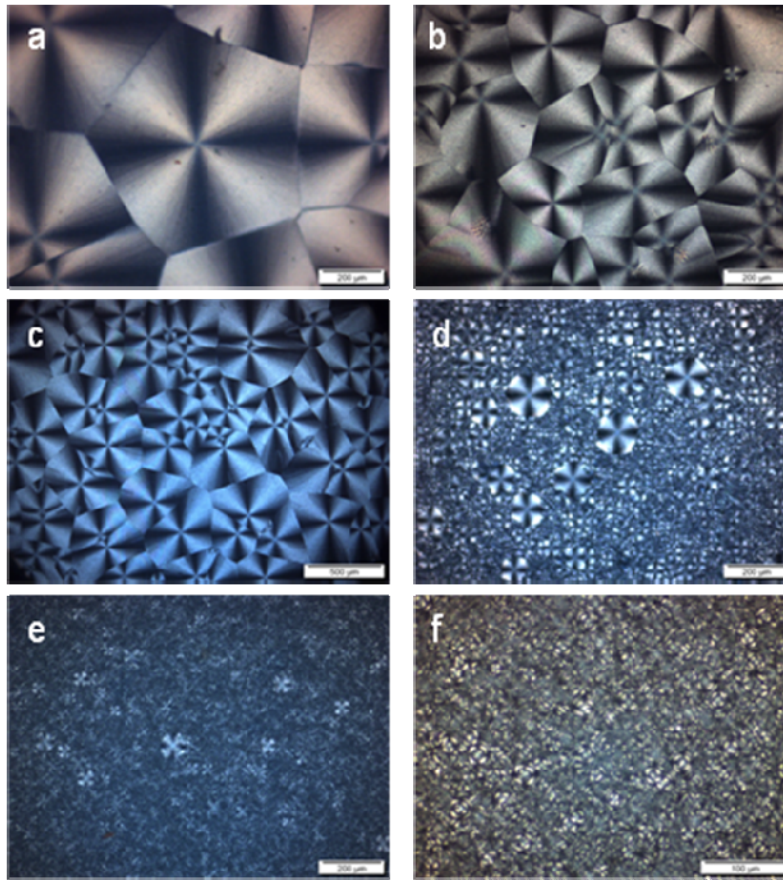


Figure 40: Effect of filler content (5, 10, 15, 20 & 30 wt% needle shaped HA) on the spherulitic morphology of PHB samples that were crystallized at 90°C and cooled at room temperature

Large interparticle distance has larger space for the spherulite to grow and also for nucleating it. The decrease in crystallite size may not be due to the nucleating effect of the filler, rather it may be due to the degree of cooling rate which may be considered. However cooling rate was not controlled for melt crystallized samples. They were cooled at room temperature.

4.4 Differential Scanning Calorimetry

4.4.1 Nonisothermal melt crystallization behaviour of PHBHV/HA nanocomposites

The nonisothermal melt-crystallization exotherms for PHBHV/HA nanocomposites containing 10 and 20 wt% of HA and varying filler size and shape, at five cooling rates (Φ) are shown in Figure 41. From these curves, some useful crystallization parameters, such as the peak temperature (T_p), at which the sample has the fastest crystallization, and the onset temperature (T_c), determined with a method described in the literature [172] can be easily

obtained. The values of T_p and T_c for all systems in this study are listed in Table 10. For a given value of Φ , all T_p values for the PHBHV/HA nanocomposites are consistently higher than those for pure PHBHV irrespective of filler size, suggesting that the addition of HA promotes the crystallization of the polymer. Similar behaviour has been observed at other Φ values (Table I0).

This can be clearly observed in the cooling curves. As the cooling rate increases, T_p shifts to lower temperature both for pure PHBHV and filled systems. When the specimens are cooled with a lower rate during the DSC measurement, they have enough time to form the necessary nuclei and to crystallize. So, the beginning of the crystallization exotherm appears at higher temperature. As the cooling rate increases, the motion of PHBHV and filled systems chains cannot follow the cooling temperature. Hence, the crystallization may occur at the lower temperature. On the other hand, for a given cooling rate in Figure 41, T_p of filled PHBHV increases as filler loading increases. The result indicates that HA in PHBHV matrix can hinder the crystallization of PHBHV so that the crystallization of filled PHBHV needs greater supercooling.

It can also be observed from the curves that both the filler type shows different behaviour. Hence, each type of filler with different loading concentration will be discussed separately. When comparing the effect of HA nanoneedles on the heat flow of the composites with respect to filler concentrations of 10 to 20 wt %, we found that at both the concentrations, a similar behaviour was observed. At HA nanoneedle concentrations (10 & 20 wt%), T_p and T_c is same, but the only difference which could be noticed is the peak height, which is higher in case of 20 wt% nanoneedles. When comparing with pure PHBHV, both T_p and T_c of nanoneedles filled matrix are significantly higher at the same Φ value. This phenomenon can be related to heterogeneous nucleating effect of nanoneedles in PHBHV matrix. HA particles serve as additional nucleators, and their introduction promotes the crystallization of PHBHV. Similar nucleating effects of microscale particles have been reported for polypropylene (PP) composites reinforced with short sisal fibers and silver-exchanged natural zeolite.

In case of nanospheres, T_p and T_c for 10 & 20 wt% are totally different. Here at 10 wt% loading, the values of T_p and T_c are very close to that of pure PHBHV, whereas with increasing filler content upto 20 wt%, T_p and T_c shifts to higher temperature, suggesting higher nucleation effect. On the other hand, the addition of filler reduces the concentration of the polymer in the composite, and this will unavoidably restrict the motion of PHBHV chains to some degree.

It could be attributed that, when fillers such as HA nanoneedles are evenly dispersed, they provide many nucleation sites for crystallization. As the decrease in size of nanoneedles compared to nanospheres, there is increase in net amount of filler particles for a particular weight percent.

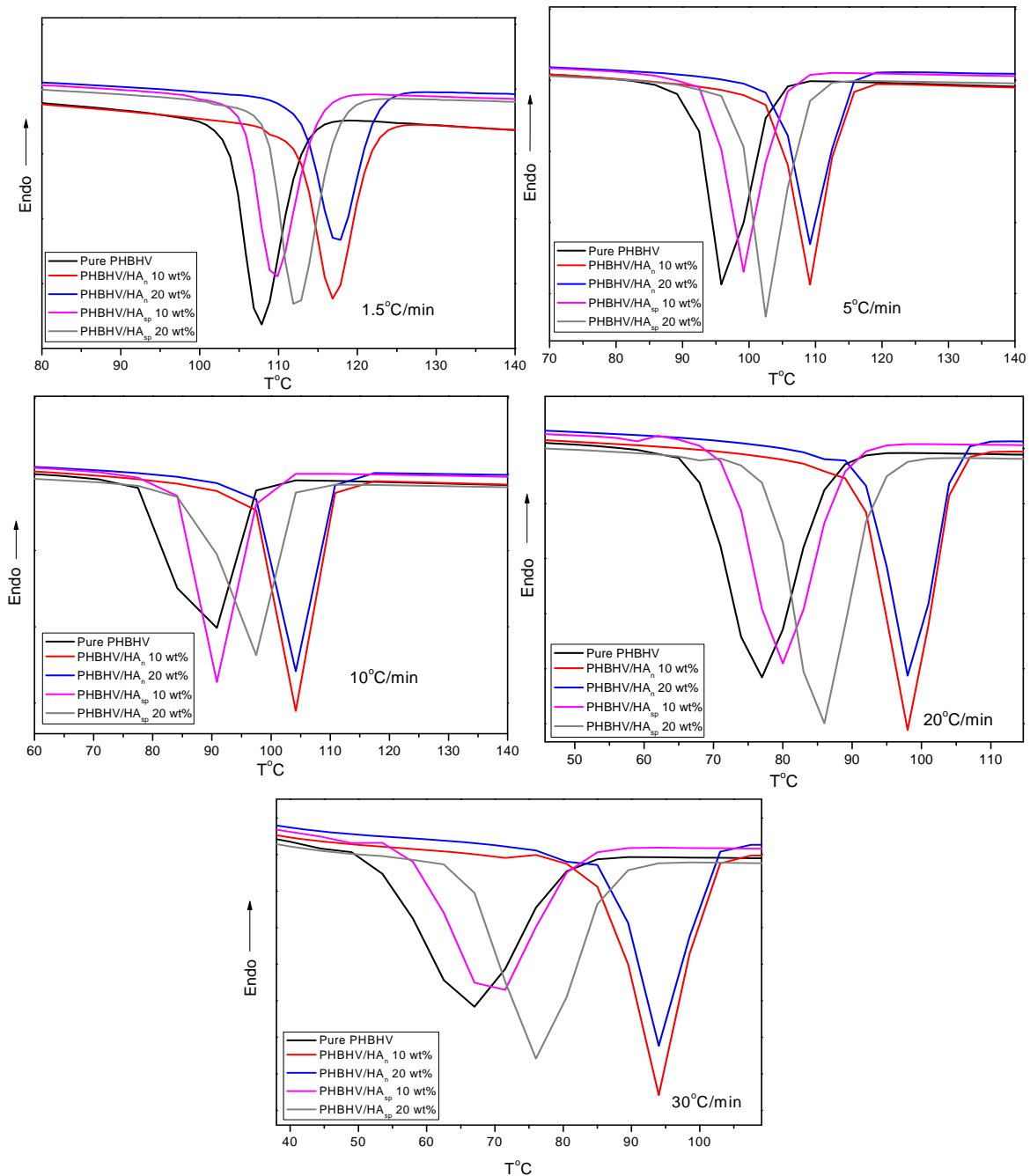


Figure 41: DSC thermogram of PHBHV, PHBHV/Han and PHBHV/HA sp with different filler loading and at different cooling rates: (a) 1.5 °C/min, (b) 5 °C/min, (c) 10 °C/min, (d) 20 °C/min, (e) 30 °C/min.

Bigger sized particles can accommodate fewer amounts. With 10wt% nanoneedles, crystallization peak shifts to higher temperature, whereas in 10wt% nanospheres, the

crystallization peak is shifted towards lower temperature. Even 20wt% nanoneedles also possess same crystallization peak as that of 10wt%.

This could be attributed by the fact that there might be some agglomerations which reduces the amount of separated filler particles to promote additional nucleation sites. At a low HA concentration, the effect of the filler on the polymer concentration is limited, and it is easy for the additional nucleation sites to incorporate the surrounding polymer.

However, at a high level of HA, the diffusion of polymer chains to the growing crystallite is evidently hindered, and so the growth process is retarded. In nanosphere filled systems, due to decreased number of particles, there may be reduced ability to initiate nucleation centres. So, heterogeneous nucleation of nanoneedles is higher than nanospheres. Nevertheless, it is not established to what diameter or shape does the heterogeneous nucleation favoured the most. In general, the combination of a larger number of nucleation sites and limited crystal growth is expected to produce crystals of a fine grain size. Wu and Ke et al. reported that different silica size levels all played nucleation roles in poly (ethylene terephthalate).

Table 10: Nonisothermal Parameters for PHBHV and PHBHV/HA (with different filler shape) composites obtained from DSC Exotherms

Φ (°C/min)	Parameters	1 PHBHV	2 PHBHV	3 PHBHV	4 PHBHV	5 PHBHV
1,5	Tp	107	116	117	109	112
	Tc	114	122	122	115	118
	t _{0.5}	5.95	6.09	6.22	6.96	6.86
5	Tp	95	109	109	99	102
	Tc	103	114	114	104	108
	t _{0.5}	2.51	2,3	2.27	2.4	2,3
10	Tp	90	104	104	90	97
	Tc	98	111	111	98	104
	t _{0.5}	1.38	1.45	1.3	1.47	1.53
20	Tp	77	97	98	79	86
	Tc	87	104	104	88	93
	t _{0.5}	0.87	0.64	0.65	0.92	0.86
30	Tp	67	94	94	71	76
	Tc	80	100	101	82	87
	t _{0.5}	0.75	0.47	0.51	0.74	0.64

The silica with the smallest size of 54 nm possessed the best capacity for accelerating the crystallization of the polymer because the most nucleation centres were supported in this case. Notably, the aforementioned influence of the filler on polymer crystallization has also been seen in nanocomposite systems, such as clay/nylon nanocomposites. Even the same

trend was observed in PHB/HA nanocomposites for both the type of fillers. Nevertheless, only PHBHV/HA nanocomposites as representative materials is dealt in detail.

4.4.2 Nonisothermal Crystallization kinetics

The determination of the absolute crystallinity is not needed for the analysis of the crystallization kinetics, and the degree of conversion or relative crystallinity (X_t) as a function of temperature can be defined as follows:

$$X_t = \frac{\int_{T_0}^T (dH_c/dT)/dT}{\int_{T_0}^{T_\infty} (dH_c/dT)/dT} \quad (6)$$

where T_α is the temperature at the end of crystallization, T_0 is the temperature at which the crystallization begins, and dH/dT is the heat flow rate. During nonisothermal crystallization, time t is determined with the following equation:

$$t = \frac{T_0 - T}{\phi} \quad (7)$$

where T is the temperature at time t . Figure 17 illustrates X_t as a function of the temperature for PHBHV/HA (nanorods) and PHBHV/HA (nanospheres) composites filled with 10 wt % HA at various Φ values.

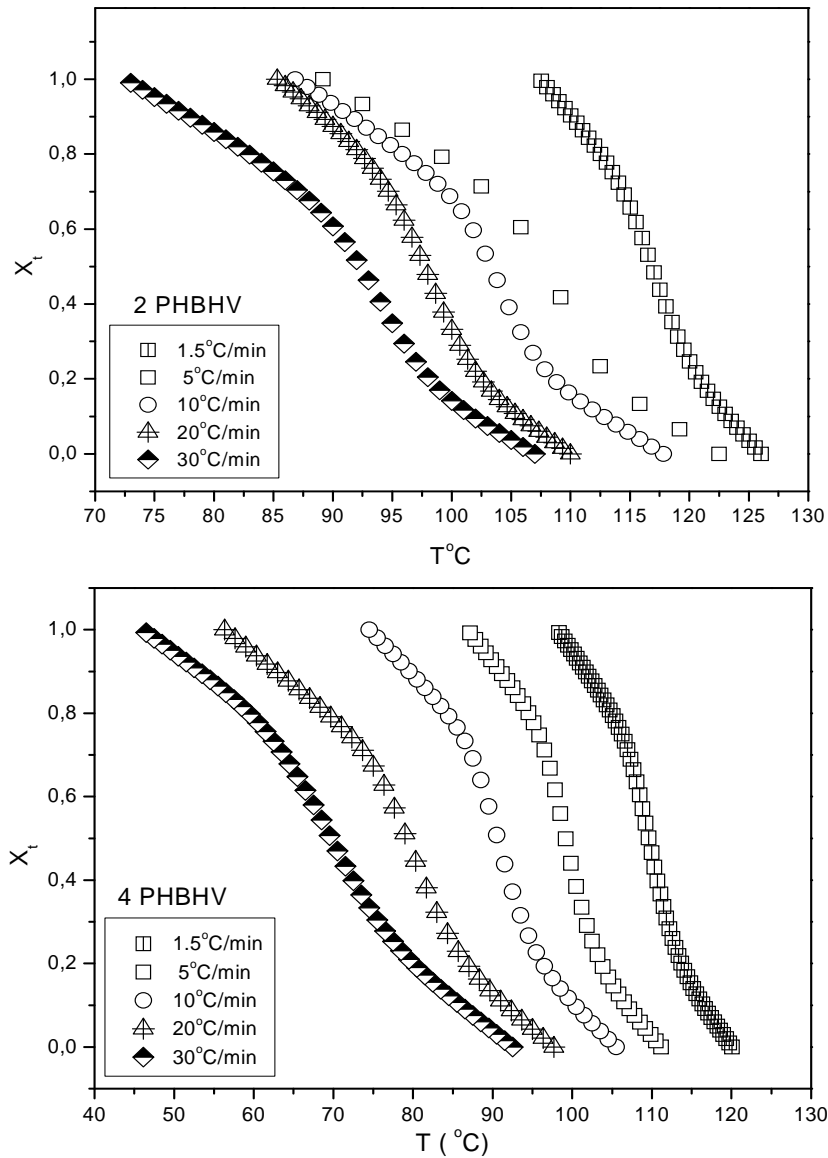


Figure 42: X_t as a function of temperature (T) for PHBV/Han and PHBV/Hasp (10wt %) at various Φ values.

All the curves have the same sigmoidal shape. Once the X_t - T plot was obtained, the conversion into the X_t - t plot was required because the microkinetic models were used. With eq. (6), the temperature scale of Figure 42 can be changed into the timescale of Figure 43. Figure 44 shows that, higher Φ is, the shorter the time is for finishing the crystallization.

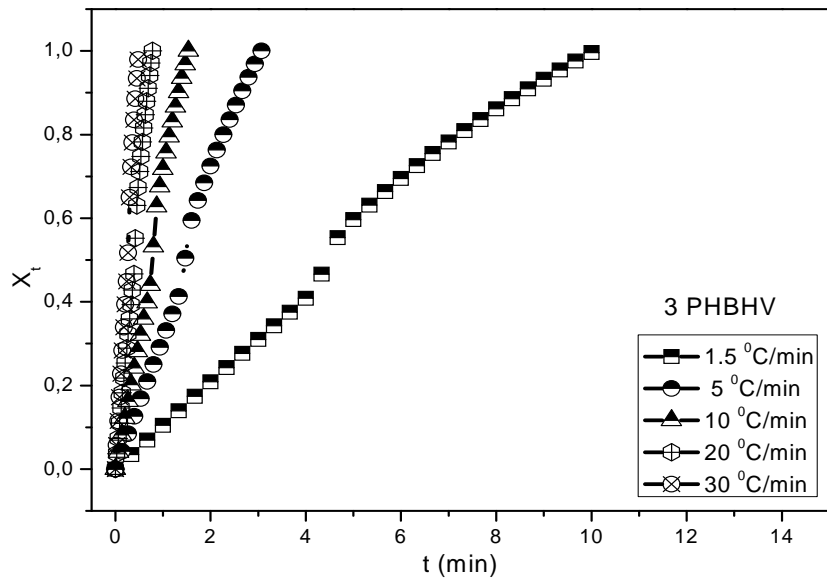


Figure 43: X_t as a function of time (t) for PHBHV/HA (nanorods) 20wt% at various Φ values.

The half-time of crystallization ($t_{0.5}$), another important parameter, can be obtained from Figure 44 at $X_t = 0.5$. Values of $t_{0.5}$ for all systems under study are also listed in Table 10. The $t_{0.5}$ values quite depend on the filler content and Φ . The reciprocal value of $t_{0.5}$ signifies the bulk crystallization rate.

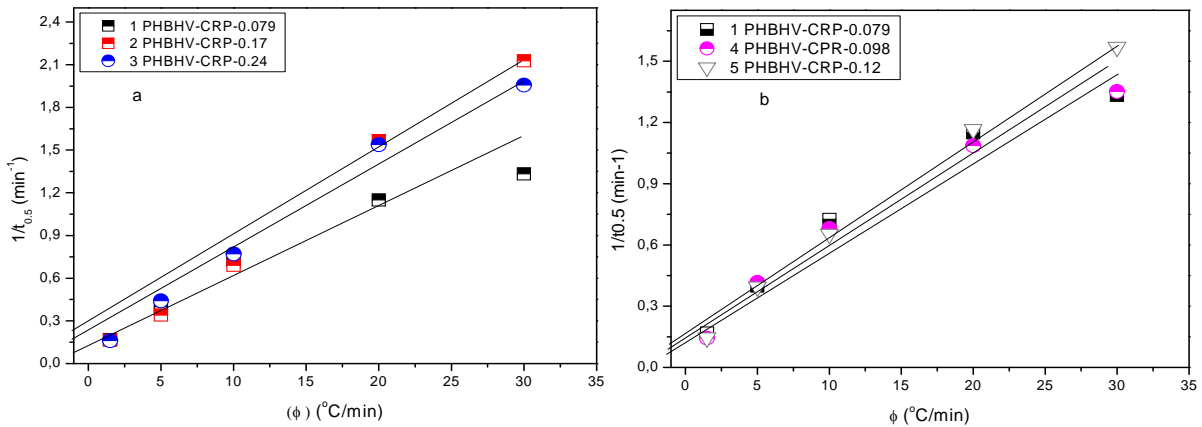


Figure 44: Plots of $1/t_{0.5}$ as a function of volume fraction (Φ), a) Pure PHBHV & PHBHV/HA needle nanocomposites & b) Pure PHBHV & PHBHV/HA spherical nanocomposites with varying filler ratios.

For a given PHBHV or PHBHV/HAn and PHBHV/HA sp composite system, $1/t_{0.5}$ increases with improving Φ , showing that higher Φ values promote the crystallization process. On the other hand, a comparison of the $1/t_{0.5}$ values for all HA contents indicates that the composite with 10 and 20 wt % HA nanoneedles has the fastest crystallization rate. To explore this effect more clearly, the crystallization rate parameter (CRP) was determined. CRP values as determined by the slope of the $1/t_{0.5}$ vs Φ shows that nanorods with 20 wt% has higher value

of 0.24 min^{-1} followed by 10 wt% HA nanorods. Whereas nanospherical particles has lesser values, which confirms that nanorods increases the crystallization kinetics.

4.4.3 Avrami analysis

The Avrami macrokinetic model[173] describes a time dependent relative crystallinity function $X(t)$ for a nonisothermal-crystallization process and can be written as follows:

$$X(t) = 1 - \exp(-Zt^n) \quad (8)$$

or

$$\ln[-\ln(1 - X_t)] = \ln Z_t + n \ln t \quad (9)$$

where Avrami exponent n is a mechanism constant depending on the type of nucleation and growth process and Z_t is a crystallization rate constant involving both nucleation and growth parameters. Obviously, n and Z_t can be obtained from the slope and intercept, respectively, of the Avrami plots of $\ln[-\ln(1-X_t)]$ versus $\ln t$. Considering the nonisothermal character of the process investigated, Jeziorny [174] suggested that rate parameter Z_t should be corrected for the influence of Φ of the polymer. Assuming Φ to be constant or approximately constant, the final form of the parameter characterizing the kinetics of nonisothermal crystallization can be given as follows:

$$\ln Z_c = \frac{\ln Z_t}{\phi} \quad (10)$$

Z_c apparently represents the kinetic crystallizability at a unit of the cooling rate. An Avrami analysis was carried out by the direct linear fitting of the plots of $\ln[-\ln(1-X_t)]$ versus $\ln t$ according to eq. (10). The linear portions of the curves in this study cover a large range of crystallization degrees, about 5–95%, and these portions have been chosen for the determination of the Avrami parameters. Table 11 summarizes the values of n and Z_c for PHBHV and PHBHV/HA composites.

Table 11: Kinetic Parameters for the PHBHV and PHBHV/HA composites obtained from Avrami Analysis

ϕ (°C/min)	Avrami					
	parameter ^a	1 PHBHV	2 PHBHV	3 PHBHV	4 PHBHV	5 PHBHV
1,5	n	3.23	1.12	1.17	2.72	2.1
	Z_c	0.33	0.48	0.47	0.31	0.37
5	n	2.93	1.52	1.08	2.02	1.94
	Z_c	0.78	0.84	0.86	0.84	0.83
10	n	2.74	1.3	1.07	1.44	1.72
	Z_c	0.97	0.95	0.96	0.96	0.94
20	n	2.61	1.07	1.04	1.42	1.51
	Z_c	0.85	1.02	1.01	1.04	0.97
30	n	2.55	1.06	1.03	1.37	1.14
	Z_c	0.95	1.03	1.2	1.01	0.99

Table 11 shows that, almost all the n values are in the range of 3.2–1.0 and drop with increasing Φ . The results agree with the values reported by Chen et al. [172] for PHB and maleated PHB. The Avrami exponent n of pure PHBHV is about 3-2.5 with different cooling rates. The nucleation mechanism and geometry of crystal growth of PHBHV are slightly affected by cooling rates. In general, n = 3 corresponds to two different kinds of possible crystallization mechanism. One is three-dimensional growth and instantaneous nucleation; the other is two-dimensional growth and homogeneous nucleation[175]. So, it is difficult to elucidate the growth and type of nucleation only from the values of the exponent n. Additional information on nucleation, morphology, and even possible mechanisms are necessary to fully interpret the exponent n. The nucleation behaviour of PHB and the effect of nucleating agents (talc and saccharin) on it had been studied by Barham [162]. He drew a conclusion that pure PHB melts may undergo homogeneous nucleation. According to Doi [176], PHBHV crystallize in the same crystalline lattice as homopolymer of the main component when HV content is lower than 40%. From our POM experiment we also observed that the nucleation of PHBHV is at random. In the above experiments even though there is a slight increase in n values with different cooling rate, it can be assumed that PHBHV melts also undergo homogeneous nucleation. So in our experiment, n=3 may corresponds to two dimensional growth and homogeneous nucleation. Where as in filled systems of that of nanoneedles, the n value drastically decreases to n=1.5-1.0 and that of nanospheres, n=2.1-1.0

The HA particles act as heterogeneous nuclei for the initial nucleation and has reduced the value of n and nanoneedles has the least n values, indicating that increased heterogeneous nucleation from nanoneedles, also parameter Zc in case of nanoneedles is higher compared to nanospheres and pure PHBHV.

4.4.4 Ozawa analysis

Ozawa[177] extended the Avrami equation for a nonisothermal treatment. Assuming that the nonisothermal crystallization process is composed of infinitesimally small isothermal-crystallization steps, Xt at temperature T can be calculated as follows:

$$1 - X_t = \left[-K(T) / \phi^m \right] \quad (11)$$

where m is the Ozawa exponent, which depends on the dimensions of the crystal growth, and k is the cooling crystallization function, which is related to the overall crystallization rate. Taking the double logarithmic form, we can rewrite this equation as

$$\ln[-\ln(1 - X_t)] = \ln K(T) + m \ln \phi \quad (12)$$

If the Ozawa method is valid, plots of $\ln[-\ln(1-X_t)]$ versus $\ln \Phi$ should be straight lines, and kinetic parameters $k(T)$ and m should be obtainable from the intercept and slope of the lines, respectively. Figure 45 presents typical Ozawa plots for PHBHV/HAn composite containing 10 wt % filler. In the Ozawa plots, a characteristic curvature can be observed, preventing an accurate analysis of the nonisothermal crystallization data. The continuous change in the slope with temperature makes it clear that m is not constant during crystallization, and the cooling crystallization function $k(T)$ cannot be determined because of the nonlinearity of the curves. The most likely reason for the unsatisfactory description is the assumption during the application of the Ozawa method that the secondary crystallization and dependence of the fold length on the temperature can be ignored and exponent m is a constant independent of the temperature [178]. In fact, except for PHB/HA composites, the crystallization kinetics of some polymer composites, including nanocomposites [179, 180] has also been proved not to be described well by the Ozawa method because for these polymer systems, a large part of the overall crystallization is due to secondary crystallization

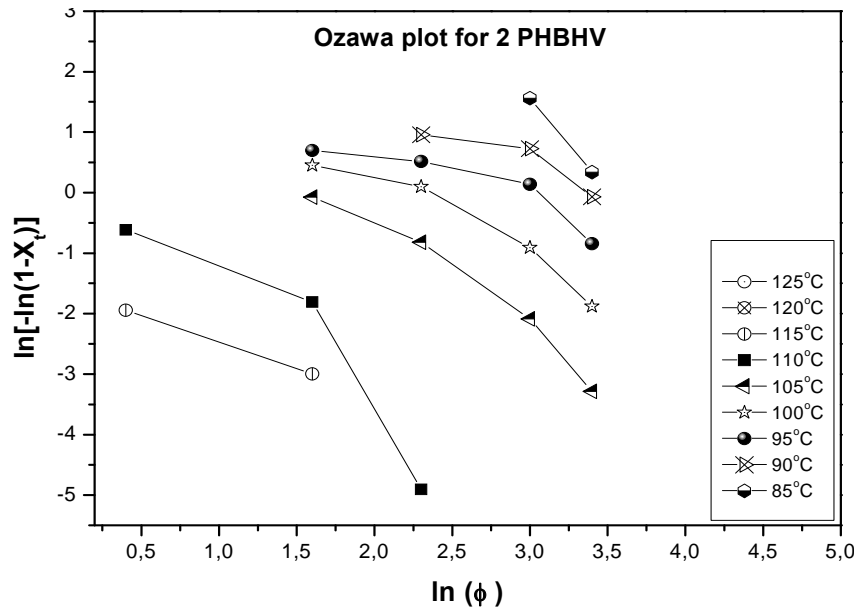


Figure 45: Typical Ozawa plots of PHBV/HA nanorods 10 wt%

4.5 Mechanical Properties

The typical stress–strain curves of the PHB/HA (needles), PHB/HA (spherical), PHBV/HA (needles) and PHBV/HA (spherical) nanocomposites are shown in Figure 46. For all nanocomposites, the curves show that Young’s modulus increased with filler content. Major difference observed in both PHB and PHBV matrix was the elongation at break. The variation of mechanical properties such as young’s modulus and yield stress on filler content is shown in Figure 46. Yield strength of the polymer changed slightly between two filler types, but there was drastic increase in yield strength when compared with unfilled system.

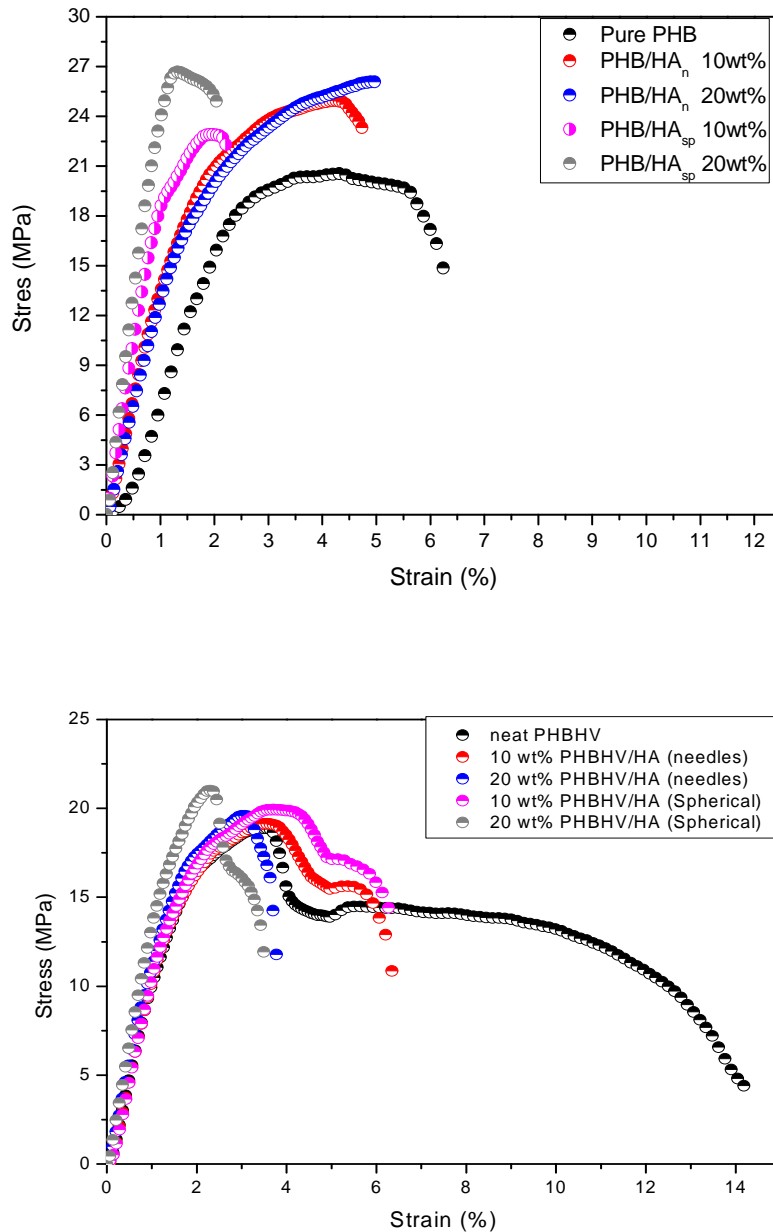


Figure 46: Typical stress-strain curves of a) PHB/HA (n), PHB/HA (s) and b) PHBHV/HA (n), PHBHV/HA (s) nanocomposites with different filler contents.

This could be highly attributed to the filler present. Yield strength of pure PHB was about 16 MPa and that of 20 wt% filler system had 28 MPa. Also young's modulus of filled system had tremendous influence. Pure PHB which had young's modulus of nearly 1 GPa, while that of 20 wt% of PHB/HA(spherical) had 3 GPa. Nevertheless young's modulus of 10 wt% for both the fillers did change slightly. Elongation at break for pure PHB was about 7 % while that of Pure PHBHV was 14%. This drastic change in elongation is due the copolymer unit

which renders the polymer ductile. PHB which has more than 80% crystallinity behaves brittle system. More of the melt crystallized samples of PHB will have cracks which results due to physical ageing.

4.5.1 Correlation to Halpin-Tsai Model

Young's modulus data obtained by tensile testing was interpreted by using a simplified version of the Halpin–Tsai model. According to the Halpin–Tsai model, Young's modulus of a composite can be expressed in terms of the corresponding properties of the matrix and the filler, together with their proportions and the filler geometry, using Eq. (3)

$$E_r = \frac{E_c}{E_m} = \frac{1 + \xi \cdot \eta \cdot \varphi}{1 - \eta \cdot \varphi} \quad (13)$$

and

$$\eta = \frac{(E_f/E_m - 1)}{(E_f/E_m + \xi)} \quad (14)$$

In Eq. (13), E_r is the relative Young's modulus and E_c , E_m , and E_f are the moduli of the composite, matrix, and filler, respectively; φ is the filler volume fraction. The Halpin–Tsai model assumes the filler to be firmly bonded to the matrix. The factor $\xi=2$ (L/D) describes the influence of the geometry of the reinforcing phase, where L/D is the aspect ratio, E_f is 100 GPa [181].

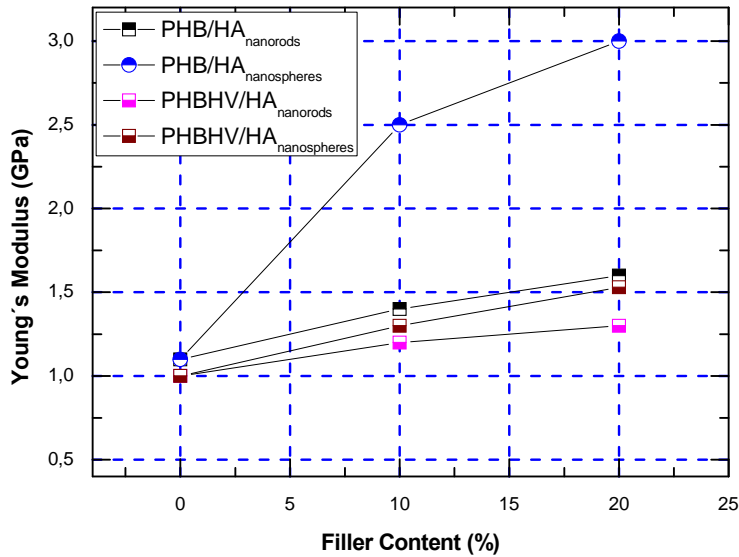
Eq. (13) assumes that the fibers are oriented. In our case, we are dealing with very short fibers that are randomly oriented. In this situation Schaefer and Justice found that Eq. (15) simplifies considerably assuming rigid fibers at low volume fraction[182].

$$E_r = 1 + 2 \left(\frac{L}{D} \right) C_a \varphi \quad (15)$$

where the angular factor, C_a is approximately 0.2 [183] Eq. (15) is relevant to the systems studied here, since it shows that large aspect ratio, L/D , is essential for fiber reinforcement. Eq. (15) assumes $L/D \rightarrow 1$, the Smallwood limiting law[184] for independent spherical particles obtained, which is independent of the filler size.

$$E_r = 1 + 2.5\varphi \quad (16)$$

Elongation at break for both PHB/HA and PHBV/HA filled with nanoneedles had higher elongation. There are many reasons which controls toughness enhancement in the polymer nanocomposites. One main reason is the dispersion, which greatly influences the mechanical properties. In both the nanocomposites, good dispersion of HA nanoparticles at 10 and 20 wt% was achieved. Nevertheless, with increase in filler content, the size of the agglomerates increases and their distribution broadens. In 10 wt% nanoneedles the average agglomerate was about 300-500 nm and that of spherical nanoparticle was 800-1200 nm. These large agglomerates lead to cracks leading to catastrophic failure. Another reason for the toughening enhancement is the volume fraction of particles. Higher volume fraction leads to smaller interparticle distance. Nanoparticles give smaller interparticle distance when compared to larger size nanoparticles. Table 1 shows the interparticle distance with filler content.



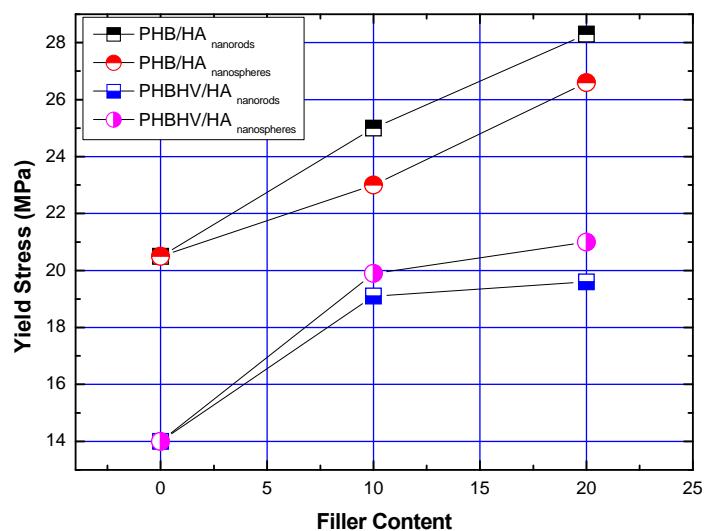


Figure 47: Young’s modulus values of PHB/HA (n), PHB/HA (s) and PHBHV/HA (n), PHBHV/HA (s) nanocomposites with different filler contents.

Table 12: Comparison of Average Particle (Agglomerate) Diameter (D) and Average Interparticle Distance (ID) of Investigated Nanocomposites

Sample	wt % filler	Avg Particle diameter	Average ID distance(nm)
PHB/HA sp	10	120-160	330
PHB/HA sp	20	120-160	140

Michler et al. suggested that, to maintain good toughness in polymer composites with semicrystalline matrix, there are some limiting factors. a) particle diameter not too large and particle size distribution not too broad, b) interparticle distance (ID) smaller than a maximum ID_{max} and larger than a minimum distance ID_{min} , c) no strong, perfect interfacial bonding (interfacial strength between particles and matrix), so as to permit partial, localized debonding under load.[185]

The mechanical properties of polymer nanocomposites can be affected by many factors, such as the interaction between particles and a polymer matrix, crystallinity of the polymer, spherulitic morphology, molecular weight of the polymer matrix, dispersion state of the particles in the polymer matrix, etc.

Matrix characteristics do not change significantly in the nanocomposites. It was also evidenced from DSC data, the transition temperature (T_g) for all the samples did not change, indicating that there are no strong attractive or repulsive interactions between the nanoparticles and the polymers. Therefore, the interfacial adhesion between them must be weak. From the tensile testing results, the neat PHB is stiffer but less ductile than the neat PHBHV. The major difference between the neat PHB and the neat PHBHV is their percent crystallinity. For PHB the percent crystallinity is about 80-85% and that for PHBHV is 60 %. Crystallinity is reduced from 85-60% which is almost 25% reduction. Given that the long period (L) is about 6 nm, and the average size of the crystalline and amorphous phases is about 3 nm, the reduction of crystallinity is accounted for by minimal alteration of the interface region between lamellar stacks and spherulites. More over PHB with its high crystallinity results in very big spherulitic superstructures. Radial and circumferential cracks are often observed in PHB due to embrittlement. This causes the material to fail catastrophically. It was also observed that morphology of spherulites has a major role in mechanical property determination. With the addition of fillers it was observed that the spherulite diameter gradually reduced, which eventually reduces premature cracks caused by larger spherulites. Even though there is often observed some reduction of spherulite diameter in filled systems, it was observed that all the filled systems had reduced ductility compared to neat samples. This was due to contribution of hard fillers which drastically alters the micromechanical deformation processes.

All the samples showed stress whitening during tensile testing. Plastic tensile deformation of crystalline polymers can cause cavitation, producing sudden polymer whitening near the yield point. Michler et al. [186] studied the influence of molecular weight on the micromechanical deformation and found that their significant differences are connected with the decreasing thickness of the amorphous material between lamellae and also with crystallinity. Cavitation in the amorphous phase, therefore, cannot be stabilized and local stress concentrations result in longer crazes and a transition from ductile to quasi-brittle behaviour.

If the interfacial adhesion is not high, debonding at the particle– polymer interface can occur, leading to crazing and/or shear yielding. In our case, this mechanism has been actively in samples filled with needles which fractured with a slight necking that led to a more ductile behaviour.

Although void formation is a secondary factor contributing to toughness (in other words, only a small part of energy dissipation may contribute to toughness), it plays an important role for

the activation of further plastic deformation [187]. When filler loading is low (10 wt%) the formation of nanovoids releases strain constraints and induces local shear deformation in polymer ligaments between nanoparticles. As loading increases, however, the aggregates act as flaws, which trigger brittle response and premature material failure before the shear yielding is able to start. However it is known that interparticle distance (D) between well dispersed particles play a crucial role in toughness enhancement. It is also known that at a given particle diameter (D), the interparticle distance decreases with increase in volume percent, if at all the particle dispersion is achieved at highest percent. However the aggregates of spherical particles which are higher than $1\mu\text{m}$ led to brittle failure by decreasing elongation at break. In nano needle filled nanocomposites PHB/HA, PHBHV/HA the deformation mechanism is the modulated crazing: nanoparticles favor the initiation of nanovoids leading to stress concentration in the adjacent matrix strands, to yielding and fibrillation of the matrix polymer. The size of the voids inside the cavitated/fibrillated craze structure depends on the size of nanoparticles or agglomerates of particles. The easy debonding of particles from the matrix polymer generates easy cavitation, reducing the effective stress for crazing. Therefore, this type of “nanoparticle modulated craze” acts as a source of additional toughness enhancement. This was evidenced by ultra thin deformed samples of nanocomposites which showed the above mentioned phenomena [185].

To get further insight on micromechanical processes, young's modulus data was interpreted by using Halpin-Tsai. In our case, however, the modulus is not only dependent on the matrix involved.

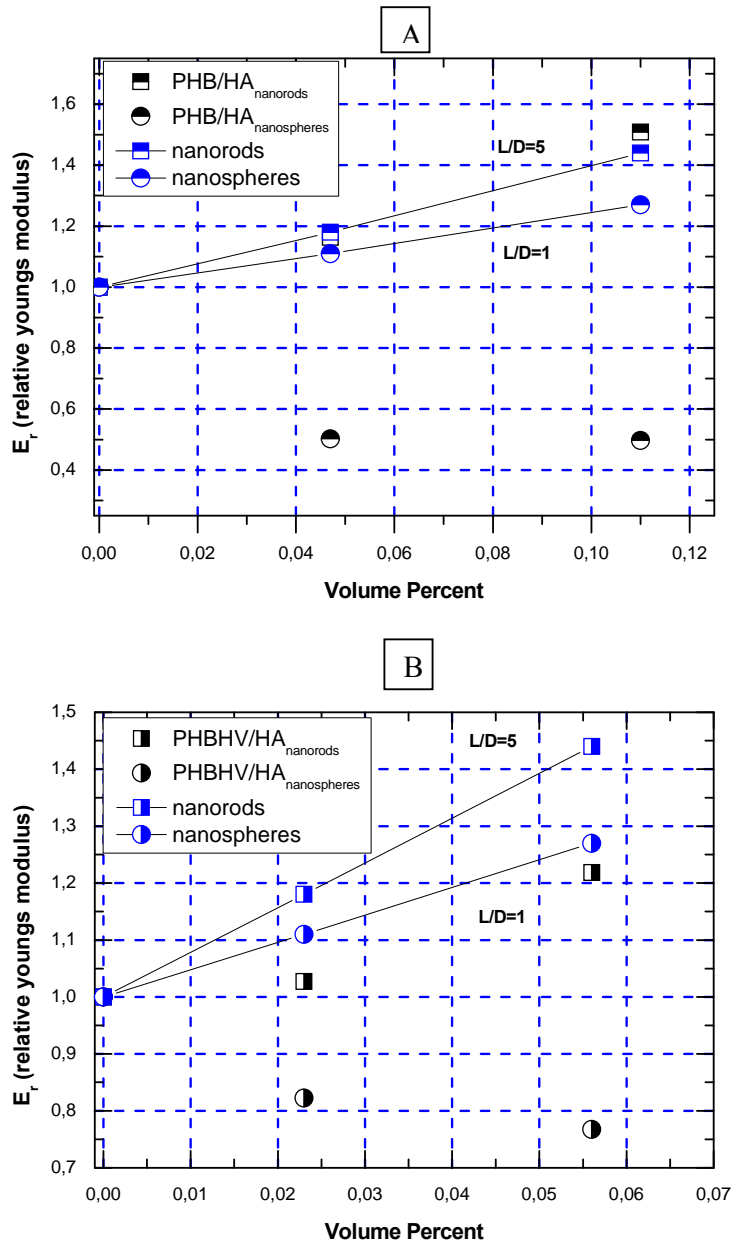


Figure 48: Measured relative modulus from the data obtained by tensile testing. A) relative modulus of PHB/HA(n) and PHB/HA (s) nanocomposites and b) relative modulus of PHBHV/HA(n) and PHBHV/HA (s) nanocomposites

In both the matrix systems, yield stress, young's modulus and elongation changed slightly for neat and nanoneedles filled composites. But the modulus value for spherical Ha filled composites was far greater than the needles HA composites, inspite of brittle failure experienced in the former. This drastic change can only be accounted for the additional stiffness provided by the spherical particles to their respective matrices. Figure 48 shows the experimental values of $E_r = E_c/E_m$ and the predictions based on simplified Halpin-Tsai. Both the systems doesn't fit exactly to the predictions. However nanoneedle filled composites

stays in the error bar of the predicted data, whereas the nanospherical filled composites falls out of the error bar.

Eqs. (15) and (16) assume independent, rigid particles so that the elastic energy is stored in the strain field around the particles. In principle these equations could be altered for aggregated particles. Interactions between the strain fields of the primary particles would alter these simple predictions. Moreover, this prediction only represents minimum expected reinforcement and neglects the energy stored in the filler itself [188].

Some insight into the anomalous modulus enhancement for the PHB/HA and PHBHV/HA with spherical particles comes from the observation that the enhancement would be “normal” if the modulus of the unfilled materials was under estimated by 30%. That is if the modulus of the filled samples is extrapolated to zero loading, the intercept is too high by about 30%. This observation leads us to believe that the enhancement is due the impact of the filler particles on the matrix. Given that a semicrystalline polymer PHB and PHBHV with wide degree difference in crystallinity is itself a composite consisting of a stiff crystalline regions and more elastic amorphous regions, simple 2-component micromechanical models like Halpin–Tsai may not be adequate to account for observed enhancement.

4.6 Micromechanical Deformation Processes of nanocomposites

For any particulate filled nanocomposites, the micromechanical mechanism governs the final mechanical properties of nanocomposites. In short, the strength of particulate-polymer nanocomposites relies on the parameters of particle size, interfacial adhesion and particle loading. Deformation mechanisms of particulate filled nanocomposites were analysed by SEM and TEM. Two different particulate fillers varying in size and shape have been dispersed in PHB and PHBHV matrix. The primary particle size of HA nanoneedles were 18-30 nm thick. Agglomeration resulted in increase of particle size at higher filler loading. Even the largest agglomerate was less than 1 μm , where as in nanospheres the agglomerates were bigger in size. Deformed samples showed different behaviour in both the systems. All the filled samples showed increase in yield stress compared to neat polymer irrespective of filler loading. The trend suggests a difference in evolution of voids in these samples due to debonding of HA in polymer matrix. Figure 49 shows the deboned HA sp in PHB matrix in

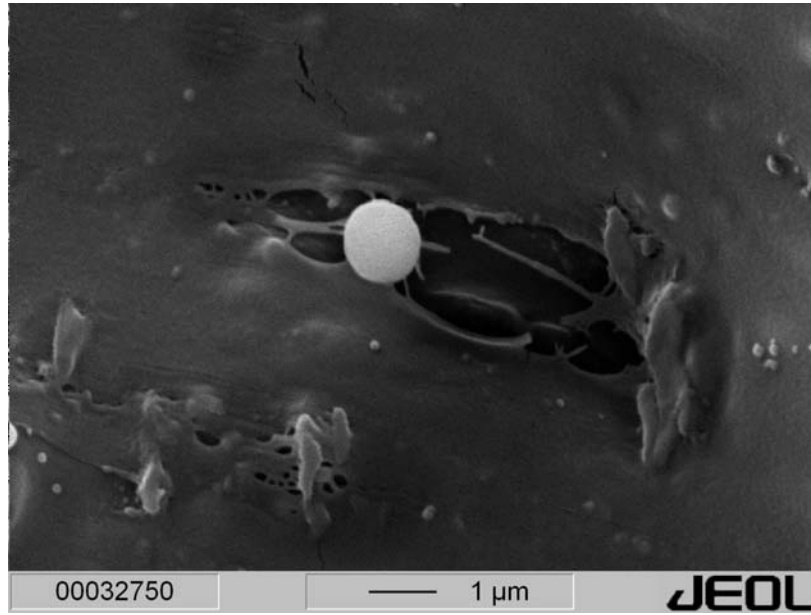


Figure 49: Debonded HA spherical particle surrounded by the void created due to deformation of the PHB/HA_{sp}.

the deformed sample. When tensile curves were analyzed, it was observed that with varying filler content, there was slight variation in maximum stresses in both 10 and 20 wt% filler particles. This is because the formation of voids will reduce the apparent yield stress of the composites. It can also be predicted that not all the particles eventually debonded in the experiments. When carefully considering the tensile strain curves, it is observed that, with nanoneedles as filler content, there was drastic increase in strain to break for both the matrix, whereas for nanospheres, there was brittle failure of the samples. To understand the possible toughening effect in both the filled systems, it is worth to analyse the effect of contributing phases.

In the present system, the size of nanoneedles are $d=18-30$ nm and $L=70-100$ nm and that of nanospheres are $d=150-200$ nm. This large difference in aspect ratio makes nanoneedles filled matrix as better nanocomposites. Nevertheless, improved properties of nanocomposites are due not only of intrinsic properties of the nanoparticles alone, but also because of contributing micromechanical mechanism caused by the effect of interphases and interfaces between matrix and fillers.

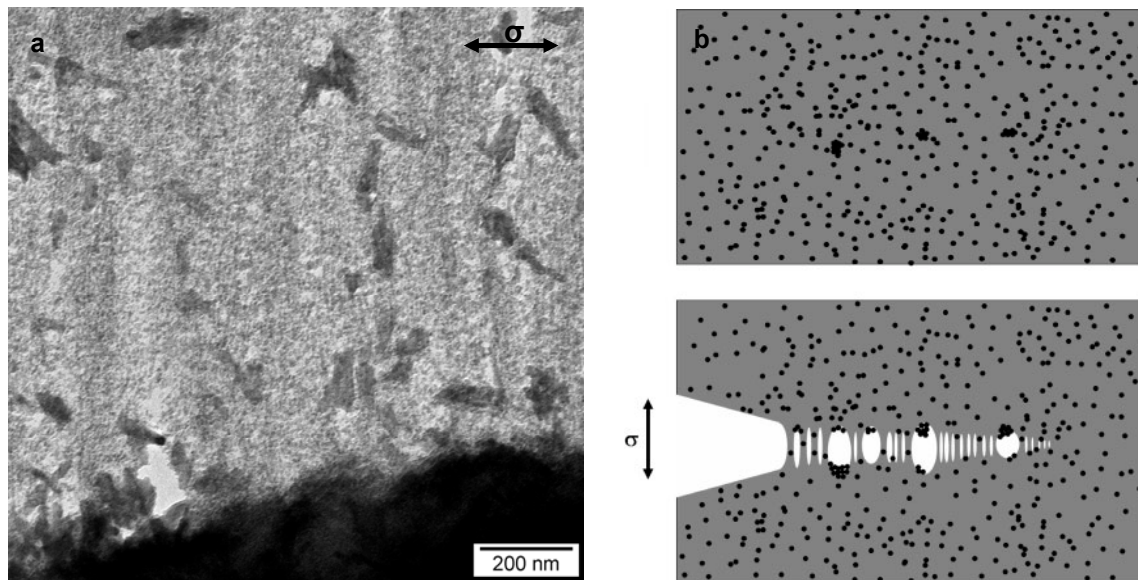


Figure 50: a) Internal craze structure in PHB/HAN nanocomposite with 10 wt % particle content: debonded particles, nanovoids, and fibrils. Solution-cast film, deformed, TEM. B) Schematic representation of craze formation in a PHB/HA nanocomposite

The above figure 50 demonstrates deformation behaviour of PHB/HA nanocomposites. The deformed sections of PHB/HA needles shows craze structure. The craze structure is modulated by larger nanoparticle agglomerates, which generate larger voids by debonding and partly coarser fibrils between them. The larger magnification of Figure 51 demonstrates the interrelation between Ha needle particles, debonding, nanovoid formation, and fibrillation. With increasing particle content larger agglomerates appear, creating larger voids inside the crazes (Figure 51).

Also, due to nanoneedles the fracture events were modified. As the filler content increases, with slight agglomeration can result in microvoids. These microvoids can help in crack wandering and can result as means to stop cracks. With this event crack can propagate around the microvoid thereby creating an island of unstressed region. Such phenomena lead to multiple cracks all over the sample and can absorb energy leading to enhanced toughness. Figure 51 demonstrates such a mechanism for PHB/HA filled with 10 wt% HA nanoneedles.

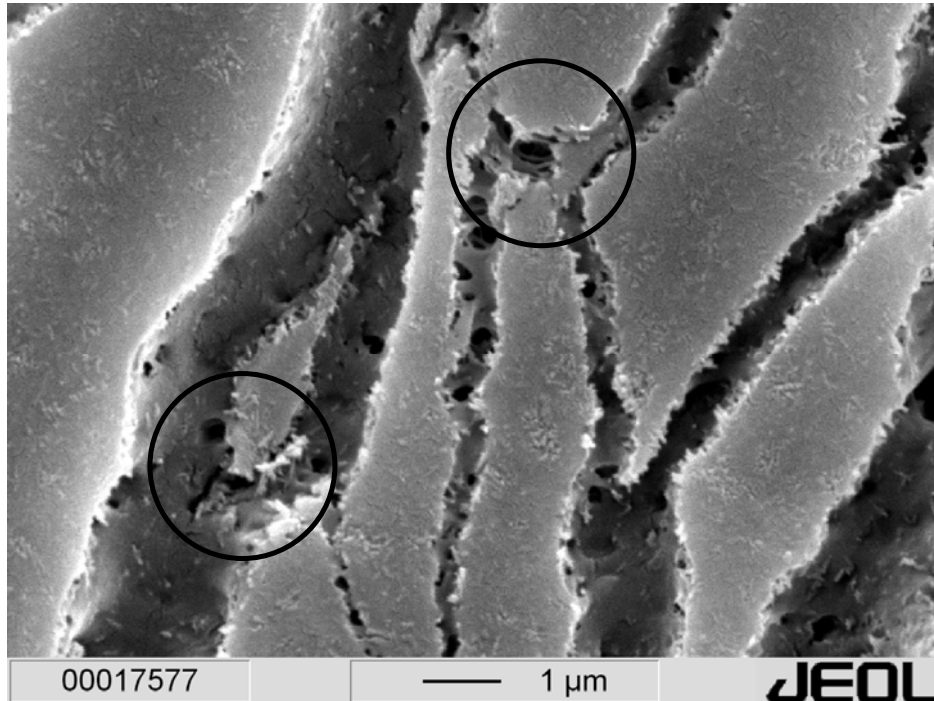


Figure 51: SEM micrograph of PHB/HA nanoneedles 10 wt% demonstrating multiple fracture events due to fillers which enhance microvoid formation. Circle shows a microvoid, which has deviated the main crack growth.

The modulated craze structures visible in Figures 52a reveal a modified crazing mechanism as compared with the usual mechanism in PS: as sketched in Figure 50b, particle agglomerates are breaking up and/or are debonded from the PHB matrix, generating smaller or larger voids; the PHB strands in the voided structure are then stretched into fibrils. Here, the breaking up or debonding stress determines the crazing stress, which is lower than that in unmodified PHB. Therefore, slight agglomeration makes crazing easier and more crazes can be created with a positive effect on toughness. It is also well established that the interparticle distance between dispersed particles plays a crucial role in the toughening mechanism in heterogeneous systems. The interparticle distance measured in PHB/HA nanocomposites was in the range of 90-120 nm and this decreased with increase in filler loading. Due to smaller interparticle distance and good adhesion effect between nanorods and matrix, there is increased plastic deformation, which results in stretching of fibrils. This effect induces energy dissipation, resulting in toughness.

In contrast, the larger spherical particles (180 nm) would preferentially undergo single debonding process. As a matter of fact, the particles being rather well dispersed, the maximum stress concentration lies in the polar regions of the filler, which will activate a debonding process. Around a particle, a void is developed as shown in figure (49), which appears as elliptical with longest axis along the traction one. The void length along the

traction axis is much larger than the dimension of filler. Agglomerates creates voids, but very less comparable to nanoneedles. Due to larger void length, the matrix undergoes brittle deformation before fibrillation. Hence, nanocomposites with spherical particles undergo brittle failure without matrix yielding.

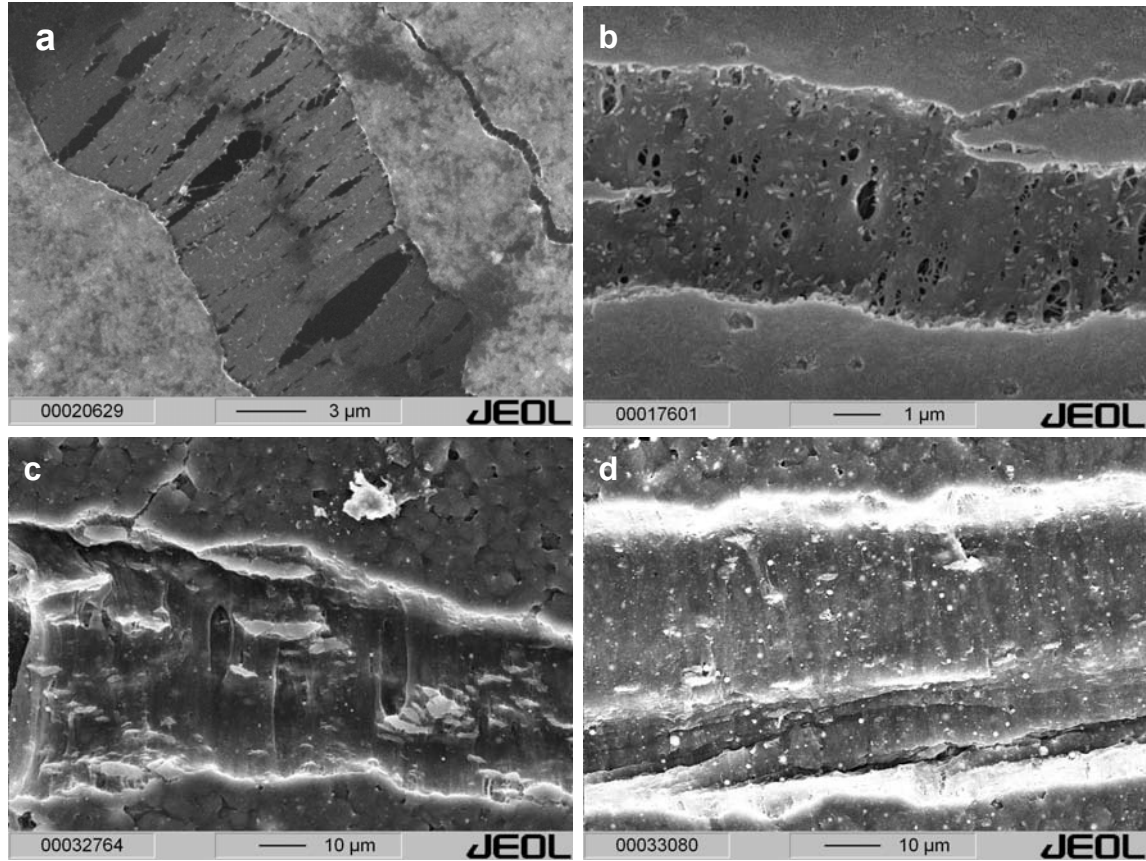


Figure 52: Crazes in PHB/HA nanocomposite with 10 & 20 wt % particle content. a & b) PHB/HA needles- Craze structure is modulated by nanoparticle agglomerates, generating larger voids inside the fibrillated crazes. Solution-cast film, deformed, SEM, c & d) PHB/HA-spherical – Crazes are formed by agglomerates with large voids which results in early failure.

4.7 Microhardness

It has been reported that Vickers hardness of bioceramic–polymer composites increased with the increase in bioceramic volume in the composites. Figure 53 shows Vickers hardness (VHN) for the PHB/HA and PHBHV/HA composite, in which an ascending trend of Vickers hardness is observed with the increase in HA volume percentage and size of nanoparticle. Although the hardness of a material is actually determined by the compressive yield strength of the material, it is shown to be a fairly good predictor of the Young’s modulus for mineralized tissues and it was observed that the relationship between Young’s modulus and Vickers hardness was close to a linear one for both human cortical bone and bioceramic–

polymer composites. However, it was found in the current investigation that Young's modulus from tensile testing and microhardness of composites did not follow a linear relationship. It is thus obvious that with regard to the relationship between Young's modulus and Vickers hardness, different composite systems need to be treated differently. As pointed out previously, using a much simpler mechanical testing method such as microhardness testing instead of tensile testing has significant practical advantages in assessing mechanical properties of new biomaterials, especially when there is a very limited amount of the new biomaterial for characterization and evaluation. For comparison, mechanical properties of PHB/HA and PHBHV/HA composite obtained from tensile testing and microhardness testing are tabulated in Table II. In comparison to homopolymer (PHB) and copolymer of PHBHV, microhardness for pure PHB was 268 MPa and that of PHBHV was 108 MPa. Variation in hardness is dependent on the crystal structure, crystallinity and also molecular weight. PHB homopolymer has crystallinity on the order of 80-85%, whereas crystallinity of copolymer varies with the percent of hydroxyvalerate content. In the present study, HV content was 12% and its crystallinity as measured by DSC was about 40%.

Nanocomposites of PHB/HA and PHBHV/HA showed increasing trend in hardness values with increasing filler content. In PHB/HA nanocomposites, hardness of nanocomposites filler with nanoneedles increased from 268 MPa for pure PHB to 312 MPa for 20 wt% loading. This increase in hardness is attributed to hardness of nanoHA which is around 600 MPa. Moreover, relatively uniform distribution of HA nanoparticles and decrease in interparticle distance with increasing particle loading in the matrix results in increase of resistance to indentation of PHB and PHBHV matrix. On the contrary matrix loaded with HA spherical particles showed higher hardness compared to needle shaped particles. For 20 wt% loading of HA spherical particles to PHB and PHBHV matrix, the hardness values increased from 312 MPa to 385 MPa (PHB matrix) and this trend was also observed for PHBHV matrix, the values of which are tabulated in the table.

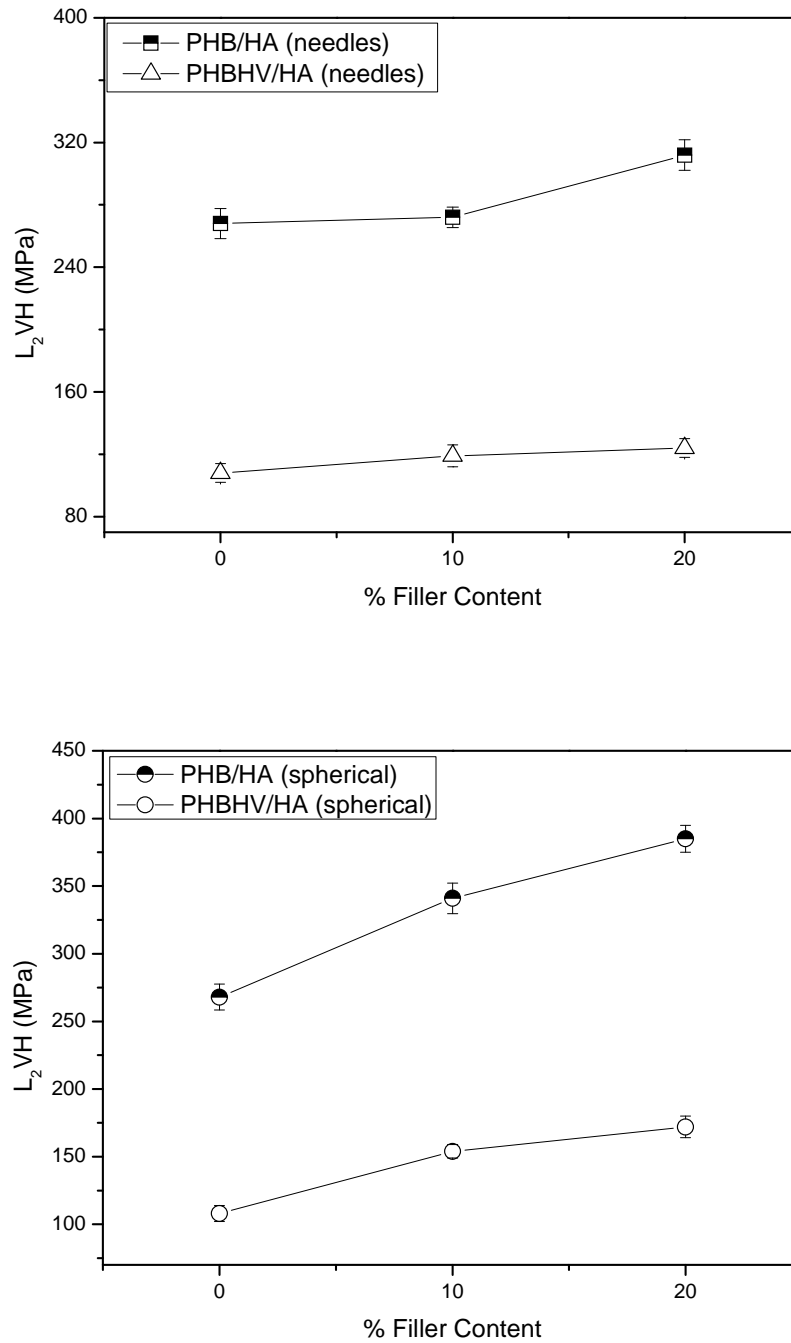


Figure 53: Microhardness as a function of filler content. a) Nanorods and b) Nanospheres

Figure 54 shows SEM micrographs of Vickers indentations made on HA/PP composite from microhardness testing. These micrographs reveal good interlock between HA particles and PHB matrix for composite of all compositions. As Vickers hardness testing is basically compression testing using a pyramid-shaped diamond indenter instead of a flat surface

compression platen, the material around the sharp tip and edges of the indenter was squeezed and deformed plastically. Unlike the condition of a tensile force, such a compressive stress condition would not cause debonding at the PHB/HA interface. Therefore, bioceramic-polymer composites with a weak interfacial bond such as PHB/HA is better suited for the compressive loading condition than for the tensile loading condition. As the matrix is a tough polymer in comparison to HA (i.e., PHB), no microcracks were generated at the sharp corners of indentations on PHB/HA composite and no material came off the composite surface during or after microhardness testing (Figure 53).

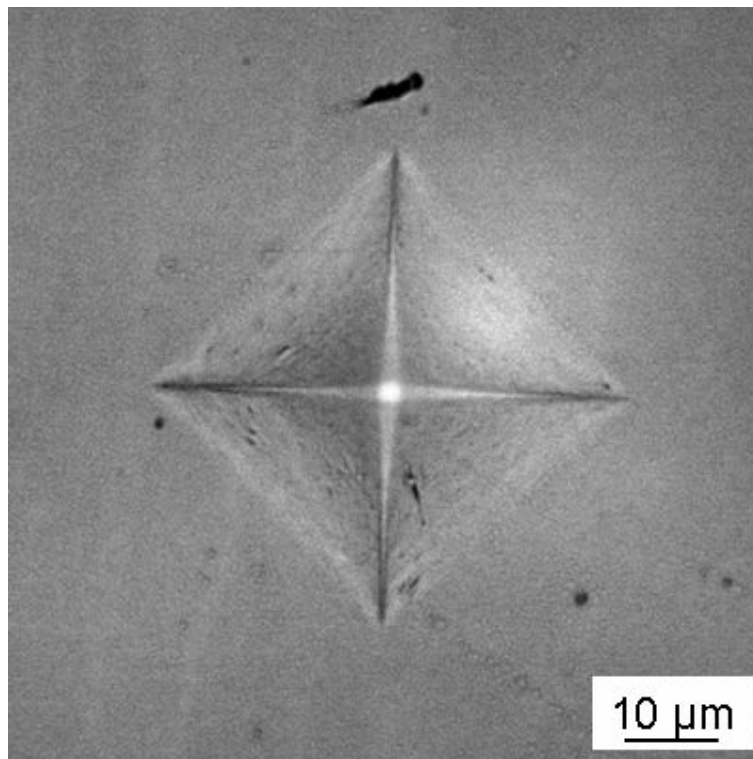


Figure 54: Optical micrographs of micrographs of Vickers indentations made on surfaces of PHB/HA (n) 10 wt% composite

Wang et al. have observed a drastic change in indentation area on testing of bulk HA, where microcracks emanated from the corners of a Vickers indentation or chipping occurred on sintered HA during microhardness testing because HA is a weak ceramic (and as a ceramic, it is also brittle). The HA chips caused by the propagation of Vickers indentation-induced lateral cracks either fractured or came off the HA surface easily. The provision of toughness by the matrix polymer is certainly an appealing feature of HA-containing polymer composites which overcome the shortcomings of brittleness and weakness of HA while providing bioactivity through HA.

In any composites, the actual value either for tensile testing or for indentation measurements, the values for both depends on the combined effect of contributing phases. To analyse the composite hardness, rule of mixture (ROM) for composites have been evaluated. Accordingly, ROM is shown in eq 17

$$H_c = H_f V_f + H_m V_m \quad (17)$$

where H_c , H_f and H_m are hardness of composite, particle and matrix respectively.

Volume fraction of filler and matrix was calculated according to the equation 18

$$V_f = \frac{W_f}{\left[W_f + (1 - W_f) \left(\frac{\rho_f}{\rho_m} \right) \right]} \quad (18)$$

where, V_f is the volume fraction of particles, W_f is the weight fraction of particles, ρ_f is the density of the particles, and ρ_m is the density of the PHB & PHBHV matrix

As shown in Figure 55, there exists very good relation between the experimental and the microhardness predicted from the ROM, for nanoneedles. Whereas nanospherical loaded matrix shows enhanced increase in hardness values and will not fit to theoretical data. This can be attributed to the larger size of spherical particles compared to nanoneedles. Though, both the HA particles are in nano range, but spherical particles are 150-200 nm in diameter, while nanorods are 18-30 nm thick. Another factor which affects the hardness values is the size distribution of spherical nanoparticles. These particles shows bimodal size distribution, where many different sizes with varying proportions are present. Hence the amount of filler per unit volume may be similar to that of needles or even more. These particles due to larger area and volume can act as surface coating on polymer matrix and can partially prevent direct contact of matrix. Due to this, hard HA spherical particles are pressed into the comparatively soft polymer matrix rather than being plastically deformed and thereby recording higher hardness. In case of HA needles, which are smaller in size, have defined interparticle distance and under load will be plastically deformed along with the matrix. It is worth noting that maximum packing of the particles varies with the size distribution and shape of the particles.

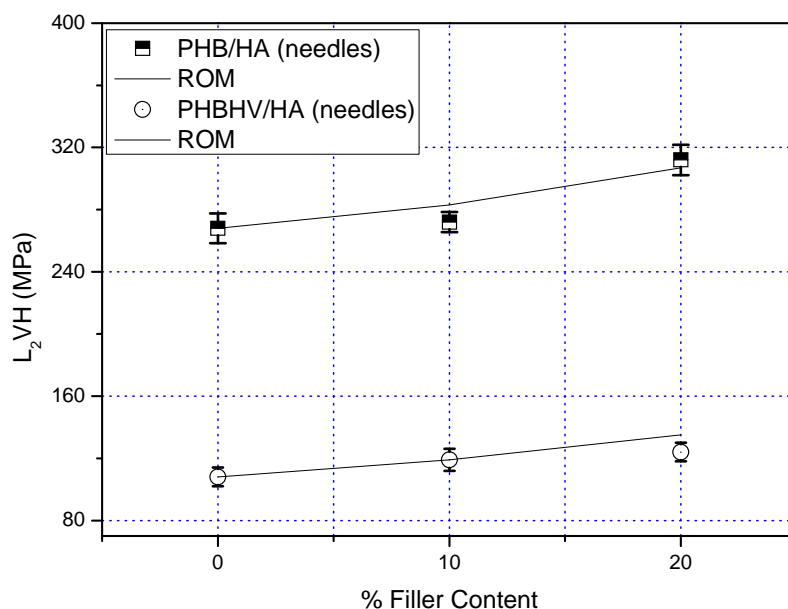


Figure 55: Microhardness as a function of filler content. Correlation of experimental microhardness with composite rule of mixtures (ROM)

Microhardness of composites was measured for both solution cast and melt pressed samples. As casted films had lower hardness compared to melt pressed films. Figure 56 show microhardness of PHB/HA composites with two different PHBs varying in molecular weight and producer.

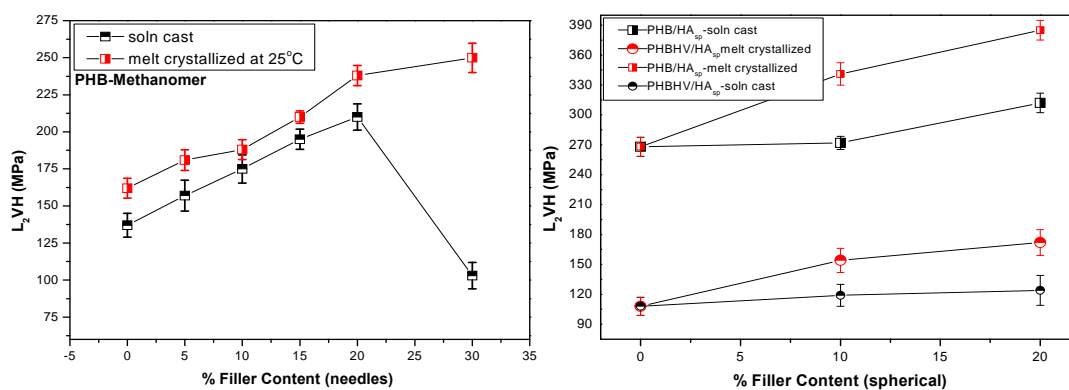


Figure 56: Microhardness as a function of filler content. a) Comparison of microhardness of solution cast and melt pressed PHB and PHBHV nanocomposites.

Nanocomposites of PHB/HA_n from methanomer showed increase in microhardness with increase in volume content of filler. Nevertheless, solution casted films showed a slight decrease in hardness values for solution cast and melt pressed films. Solution casted pure PHB had hardness around 135 MPa and that of melt pressed pure PHB had hardness around

165 MPa. In case of PHB/HA sp, a PHB from Sigma Aldrich showed drastic change in hardness values from those of melt pressed and solution casted films. Hardness is purely dependent on surface topography and crystal structure as mentioned earlier. It was also observed that, the surface morphology of solution cast films had rougher morphology and there were some micropores generated due to solvent evaporation. These pores in turn acted as a weak point and the resistance to indentation decreased, resulting in lower hardness.

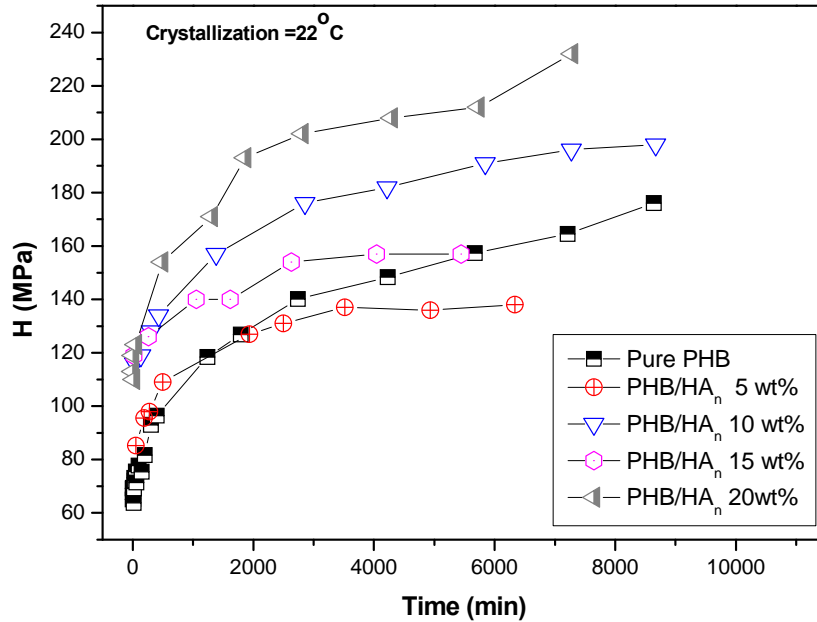


Figure 57: Dependence of microhardness H as a function of crystallization time for PHB/HA nanoneedles filled with different wt%.

4.8 Contact Angle

Cell interactions on the surface of a substrate are solely dependent on the surface characteristics of the composite film. Studies on contact angle revealed an interesting modification of nanocomposite surface with addition of fillers. These studies determine the contact angle of PHB, PHBHV and their nanocomposites with different filler size and ratios. Static angle measurement was performed on both the surface of films, one which is exposed to air(rough texture) and the other which is intact to glass surface (glossy texture) while casting. The roughness of the films, are influenced by the interfacial tensions according to Young equation, but also by many other factors, such as surface roughness chemical heterogeneity, adsorbed layers, molecular orientation, swelling and partial solution of constituents in the material.

Static advancing contact angle of water on various films are summarised below. As expected, contact angle of pure PHB showed 88° , because of its hydrophobic nature (Figure 58). With the addition of 10 wt% needle shaped filler, the contact angle value decreased to 68° . This was due to hydrophilicity of added filler and the value even decreased when 20 wt% filler was added. It is expected that the surface characteristics of the polymer film was modified by the addition of filler. This may not show linear trend with higher filler loading due to surface effects, which are influenced by nanofiller aggregations. Similarly, addition of nanospherical particles showed the same trend, but the contact angle dropped slightly compared to nanoneedles shaped fillers. It may be expected that the larger sized filler particles may decrease the water contact angle by solely contributing to the angle.

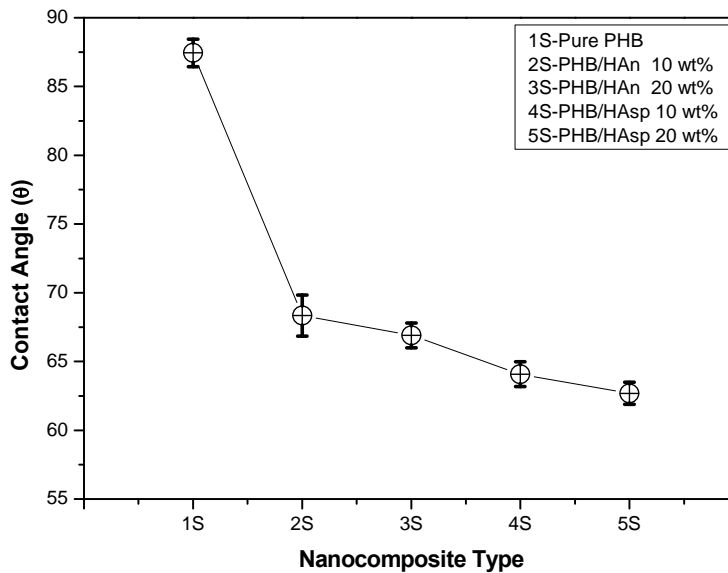


Figure 58: Dependence of contact angle (θ) for PHB/HA filled nanocomposites.

Contact angle of composites films of PHBHV copolymer showed somewhat different trend. As expected, pure PHBHV measured contact angle of 76° . This was comparatively less than the pure PHB, which was 88° . The reason of change in contact angle values may be due to surface of casted films. On the other hand, spherical filler showed slight increase in contact angle values when compared to needle shaped fillers.

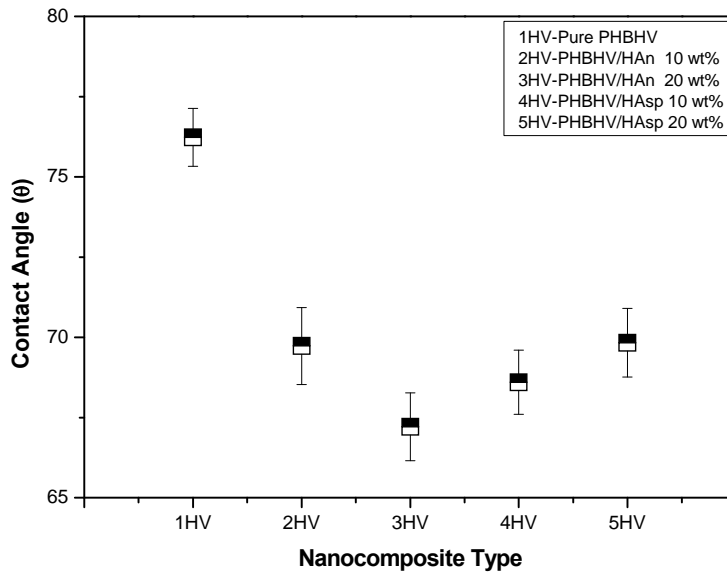


Figure 59: Dependence of contact angle (θ) for PHBHV/HA filled nanocomposites.

The surface tension is calculated via Neumann iteration for the contact angles. PHB has the lowest surface tension with a 30.82 mN/m value, whereas PHBHV had 37.84 mN/m. All the other filled systems which varying filler content and filler size ranged from 40-46 mN/m.

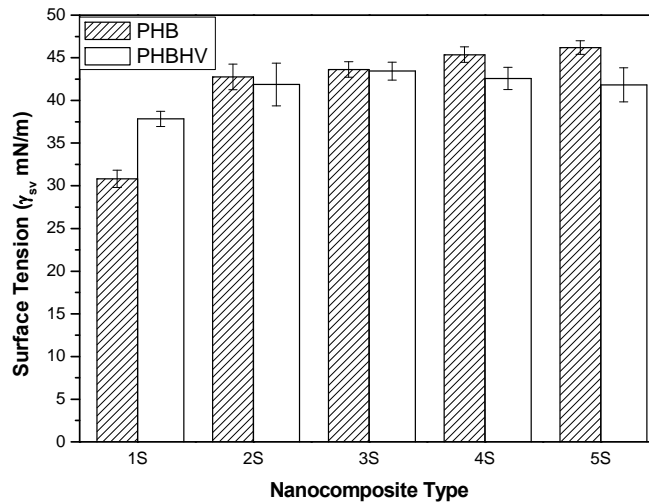


Figure 58: Dependence of surface tension for PHB/HA and PHBHV/HA filled nanocomposites.

As discussed earlier, contact angle is dependent on surface roughness of the substrate. Film surface which were intact to glass plates had finer texture, whereas film surface which were exposed to air had rougher texture. Contact angle values of both the surfaces are shown in figure 58. From the graph it can be clearly noticed that, the surface morphology of films

influenced the CA values. CA values on the rough surface very similar to that of the pure PHB films. The angles made by drop were dominated solely by the hydrophobic polymer and not by the hydrophilic filler. It may be expected that, during solution casting, the evaporation time of solvent in solution is greater than the settling time of fillers beneath the thin layer of polymer. Also due to density difference, all the fillers dispersed will settle towards the glass plate leaving behind polymer on the exposed surface. Because of this CA values of filled systems are more or less similar to pure PHB.

4.9 Cell Culture

Morphology of MG-63 cells were analyzed on PHB/HA (nanoneedles) and PHB/HA (nanospheres) nanocomposite films.

4.9.1 Cell adhesion and morphology of MG-63 cells

The morphology of MG63 cells cultured on PHB and PHB/HA nanocomposite films with different filler content and varying filler size was determined by phase-contrast microscopy after 2hr, 1, 3 and 7 days. Figure 59-63 shows the morphology of the cells which is attached to and proliferated on the TCP used as a control surface, and b,c,d,e and f are different samples which are summarized in the figure. Since Figure 59 shows only the representative morphology of the cells from each culture, the cell density depicted should not be considered as indicative of the actual cell numbers. After 2 hr of cultivation, the cells on the TCP control had mixed morphology exhibiting both spherical and spread shapes. In case of PHB and composite films, all the cells showed spherical morphology. Following the initial stage of cell attachment, the morphology of cells on the samples changed from a spherical to an irregular shape characterized by cytoplasmic and dendritic extensions, i.e., lamellipodia and filopodia. However, it was noticed that at day 1 the cell morphology for 20 wt% filled nanocomposites of both the sizes showed flattened shape compared to pure PHB and 10 wt% nanocomposites. Nevertheless, it was observed that the cells on TCP exhibited a more flattened spindle shape.. On day 3, the cells on all samples had proliferated to some extent with TCP showing higher tendency of proliferation. Even on the third days, the cell morphology for nanocomposites were irregular. The cells attained confluence on the TCP and nanocomposite films at day 7. However, it is notable that the morphology of the cells on the TCP and nanocomposite films was clearly different on TCP, the cells exhibited a flat spindle shape and were aligned in a distinct orientation. In contrast, the cells on films exhibited a variety of shapes without any clear orientation.

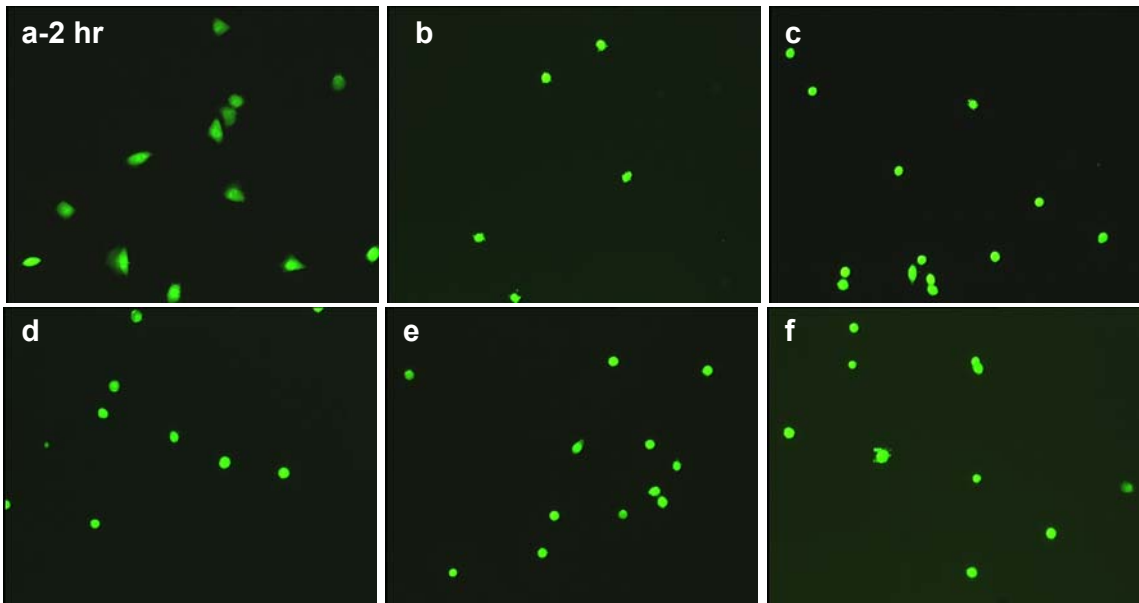


Figure 59: Cell morphology at 2 hrs of cell seeding. a) Tissue culture Polystyrene (TCP), b) pure PHB (biomer), c) PHB/HA n 10wt%, d) PHB/HA n 20 wt%, e) PHB/HA sp 10 wt% and f) PHB/HA sp 20 wt%. Films are stained with FDA (Fluorescein diacetate)

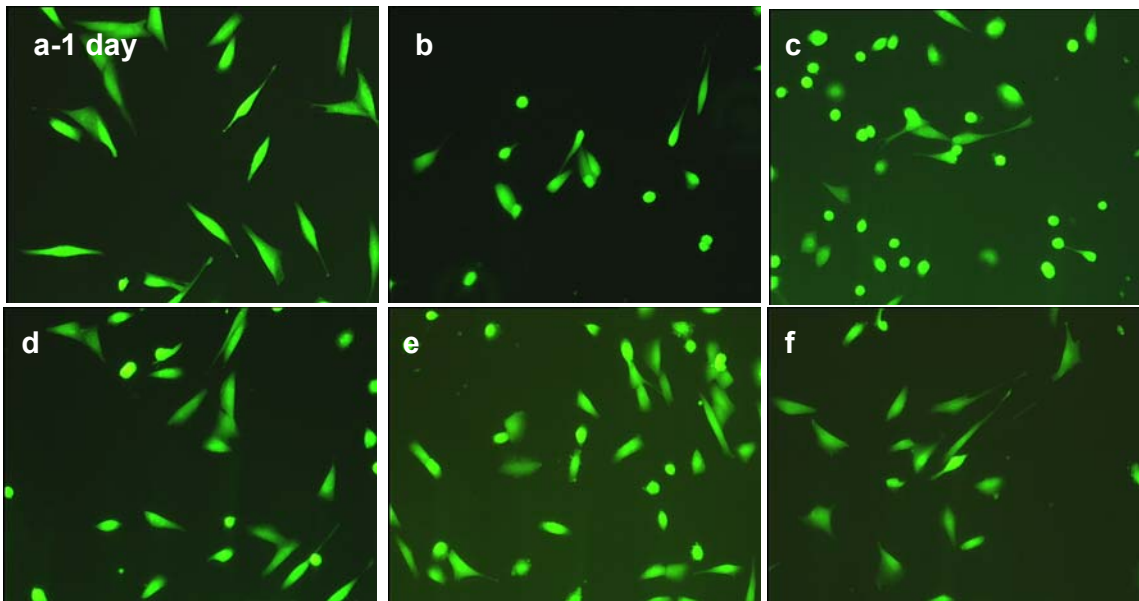


Figure 60: Cell morphology on day 1 of cell seeding. a) Tissue culture Polystyrene (TCP), b) pure PHB (biomer), c) PHB/HA n 10wt%, d) PHB/HA n 20 wt%, e) PHB/HA sp 10 wt% and f) PHB/HA sp 20 wt%. Films are stained with FDA (Fluorescein diacetate)

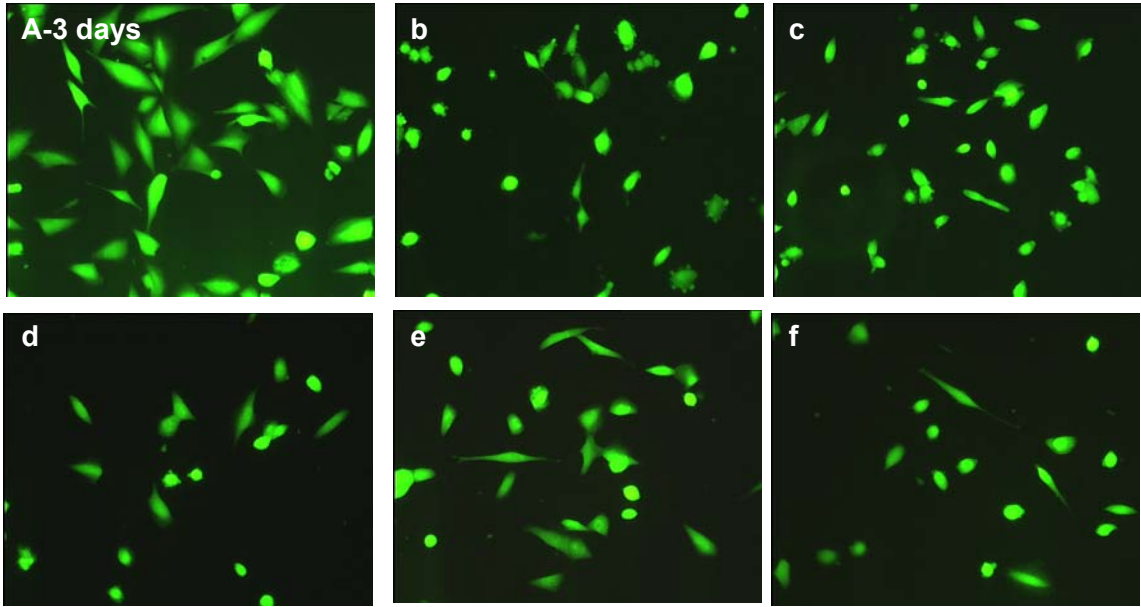


Figure 61: Cell morphology on day 3 of cell seeding. a) Tissue culture Polystyrene (TCP), b) pure PHB (biomer), c) PHB/HA n 10wt%, d) PHB/HA n 20 wt%, e) PHB/HA sp 10 wt% and f) PHB/HA sp 20 wt%. Films are stained with FDA (Fluorescein diacetate)

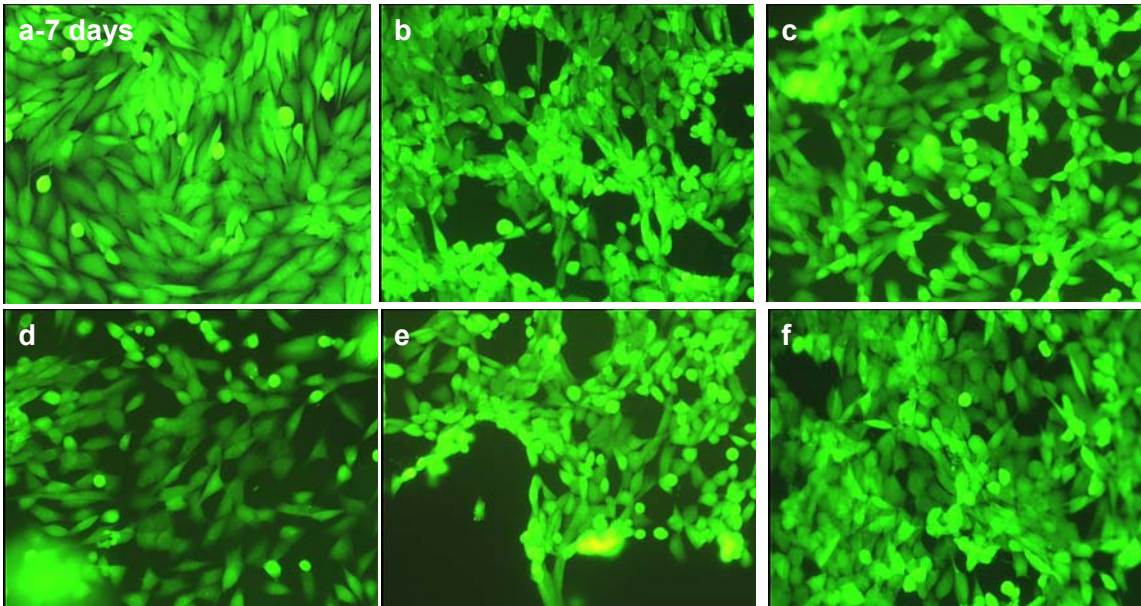


Figure 62: Cell morphology on day 7 of cell seeding. a) Tissue culture Polystyrene (TCP), b) pure PHB (biomer), c) PHB/HA n 10wt%, d) PHB/HA n 20 wt%, e) PHB/HA sp 10 wt% and f) PHB/HA sp 20 wt%. Films are stained with FDA (Fluorescein diacetate)

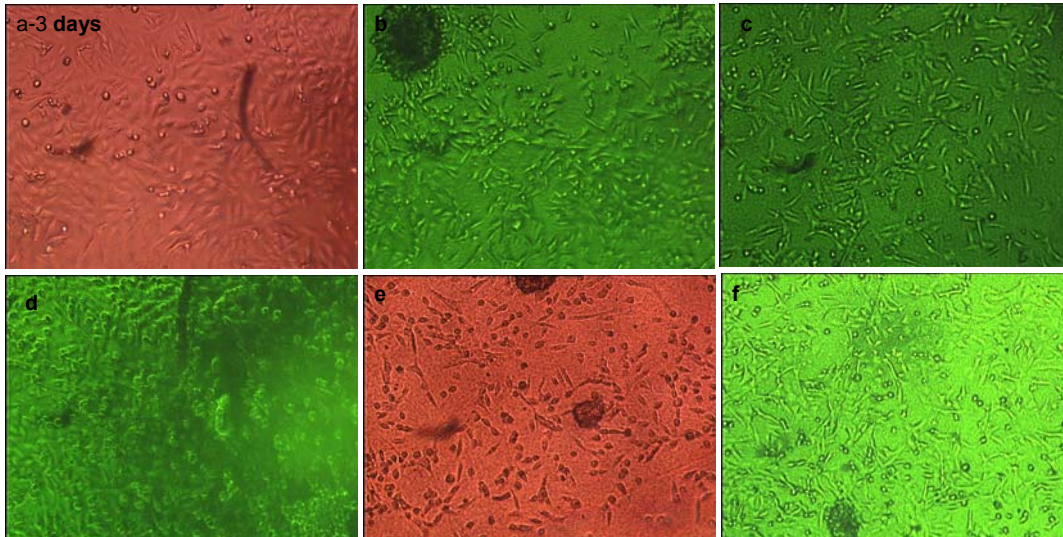


Figure 63: Cell morphology at 3 days of cell seeding. a) Tissue culture Polystyrene (TCP), b) pure PHB (sigma), c) PHB/HA n 10wt%, d) PHB/HA n 20 wt%, e) PHB/HA sp 10 wt% and f) PHB/HA sp 20 wt%. Films are stained with FDA (Fluorescein diacetate)

4.9.2 Evaluation of Cell Proliferation

The viability of MG-63 cells cultured on polystyrene control and PHB (Biomer) nanocomposites are shown in figure 64. The measured fluorescence intensity (FI) is correlated to the metabolic activity of viable cells. Higher metabolic activity gives rise to high FI and is thus indicative of the higher cell viability. Over the culture period, cell viability on polystyrene control was significantly higher than cell viability of PHB nanocomposites on day 1 and 3. Nevertheless there was some decrease in viable cells on the 3 days culture in nanocomposites for which the reason is still yet to be analyzed. But on the seventh day the cell viability of all the samples were even higher than TCP. This confirms that the surface of the samples does not facilitate the cells to attach and proliferate more readily. But what is observed here is that the filled systems especially one with 20 wt% nanoneedles and 20 wt% nanospheres, we can see increased FI on the 7 day. This is attributed to the HA filler which promote cell proliferation.

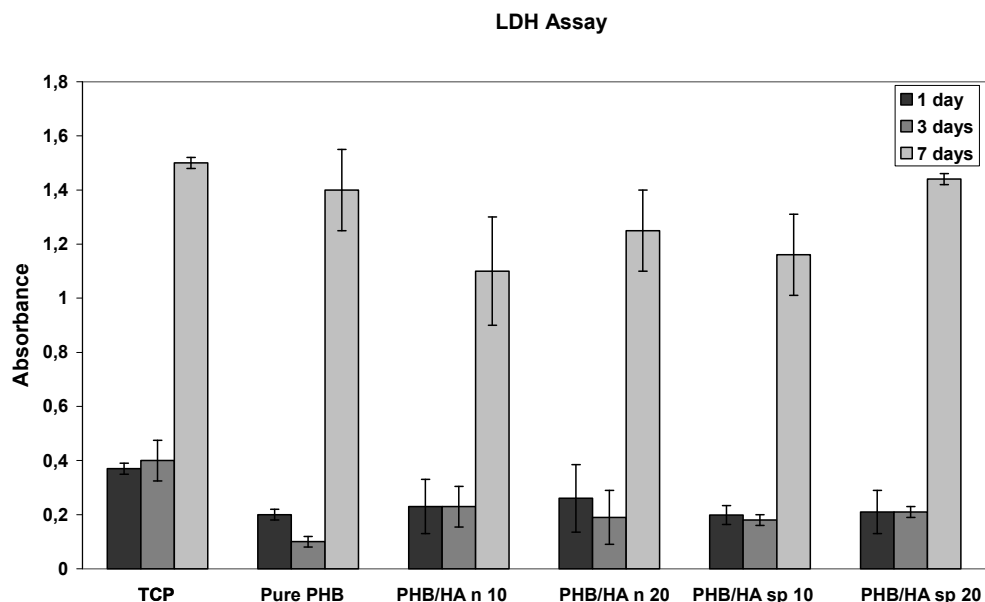


Figure 64: Proliferation of MG-63 cells cultured on TCP (control), Pure PHB & PHB/HA (10 & 20 wt%, needle & spherical filled) samples investigated after 1, 3 and 7 days of cultivation via LDH assay. The absorbance was read at 492 nm. The data presented represent the mean \pm SD.

However, addition of HA increased cellular activity compared to pure polymer, but there was drastic decrease in cellular activity and cell morphology, when compared to that of polystyrene controls. Hence, it could be concluded here that the decrease in cell activity is not from the toxicity of the substrates, but from the surface roughness of the substrates. Morphology of cells as well as cellular activity is directly dependent on the surface texture. Some studies have investigated that surface roughness favored cell adhesion and shown better attachment of cells on rough surface, however surface morphology did not affect cell spreading. Though it must be noted that cell proliferation, differentiation and matrix calcification is as important as cell adhesion. These results shows that surface roughness has a major affect on cells, and that many aspects of cellular activity, including cell morphology, are affected in a surface-specific manner. These results are also in consistence with the results obtained by Bower and Martin et al.

The effect of the surface roughness on the cell growth was also confirmed by fluorescence microscopic observations of the live and dead cells cultured on the roughest and smoothest substrates. Here smooth surface is compared for polystyrene controls and rough surfaces for nanocomposite films.

The morphologies of the attached MG-63 cells at day 1 after plating on the substrates were observed by fluorescence microscopy. Representative pictures are shown in Figure 59-63 for 1, 3 and 7 days which to discern the substrate-dependent differences in their cell

morphologies. Whereas cells on the smoothest substrate (control) exhibited a high degree of spreading and showed a highly flattened morphology (Figure. 63), those on the roughest, of which the surface is highly rugged and irregular, had a round shape. Even though there was confluent monolayer observed on the 7th day of culture, the shape of cells didn't change on nanocomposite films. These results were also consistent with the results on epithelial cells, fibroblasts, and bone cells which were reported to use the topography of the substrates for orientation and migration, a process known as contact guidance. The endothelial cells attached on the planar substrates micropatterned with adhesive and nonadhesive regions which were shown to take on the size and shape of the underlying adhesive island. Miura et al. reported that the cells attached on a closely packed particle monolayer showed a stretched narrow stalk-like shape and the cell growth was suppressed compared with a flat surface. They concluded that cell extension and shape could be related to the cell growth and the pitch is a key factor for determining later fate of the cells.

Number of cells attached on the substrates at day 1 was evaluated by measuring the L-lactate dehydrogenase (LDH) activity of the cell lysate (Figure 64). It was found that the absorbance values of nanocomposite films were far less compared to controls. The reason for this decreased activity is due to the surface roughness, which was also observed by SEM which depicted that, solution cast nanocomposite films when casted on a glass plate, the upper surface exposed to air had a rugged surface and also there were micro pits on the surface due to solvent evaporation. Contact angle of HA filled composites showed that rougher surface was hydrophobic. After 7 days of culture, absorbance as measured by LDH assay conformed that both control and substrates showed similar values. Nevertheless the morphology of cells was completely different with controls and substrates and on the other hand, the number of cells on the roughest substrate was much lower. These results indicate that the difference in the cell number after the 7-day culture resulted either not from the initial cell number differences or from cell death, but from inhibited proliferation by the surface roughness.

ALP is a representative enzyme of osteoblastic differentiation, and the ALP activity was determined as an indicator of osteoblastic differentiation in the MG-63 cells. A different ALP activity was found depending on the surface roughness and on the duration of the culture (data not shown). The ALP activities were measured on 1,3 and 7 days and maximum was observed on 7th day. As shown in Figure 65, the ALP activities of cells on the rougher substrates were much less than of those on the smoother substrates. This tendency of the ALP activity was consistent with all the filled systems. Though it was not able to differentiate the roughness degree between filled systems and also roughness values of the surfaces. However

these results indicate that osteoblasts cultured on smooth surfaces maintain their ability to express ALP, while a rough surface seems to significantly reduce it, clearly indicate that cell morphology is significantly influenced by the degree of cell spreading which is governed by its 2-D or 3-D surface geometry of a substrate. Therefore, the round cell morphology and decreased proliferation observed on the rough-surfaced substrates in this study could be similarly explained with geometrical restriction of cell spreading caused by 2-D surface of the substrates.

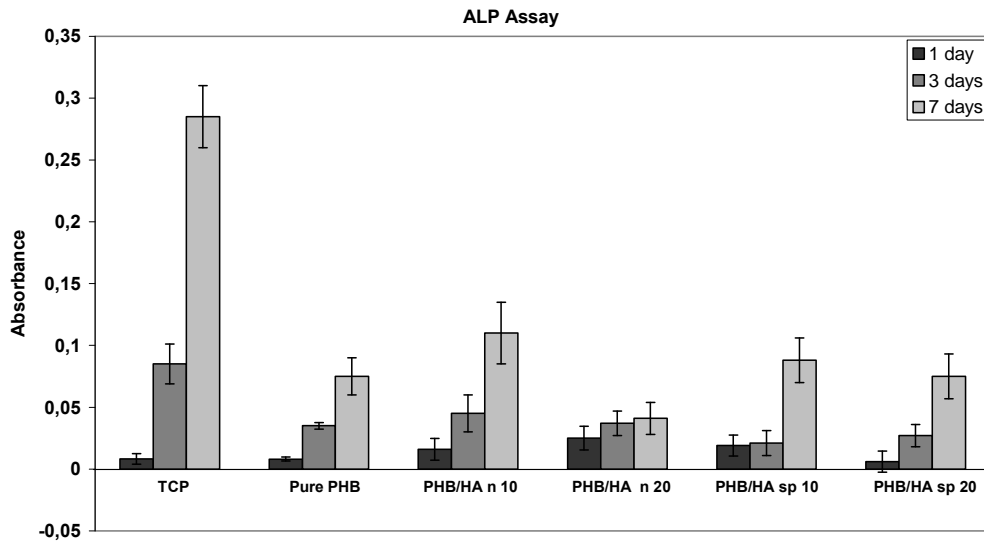


Figure 65: ALP activity of MG63 cells cultured on TCP (control), Pure PHB & PHB/HA (10 & 20 wt%, needle & spherical filled) samples investigated after 1, 3 and 7 days of cultivation via ALP assay. The absorbance was read at 405 nm. The data presented represent the mean \pm SD

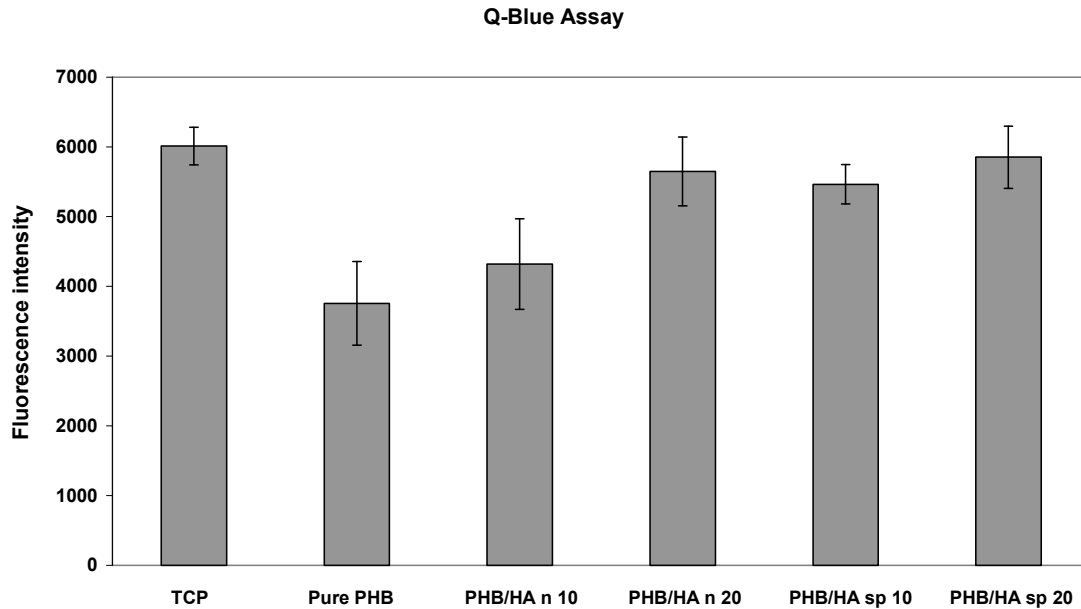


Figure 66: Viability of MG63 cells cultured on TCP (control), Pure PHB & PHB/HA (10 & 20 wt%, needle & spherical filled) samples investigated after 1, 3 and 7 days of cultivation via ALP assay. The fluorescence intensity was measured at 544 nm. The data presented represent the mean \pm SD.

4.9.3 Cell adhesion and morphology of primary osteoblast cells

Cell morphology on substrates prepared using PHB and PHB/HA varying in filler content as well as filler shape demonstrated increase in number of viable primary osteoblast cells as observed using ESEM. Figure 67 is a ESEM image of pure PHB and nanocomposite substrates filled with needle shaped particles on which osteoblasts cells were cultured.

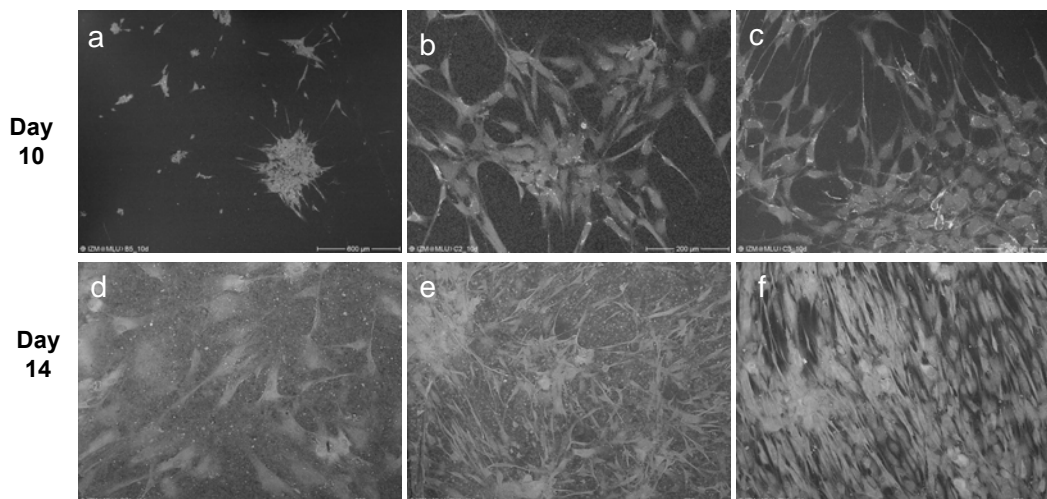


Figure 67: Primary osteoblasts cultured on PHB/HA substrates. Cell morphology on day 10 and 14 imaged using ESEM. a) & d) pure PHB (methanomer), b) & e) PHB/HA n 10wt%, c) & f) PHB/HA n 20wt%

As compared to pure PHB which is shown in Figure 67a, all the other images shows cell behaviour on nanocomposite films with increase in filler content. It was observed that cell growth on nanocomposite substrate was better than that of pure PHB substrate except for the 30% filler loading which is shown in figure 67f. This may be attributed to the uneven dispersion of the filler in the matrix. It was also noticed that, there was preferential anchorage of cells to HA by the cell filopodia. Cells were also seen to anchor to surrounding cells in preference to the PHB substrates. As expected, there was normal, flattened osteoblast morphology on all the samples. Also at higher filler loading, the cells showed elongated morphology which may have occurred due to the stretching filopodia, in the quest of establishing contact with the surrounding cells. However, compared to the control, nanocomposite substrates showed substantial increase in number of cells. This was also evidenced in earlier reports, where HA blending into biomaterials increased positive cell response. Studies have also found that a synergy among increasing focal contact formation, cytoskeleton organization, cell proliferation and expression of phenotype was observed with increasing HA content in poly (methylmethacrylate) [95, 189] . Others suggested that HA coatings on TiO₂ resulted in increasing bioactivity owing to the presence of hydroxyl groups detected on their surface which promoted the calcium and phosphate precipitation, and thus improved the interactions with osteoblast cells. This was also evident in the present study where the contact angle values decreased for nanocomposites suggesting higher hydrophilicity induced by the filler component.

Studies have also focussed on the effect of surface roughness on cell adhesion behaviour. Surface of the nanocomposites from our fabrication technique resulted in an appropriate surface roughness as evidenced by SEM images (which is not shown here). This had a positive effect on surface biocompatibility as osteoblasts preferred appropriate surface roughness.

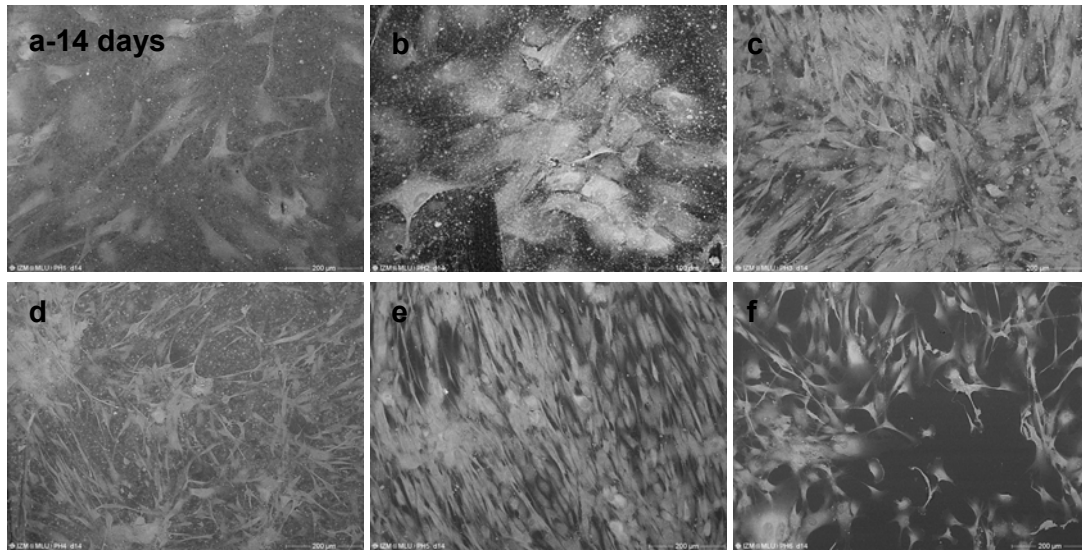


Figure 68: Primary osteoblasts cultured on PHB/HA substrates. Cell morphology on day 10 and 14 imaged using ESEM. a) pure PHB (methanomer), b) PHB/HA n 5wt%, c) PHB/HA n 10wt%, d) PHB/HA n 15 wt%, e) PHB/HA n 20 wt% and f) PHB/HA n 30 wt%.

Crystallinity of PHB may also have an effect on exposure of HA particles on surface. When chloroform evaporated during scaffold fabrication, PHB polymer chains undertook a rearrangement. After blending with HA, PHB with higher crystallinity may exclude more HA on surface compared with the unfilled PHB. This was proven by surface examination (AFM) of different PHB and PHB/HA films with both the filler types. As needle shaped fillers were oriented along the direction of lamellae, they tend to occupy the interlamellar space, whereas the fillers which were arranged perpendicular to the lamellae were excluded. In the case of spherical particles, which were larger in size than the interlamellar spacing, were excluded. Some of them even distorted the lamellar arrangement. Nevertheless we didn't notice any drastic change in viability with both the filler types. As exposed HA particles should be favourable for focal contact formation of osteoblasts, this may be the reason why blending of HA into PHB has better effect on promoting osteoblast growth than that into pure PHB. Also the effect of filler shape on osteoblast attachment was studied by using needle and spherical

shaped particles. Figure 69 shows the ESEM image of attached cells on PHB/HA n and PHB/HA sp nanocomposite substrates. Accordingly, both the substrates showed well dispersed cells on to the substrates and there was no drastic change observed. Nevertheless, quantitative cell assays may be helpful in determining the actual difference in the number of cells attached to the substrates. This will be dealt in detail in future studies.

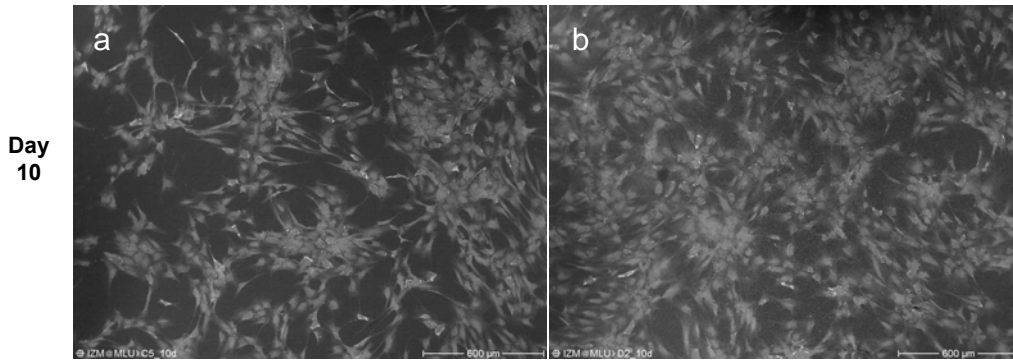


Figure 69: Primary osteoblasts cultured on PHB/HA substrates. Cell morphology on day 10 imaged using ESEM. a) PHB/HA n 10wt% and b) PHB/HA sp 10 wt%

4.9.4 Immunohistology of primary osteoblasts

Primary osteoblasts cells cultured at confluence exhibited a strong intracellular cytoplasmic labeling for collagen Type I, as revealed by immunocytochemistry. Both cells cultured on pure PHB and PHB/HA (Figure 70) showed a positive immunofluorescent staining for collagen Type I.

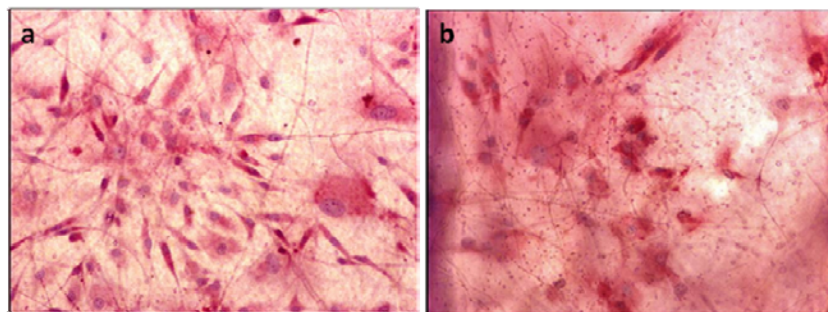


Figure 70: Histological aspect of the extracellular matrix formed by human osteoblastic cells cultured on PHB/HA substrate on 14 days of culture. a) PHB/HA n 10wt% and b) PHB/HA n 20 wt%.

Histologic evaluation showed that the matrix synthesized by primary osteoblasts cells on the substrates after 2 weeks of culture was composed of thick layers of collagenous matrix. Some nodular structures were also found with numerous osteocytic cells embedded into the matrix. It was also found that, with increase in content of hydroxyapatite, these thick nodules increased showing the positive effect of HA on collagen synthesis.

4.10 Porous Scaffolds

4.10.1 Morphology of porous scaffolds by immersion precipitation

Morphology of porous scaffolds was observed from scanning electron microscopy. Figure 71 (a and b) is a porous film prepared by dilute PHB-chloroform solution mixture (96:4). Ethanol was used as nonsolvent for pore generation by solvent exchange. Using ethanol as nonsolvent, a uniform pores with cellular structure was obtained. With the immersion bath composition of 100:0 and 96:4 (chloroform:ethanol) ratios, we could observe very fine cellular pores. As the immersion bath composition changed to higher nonsolvent ratios, similar cellular structures were observed, but with increasing cell size varying from 8-10 μm . When the concentration of casting solution was increased from 90:10 and 80:20, we could observe much different morphology. The cellular architecture was changed into random pores with variation in pore size. Also the pore size decreased drastically. This phenomenon was also observed for 80:20 casting solutions. Only difference with these two concentrations is their ability to solvent nonsolvent exchange. As the concentration of casting solution was increased, the pores transformed from cellular to interconnected porous morphology. The formation of porous cellular structures has often been assigned to liquid-liquid demixing. However, PHB being crystallizable polymer, solid-liquid demixing can also play important role in structure formation. Both liquid-liquid and solid-liquid demixing are probably competing in the formation of PHB films.

Pore formation can be explained by considering a fact that, when a semicrystalline polymer is treated with a solvent, its surface region can be viewed as a concentrated polymer solution, containing dissolved polymer molecules as some well as disentangled molecules attached to the surface. If subsequently the good solvent is replaced with a poor solvent, the disentangled polymer chains will associate with each other rather than with the nonsolvent molecules. If the replacement of the solvent containing some dissolved polymer molecules by the nonsolvent is slow, the disentangled chains of the attached polymers have time to associate in the most compact form, thus generating a smooth surface. If the replacement is rapid, the chains will associate in a loose fashion, thus generating a porous interfacial region. The solvent containing dissolved polymer chains is extracted into the nonsolvent during this process. The rapid replacement of chloroform with the nonsolvent forces the surface molecular chains to entangle again. This reentanglement being rapid generates a surface whose morphology is different from that of the untreated surface. The pore size of the porous surface is in the range from micron to submicrons.

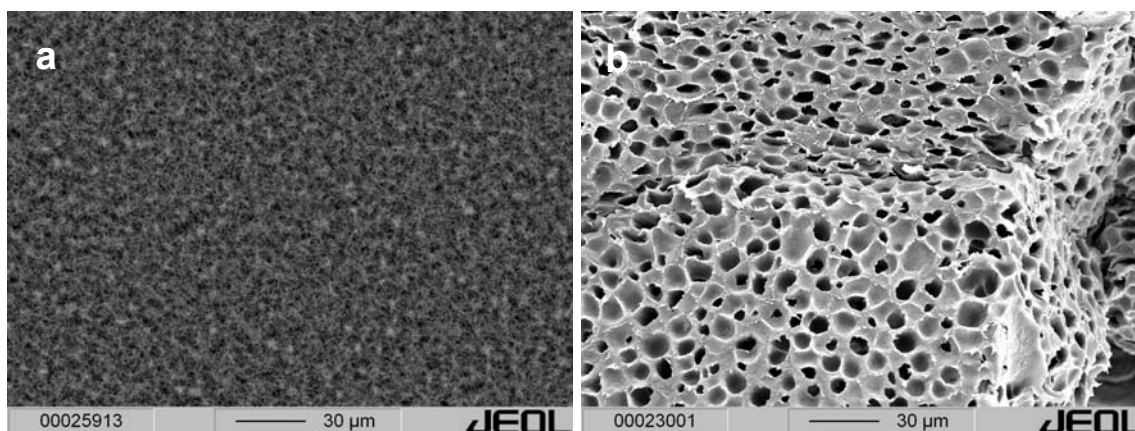


Figure 71: Scanning electron micrographs of films prepared from (by weight) 96:4 CHCl_3 -PHB solutions by immersion precipitation a) 90:10 and b) 70:30 (ethanol-chloroform immersion bath)

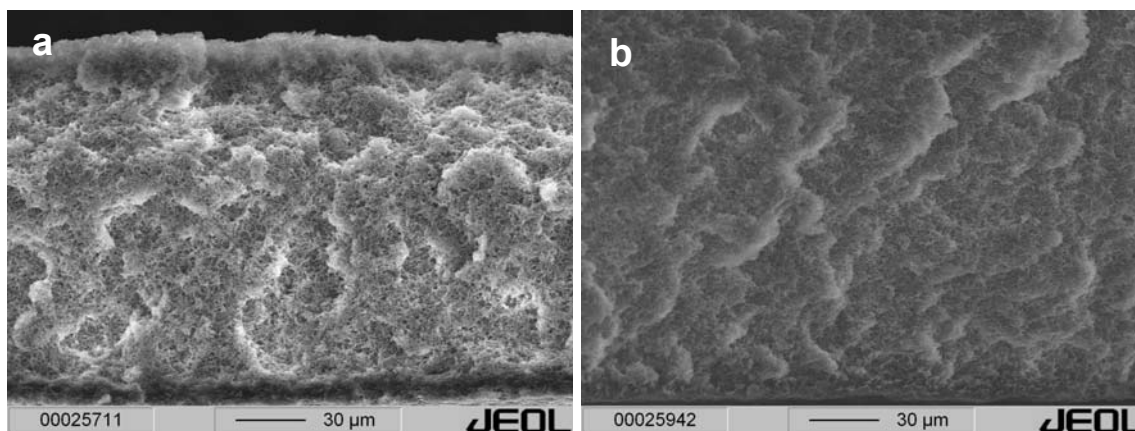


Figure 72: Scanning electron micrographs of films prepared from (by weight) 90:10 CHCl_3 -PHB solutions by immersion precipitation a) 90:10 and b) 70:30 (ethanol-chloroform immersion bath)

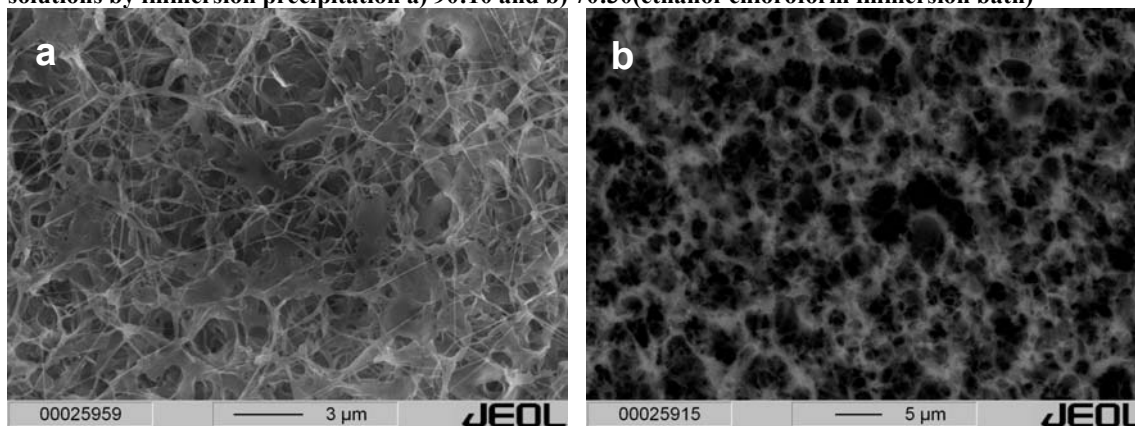


Figure 73: Scanning electron micrographs of films prepared from (by weight) 80:20 CHCl_3 -PHB solutions by immersion precipitation a) 90:10 and b) 70:30 (ethanol-chloroform immersion bath)

The porous cellular morphology as observed in dilute casting solutions can be assigned to liquid-liquid phase separation, which occurs by nucleation and growth of a poor polymer phase, with the fixation and stabilization of the cellular structure occurring by crystallization, in the presence of crystalline polymers. For dilute solutions the morphology formation was

associated with the coalescence phenomena which can take place in systems demixing by spinodal decomposition, leading to a matrix/disperse domain morphology. For concentrated casting solutions, the observed morphology is the result of gradual inversion of the phase separation sequence, with the crystallization process taking place before liquid-liquid demixing.

4.10.2 Morphology of porous structures by freeze drying and particulate leaching

Leachable templates with various shapes and sizes was prepared by fusing the sieved salt particles of determined size range in an (enclosed) atmosphere with a relative humidity (RH) of 75-81% for about 2 days, followed by drying in ambient air. Alternatively, the templates was fabricated by compacting the soaked sugar or salt particles of certain size range in an acetone/ water mixture, as sugar cubes were reported to be prepared by compressing moist sugar particles. When the acetone/water ratio is in the range of 7.5/2.5 to 9/1 (v/v), all prepared templates are stable. The porosities of the resultant templates are close to those prepared by the first.

Polymer structures with very high porosity and interconnectivity was obtained by the combination of freeze drying and particulate leaching method by using prefabricated templates. Many of the parameters will influence the structure formation. Polymer concentration has a major contribution in fixing the pore architecture. Concentrated polymer solutions more than 15-20 wt% will not give good pore interconnectivity. In this method polymer solution was forced into sugar/salt templates which have predesigned pores. This is done by applying very low pressures in the range of 50-100 mbar. As the concentration of polymer solution increases, filling up of pores decreases and there is no further interconnectivity. In figure 74 we can see the modification of pore structures with change in parameters. With decrease in freezing temperature from -25°C to -80°C , there was reduction in pore size. As the specimen geometries are equal and the samples are cooled from room temperature, the higher freezing temperature has the lowest quenching rate. Although further reducing the quenching rate increased the pore size. Also polymer concentration had great influence on pore morphology. For 5 wt% solution concentration there was increase in pore size and this trend decreased after reaching 10 wt%. The increase in pore size was almost 2 folds for 5 wt%. But the overall porosity is not much altered (Table-13). But when we observe the pure homopolymer with that of filled systems, we can see that the overall porosity is decreasing.

Grain size of the particles also influences the pore size. It was observed that bigger grain size particles resulted in larger pores. Two different grain size one which was $>100\ \mu\text{m}$ and one which was $< 100\ \mu\text{m}$ showed different morphology. All the other parameters like fusing solution acetone/water 4.5/0.5 w/w, freeze drying conditions and filler loading are kept constant. Every change in parameter will result in different morphology as this process is very sensitive. The pore sizes are relatively small, with a maximum pore size of approximately $60\ \mu\text{m}$. All scaffolds prepared by freeze-drying and leaching show an irregular porous structure.

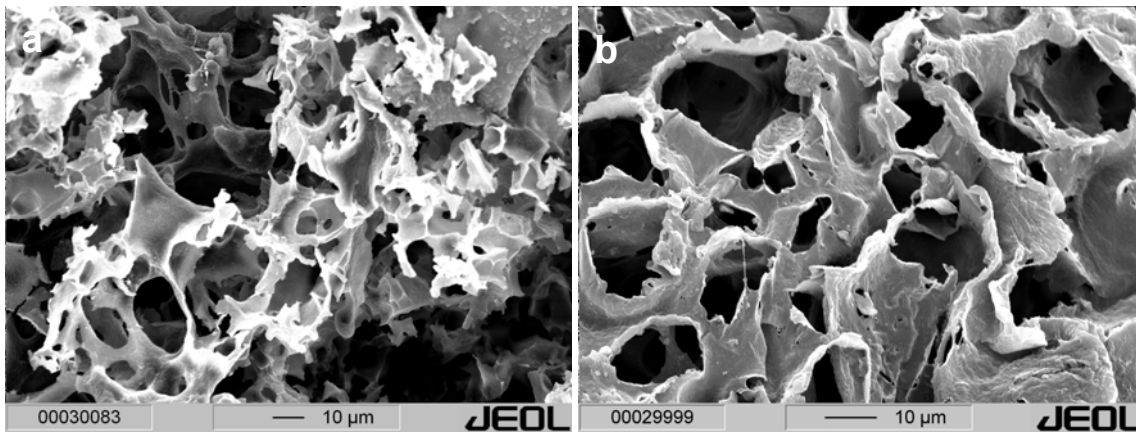


Figure 74: SEM micrographs of PHB/HA porous nanocomposites prepared from freeze-drying and particulate leaching Polymer nanocomposite/chloroform in the presence of predesigned salt template. Larger pores approximately $50\text{-}70\ \mu\text{m}$ results from leaching of salt particles and smaller pores approximately $15\text{-}35\ \mu\text{m}$ results from freeze drying. A) PHB/HA concentration 10 wt%, grain size of salt template $<100\ \mu\text{m}$ and freezing temperature -80°C B) PHB/HA concentration 10wt% and grain size of salt template $>100\ \mu\text{m}$ and freezing temperature -25°C

Porous structures with highly interconnected structures were developed by using commercially available sugar cubes. These structures have porosities over 97%. Figures 75 show that highly interconnected porous structures are obtained with large pore sizes of $300\text{-}400\ \mu\text{m}$. This is because the grain size of particles obtained from commercial sugar cubes was much bigger and they were well bound to each other forming a definite pattern of pores with the bigger diameter. When the polymer was forced inside, they retained the morphology of the pores of the sugar cubes. But with leaching and drying, some of the cubes tend to collapse or fuse. Eventually, size of pores mainly depend on the size of the grains. As compared with fig -2 we can observe the pores with smaller diameter with that of fig-4. Even though all the parameters were kept constant for both of the samples, only grain size was altered. Polymer concentration and freezing temperature only influence to a lesser extent compared to the grain size. The final pore structure of the scaffolds is determined by the size and content of the sugar particles as well as by the solvent-crystal morphology after freezing

of the chloroform solution.

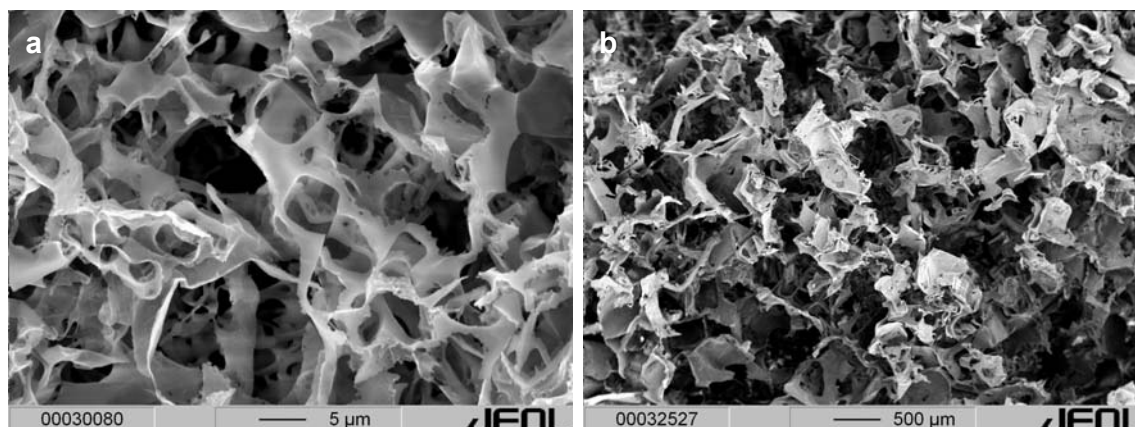


Figure 75: SEM micrographs of PHB/HA porous nanocomposites prepared from freeze-drying and particulate leaching a) Polymer nanocomposite/chloroform in the presence of predefined salt template having pores of about 30-40 μm and b) Porous Pure PHB obtained from commercially available sugar cubes. Pore size greater than 300 μm

Table 13: Porosities of Porous Polymeric nanocomposite Scaffolds Prepared by Freeze-Drying Particulate leaching and melt infiltration techniques.

Polymer	Polymer concentration	Freezing Temperature (oC)	Overall Porosity (%)
	w/v %		
PHB homopolymer	5	-25	99.35
	10	-25	99.1
	5	-80	99.5
	10	-80	99.3
PHB/HA (90/10)	5	-25	98.79
	10	-25	97.89
	5	-80	98.62
	10	-80	97.5
PHB/HA (80/20)	5	-25	97.32
	10	-25	97.2
	5	-80	97.4
	10	-80	97.2
		Melting Temperature (oC)	
PCL homopolymer	10	60	96.4
	10	60	96.1
	10	60	95.3

4.10.3 Morphology of porous structures by melt infiltration technique

Porous structures using melt-infiltration technique show very promising results for PCL scaffolds. Figure 76 shows the porous morphology of PCL scaffolds prepared using sugar templates of different grain size. a) templates of 400 μm and b) templates of 600 μm .Both the

samples show very good interconnectivity with pore diameter larger than 300 μm . With increase in grain size from 400 to 600 μm there is a slight increase in pore diameter. In some of the samples there was blocking of pores on the surface; this may be due to the cooling of polymer melt which is above the surface of the templates. But the fractured surfaces showed very good porous structures. Polymer infiltration was even over the entire substrate. Table 13 shows the overall porosity of PCL homopolymer as well as composites. Concentration of polymer was kept constant 10w/v %. With the increasing in filler content in the polymer solution there was a slight decrease in porosity. This may be due to dispersion of nanofillers in the interstitial space of the sugar templates. Some of the pores showed smaller diameter compared to other, this may be due to the solidification of the melt before entering into the deeper end of the templates. Temperature of the melted polymer is reduced as it enters into the substrate thus resulting in solidification.

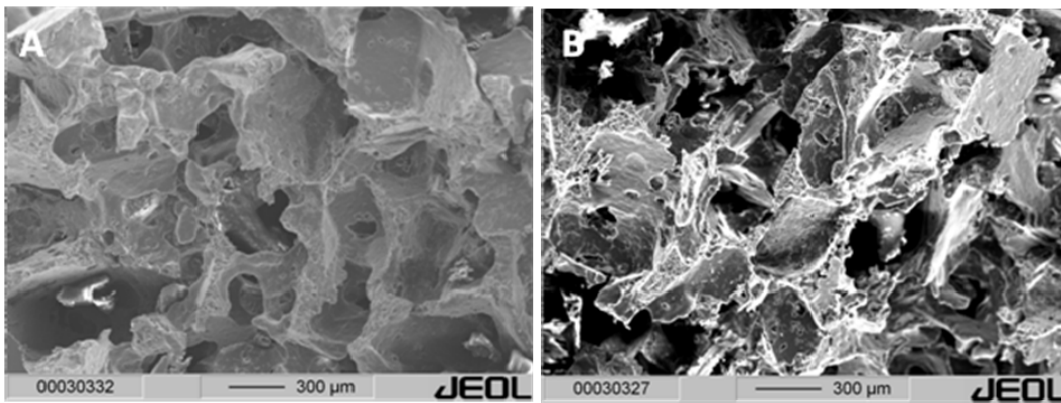


Figure 76: SEM micrographs of porous structures prepared by melt infiltration technique using sugar templates, A) PCL with 400 μm sugar template & B) PCL with 600 μm sugar template

Melt infiltration of PHB was not successful because of the viscosity of melt when heated to its melting temperature. PCL with low molecular weight 2000 g/mol melted and was liquid like at 60 $^{\circ}\text{C}$. So by applying low pressures, all the pores were filled completely.

4.11 Nanofibers

4.11.1 Morphology of nanofibers using conventional electrospinning technique.

The electrospinning process is solely governed by many parameters, classified broadly into solution parameters, process parameters, and ambient parameters. Solution parameters include viscosity, conductivity, molecular weight, and surface tension and process parameters include applied electric field, tip to collector distance and feeding or flow rate. Each of these parameters significantly affect the fiber morphology obtained as a result of electrospinning, and by proper manipulation of these parameters it is possible to get nanofibers of desired morphology and diameters. In the present study, only applied voltage, viscosity, types of solvents mixtures and types of collectors are varied.

In the electrospinning process a crucial element is the applied voltage to the solution. Only after attainment of threshold voltage, fiber formation occurs. This induces the necessary charges on the solution along with electric field and initiates the electrospinning process. It has been already proved experimentally that the shape of the initiating drop changes with spinning conditions (voltage, viscosity, and feed rate) [190]. Researchers have suggested that when higher voltages are applied, there is more polymer ejection and this facilitates the formation of a larger diameter fiber [191].

Table 14: Electrospinning parameters of nanocomposites

No	Composition	Concentration (wt%)	Applied Voltage (kV)	Collector Distance (cm)	Fiber Diameter (nm)
1	PHB	7	12	14	450
2	PHB/HA 10n	10	14	14	700
3	PHB/HA 20n	10	14	14	800
4	PHBHV	8	11	14	300
5	PHBHV/HA 10n	10	14	14	550
6	PHBHV/HA 20n	10	14	14	650

Other authors have reported that an increase in the applied voltage (i.e., by increasing the electric field strength), increases the electrostatic repulsive force on the fluid jet which

ultimately favours the narrowing of fiber diameter. In most cases, a higher voltage causes greater stretching of the solution due to the greater columbic forces in the jet as well as a stronger electric field and these effects lead to reduction in the fiber diameter and also rapid evaporation of solvent from the fibers results. In the present study nanofibers were spun for PHB and PHBHV nanocomposites.

Table 14 shows the optimum values for the nanocomposites nanofibers. Optimum fiber diameters obtained by PHB and PHBHV pure polymers were in the range of 300-450 nm and with the applied voltage of 10-12 kV. As the filler concentration was increased in the matrix, the diameter of the fiber increased. This was due to the reduction in amount of polymer dissolved in the solvent. The solution viscosity has been strongly related to the concentration of the solution and the relationship between the polymer viscosity and/or concentration and fibers obtained from electrospinning has been studied in a number of systems. At very high viscosity polymer solutions usually exhibit longer stress relaxation times, which could prevent the fracturing of the ejected jets during electrospinning. An increase in solution viscosity or concentration gives rise to a more uniform fiber diameter (Figure 77).

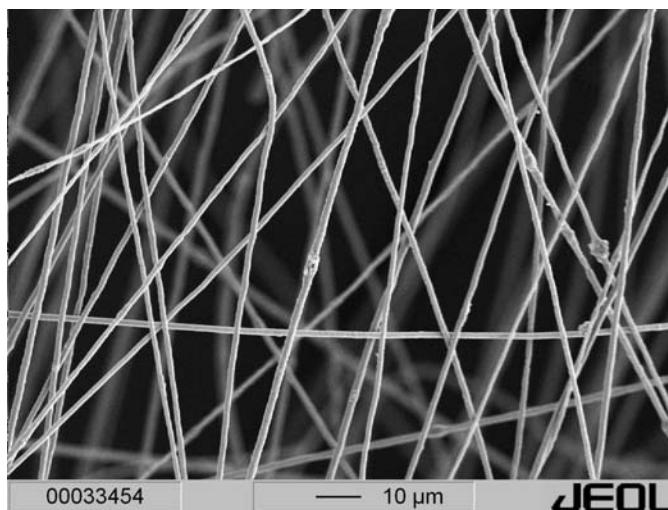


Figure 77: Electrospun PHB at higher solution viscosity demonstrates nanofibers of uniform diameter.

In electrospinning, viscosity of solution plays an important role in determining the range of concentrations from which continuous fibers can be obtained. For solution of low viscosities, surface tension is the dominant factor and just beads or beaded fibers are formed while above a critical concentration, a continuous fibrous structure is obtained and its morphology is affected by the concentration of the solution.

4.11.2 Effect of molecular weight on fiber morphology

The length of the polymer chain is determined by the molecular weight of the polymer, which in turn has an effect on the viscosity of the solution at a given concentration. However, one of the required conditions for electrospinning to form fibers is that the solution must contain a polymer of adequate molecular weight and sufficient viscosity [192]. Generally, when a polymer of higher molecular weight is dissolved in a solvent, its viscosity will be higher than the same polymer of lower molecular weight. This, however, is due to greater entanglement of polymer chain within the solution which is essential to form continuous jet during electrospinning. These polymer chain entanglements determine the stability of the jet and prevent formation of droplets thereby controlling morphology of resultant nanofibers, i.e., formation of beads or smooth fibers.[192] Figure 78 illustrates how the structural morphology of electrospun nanofibers improves with an increase in molecular weight of the polymer.

Morphological examination using SEM revealed two distinctive behaviour in the structural morphology of the nanofiber web as a function of molecular weight. Fibers from 6% aqueous solution of PHB ($M_w=4.4 \times 10^5$ g/mol) indicates fibers with almost spherical beads while those fibers obtained from higher molecular weight PHB ($M_w=1.2 \times 10^6$ g/mol) but of the same concentration shows fibers with less beads but spindle-like beads thus indicating stretching of polymer solution.

Also, more uniform fibers were obtained from 7.5% solution of higher molecular weight PHB ($M_w=9 \times 10^6$ g/mol), whereas still some fibers with beads were attained from 7.5% solution of lower molecular weight PHB ($M_w=4.4 \times 10^5$ g/mol). The results indicate that low-molecular-weight solution tends to form beads rather than fibers and high-molecular-weight solution provides bead-less fibers with larger average diameters.

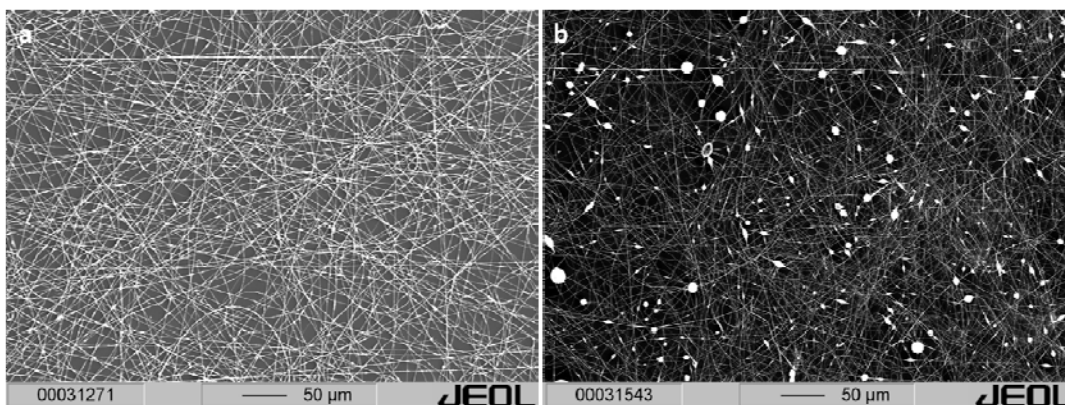


Figure 78: Effect of fiber morphology varying in molecular weight a) PHB methanomer (Mw- 1.6×10^6 g/mol) & b) PHB sigma (Mw- 4.4×10^5 g/mol)

4.11.3 Effect of Solvent on fiber morphology

The solvent used in preparing polymer solutions has a significant influence on its spinnability, because the first and foremost step in the electrospinning process is dissolution of polymer in a suitable solvent. Solvents should have some properties such as, good volatility, vapour pressure, boiling point and should maintain the integrity of the polymer solution. Thus for successful electrospinning the selection of an appropriate solvent system is indispensable. The intermolecular interaction in a polymer–solvent system (binary system) is either attractive or repulsive which depends solely on the type of solvent. In electrospinning, rapid solvent evaporation and phase separation occurs due to jet thinning, solvent vapour pressure plays a critical role in determining the evaporation rate and the drying time. Solvent volatility also plays a significant role in the formation of nanostructures as it influences the phase separation process. The solution viscosity is determined by the concentration of the polymer, but the value of surface tension depends on both the polymer and solvent. By reducing the surface tension of a polymer solution, fibers could be obtained without beads, but this should be applied with caution. It has been recognized that surface tension seems more likely to be a function of solvent compositions, but is negligibly dependent on the polymer concentration.

In this study electrospinning of PHB using chloroform as a solvent resulted in nonuniform fibers with average fiber diameter of about 2-3 μm . In contrast, addition of 1-2 % DMF in polymer/chloroform solution drastically decreased the fiber diameter and also had very good uniformity. Compared to chloroform (Dielectric constant-4.8), DMF has dielectric constant of 38.3. Also another problem encountered in using chloroform as a solvent was its vaporizing rate. This causes clogging of the needle tip which obstructs the continuous fiber formation.

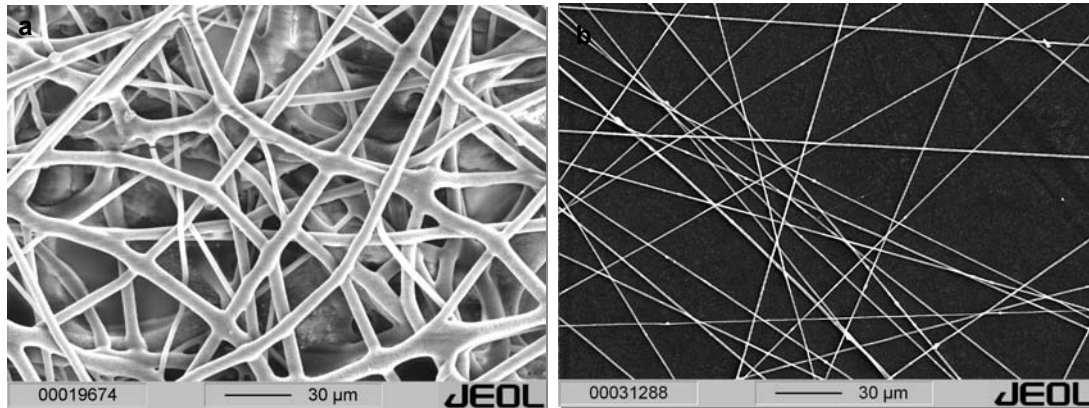


Figure 79: Effect of solvent on fiber morphology a) PHB/HA 10 wt%+Chloroform (7wt%) & b) PHB/HA 10wt%+Chloroform +dimethylformamide (7wt%)

4.11.4 Dispersion of nanoparticles in nanofiber nanocomposites

Nanoparticles of HA in polymer matrix is dispersed more efficiently than in any other nanofabrication technique. TEM investigation of nanofiber reinforced nanoparticles revealed an interesting behaviour on the dispersion of nanoparticles in nanofibers. It was observed that at 10 wt% filler loading, there was uniform dispersion on HA for both the types of fillers. With the addition 20 wt% filler, there was slight agglomeration. Also the fiber diameter changed for spherical filler particles. Nanofibers reinforced with needle shaped particles had the fiber diameter in the range of 200-350 nm, whereas for spherical HA particles, the diameter increased to 400-650nm. This was mainly due to larger diameter of fillers. Nanoparticles were found to orient longitudinally in the spinning direction.

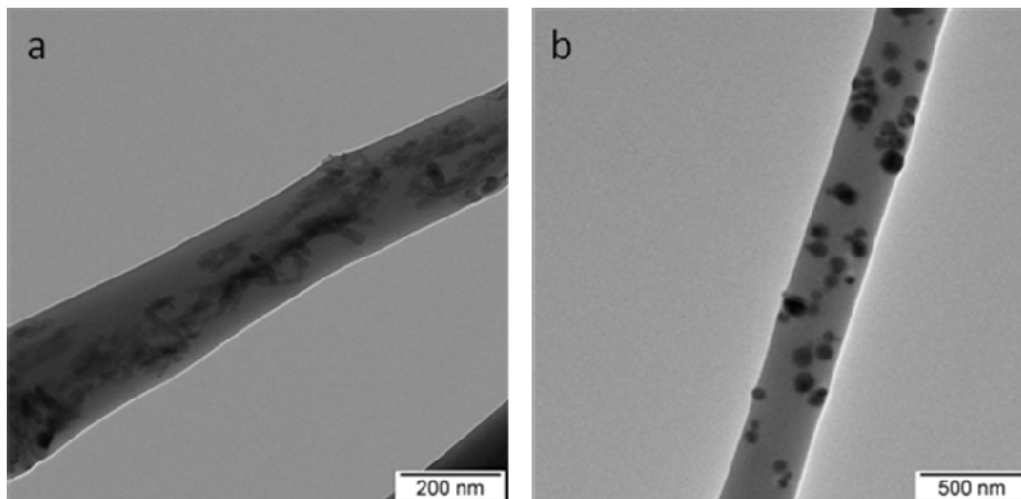


Figure 80: TEM image of nanofiber nanocomposites. a) Nanofiber nanocomposite of PHB/HA needle 10wt% with an optimum fiber diameter of 250nm & b) Nanofiber nanocomposite of PHB/HA spherical 10wt% with an optimum fiber diameter of 450nm

5. Summary

1. Morphology of nanocomposites of PHB and HA (particulate filler) yielded an optimum morphology, where uniform dispersion of filler particles in polymer matrix was achieved. Using ultrasonication as a dispersing technique, the extent of dispersion was least affected by increasing the amount of filler content. It was also established that an optimum dispersion time, temperature and dispersion medium resulted in homogeneously dispersed filler phase without much agglomeration.
2. Morphological investigations on melt crystallized PHB showed very large spherulitic superstructures in the order of $10\mu\text{m}$ - 3mm . It has been shown that the crystallographic a axis is radial in PHB spherulites with b and c axes rotating about this axes (Barham et al.). The rotation of these birefringent units as they progress radially causes the well known banded appearance when observed under crossed polarisers in optical microscope (POM).
3. Pure PHB crystallized at higher temperatures showed very large spherulite superstructures, which possessed both radial and circumferential cracks. These results was contradictory to that observed by Barham et al. who observed radial cracks at lower crystallization temperatures (below T_c - 130°C)
4. Another reason for these types of cracks to occur was due to surfaces on which spherulites were grown. When stiff surfaces like glass were used, the melt just in front of growing spherulites was severely constrained by the presence of spherulites, so that a considerable negative pressure may have build up. It is possible that the resulting stress on such spherulite may be relieved by it detaching itself from the surface at which growth is occurring, thus partially accommodating the volume change on crystallization. The fact that there is considerable stress in the samples caused by the volume reduction on crystallization can often is seen by the front of bubbles near the growth front which affected the crack propagation.
5. Spherulite growth rate was influenced by crystallization temperature with increase in spherulite diameter at higher crystallization rate starting from $20\mu\text{m}$ for 25°C to 2-3 mm for 130°C .
6. Spherulite diameter was found to decrease with increase in HA filler content thereby reducing possible crack formation in the case of bigger diameter spherulites.
7. Spherulites diameter for two different HA filler varying in size, showed different nucleation behaviour. It was observed that with needle shaped particles the diameter

of spherulites was about 500 μm and that for spherical shaped nanoparticles was about 1000 μm for the same weight fraction of fillers (20 wt%). This difference was attributed for heterogeneous nucleation induced by HA, which caused more number of primary nucleation sites for crystallization. Nevertheless the spherical particles which an average diameter of about 150-200 nm caused lesser nucleation sites per unit area than that of needle particles.

8. The nonisothermal melt-crystallization exotherms for PHB/HA & PHBHV/HA nanocomposites containing 10 and 20 wt% of HA and varying filler size and shape, at five cooling rates (Φ) were analyzed. For a given value of Φ , all T_p values for the PHB/HA & PHBHV/HA nanocomposites are consistently higher than those for pure systems irrespective of filler size, suggesting that the addition of HA promotes the heterogeneous nucleation thereby reducing the spherulite diameter.
9. Mechanical behaviour of PHB/HA and PHBHV/HA nanocomposite with different filler size showed different behaviour. For PHB/HA with needle particles, the yield stress increased with increase in filler content without much compromise in % elongation as compared to pure system. Whereas in spherical particles, only yield stress was increased with decrease in % elongation as the filler content increased. This was due to
 1. The size of spherulites were bigger in spherical HA filled systems than with needle filled HA.
 2. Interparticle distance between the filler particles varied.
10. Microhardness of nanocomposites of PHB/HA and PHBHV/HA filled with both type of fillers showed an increase in hardness with increasing filler content. Dependence was linear and followed additivity law. Spherical filled systems showed higher hardness than that of needles with a same filler content. Large area of fillers could act as surface coating on polymer matrix and can prevent direct contact of indenter on to the matrix and may press the soft matrix rather than plastically deforming it.
11. Micromechanical deformation behaviour of PHB/HA nanocomposites filled with two different nanoparticles showed modified crazing mechanism. Nanoneedles with low interparticle distance and with multiple fibrillation process resulted in enhanced toughness as compared to that of spherical filled particles.
12. Contact angle measurement on solution cast PHB/HA and PHBHV/HA nanocomposites showed decreasing (θ) value with addition of fillers thereby enhancing surface hydrophilicity without treating with chemical moieties.

13. Cell culture performed on these systems using MG-63 & primary osteoblasts showed enhanced cell activity on these substrates. Addition of HA showed improvement of cell density over the substrates and they formed confluent monolayer within 3-7 days of cell culture.
14. Immunohistological analysis on these substrates expressed collagen type I and this trend increased with increase in HA in the matrix.
15. Porous substrates prepared from these nanocomposites using different fabrication techniques showed a varied range of pores just convenient for different type of cell-substrate mechanisms
 - a) Immersion Precipitation- Pore size (8-10 μ m)- Open pores
 - b) Freeze drying (low grain templates)- Pore size (60-100 μ m)- Interconnected pores
 - c) Freeze drying (large grain templates)- Pore size (300-350 μ m)- Interconnected pores
 - d) Melt infiltration (sugar templates)- Pore size (250-350 μ m)- Interconnected pores
16. Electrospun nanofibers prepared from PHB and PHBHV with different filler ratios had uniform morphology with fiber diameter ranging from 300-700 nm. More over the filler orientation was uniform without much aggregation, with the filler particles oriented towards spinning direction. It was observed that the fiber diameter of spherical filled systems was consistently higher than that of nanoneedle filled systems.
17. Aligned nanofibers were effectively produced from parallel plate electrodes. The distance between plates was varied and it was found that, with increasing plate distance, the fibers sagged down due to their own weight. Distance of 2 and 4 cms was optimum.
18. Nanoparticles were effectively synthesized by wet-chemical method and micro-emulsion technique.
19. Finally, keeping in mind different applications of tissue engineering, PHB/HA nanocomposites are fabricated to different structures (compact structures, foamed structure and electrospun fibers) using different techniques. These structures can be used for different applications in tissue engineering (Figure 81) (BTE) and can be used as a tool kit.



Figure 81: Implants from PHB/HA composites for tissue engineering applications a) compact structures, b) porous 3-D structures and c) Sandwich structure of membrane and electrospun ma

6. References

- [1] Lakes Roderic. Materials with structural hierarchy. *Nature* 1993;361(6412):511-515.
- [2] Hartgerink Jeffrey D., Beniash Elia, Stupp Samuel I. Self-Assembly and Mineralization of Peptide-Amphiphile Nanofibers. *Science* 2001 November 23, 2001;294(5547):1684-1688.
- [3] Biddlestone F., Harris A., Hay J. N., Hammond T. The physical ageing of amorphous poly(hydroxybutyrate). *Polymer International* 1996;39(3):221-229.
- [4] de Koning G. J. M., Scheeren A. H. C., Lemstra P. J., Peeters M., Reynaers H. Crystallization phenomena in bacterial poly[(R)-3-hydroxybutyrate]: 3. Toughening via texture changes. *Polymer* 1994;35(21):4598-4605.
- [5] Scandola M., Pizzoli M., Ceccorulli G., Cesàro A., Paolletti S., Navarini L. Viscoelastic and thermal properties of bacterial poly(d-[β]-hydroxybutyrate). *International Journal of Biological Macromolecules* 1988;10(6):373-377.
- [6] Daculsi G., Weiss P., Bouler J. M., Gauthier O., Millot F., Aguado E. Biphasic calcium phosphate/hydrosoluble polymer composites: a new concept for bone and dental substitution biomaterials. *Bone* 1999;25(2, Supplement 1):59S-61S.
- [7] De Aza P. N., Guitián F., De Aza S. Bioeutectic: a new ceramic material for human bone replacement. *Biomaterials* 1997;18(19):1285-1291.
- [8] Dorozhkin Sergey V. Bioceramics of calcium orthophosphates. *Biomaterials*;In Press, Corrected Proof.
- [9] Ducheyne P., Qiu Q. Bioactive ceramics: the effect of surface reactivity on bone formation and bone cell function. *Biomaterials* 1999;20(23-24):2287-2303.
- [10] Frayssinet P., Trouillet J. L., Rouquet N., Azimus E., Autefage A. Osseointegration of macroporous calcium phosphate ceramics having a different chemical composition. *Biomaterials* 1993;14(6):423-429.
- [11] Hayashi K., Matsuguchi N., Uenoyama K., Sugioka Y. Re-evaluation of the biocompatibility of bioinert ceramics in vivo. *Biomaterials* 1992;13(4):195-200.
- [12] Hench L. L. Bioceramics: from concept to clinic. *J Am Ceram Soc* 1991;74:1487–1510.
- [13] Hotz G., Herr G. Bone substitute with osteoinductive biomaterials -- Current and future clinical applications. *International Journal of Oral and Maxillofacial Surgery* 1994;23(6, Part 2):413-417.

- [14] Kalita Samar J., Bhardwaj Abhilasha, Bhatt Himesh A. Nanocrystalline calcium phosphate ceramics in biomedical engineering. *Materials Science and Engineering: C* 2007;27(3):441-449.
- [15] Kim H. M. Ceramic bioactivity and related biomimetic strategy. *Current Opinion in Solid State and Materials Science* 2003/10//;7(4-5):289-299.
- [16] Klein Christel, de Groot Klaas, Chen Weiqun, Li Yubao, Zhang Xingdong. Osseous substance formation induced in porous calcium phosphate ceramics in soft tissues. *Biomaterials* 1994;15(1):31-34.
- [17] Miao X., Tan L. P., Tan L. S., Huang X. Porous calcium phosphate ceramics modified with PLGA-bioactive glass. *Materials Science and Engineering: C* 2007;27(2):274-279.
- [18] Chevalier J., Gremillard L. Ceramics for medical applications: A picture for the next 20 years. *Journal of the European Ceramic Society* 2009;29(7):1245-1255.
- [19] Gerber C., Lang, H.P. How the doors to the nanoworld were opened ? *Nature Nanotech* 2006;1(3-5).
- [20] Vaia R.A., Wagner, H.D. Polymer nanocomposites: framework for the future. *Materials Today* 2004;11:32-37.
- [21] Jordan Jeffrey, Jacob Karl I., Tannenbaum Rina, Sharaf Mohammed A., Jasiuk Iwona. Experimental trends in polymer nanocomposites--a review. *Materials Science and Engineering A* 2005;393(1-2):1-11.
- [22] Bancroft GN Mikos AG. Bone tissue engineering by cell transplantation In: Ikada Y, Oshima N (eds) *Tissue engineering for therapeutic use*. Elsevier, New York 2001:151.
- [23] Michler G. H. *Kunststoff-Mikromechanik- Morphologie, Deformationen und Bruchmechanismen*: Hanser Verlag, 1992.
- [24] Ishaug-Riley SL Crane-Kruger GM, Yaszemski MJ, Mikos AG. Three-dimensional culture of rat calvarial osteoblasts in porous biodegradable polymers. *Biomaterials* 1998;19:1405–1412.
- [25] Shea LD Wang D, Franceschi RT, Mooney DJ. Engineered bone development from a pre-osteoblast cell line on three-dimensional scaffolds. *Tissue Eng* 2000;6:605–617.
- [26] Connolly JF Guse R, Tiedeman J, Dehne R. Autologous marrow injection as a substitute for operative grafting of tibial nonunions. *Clin Orthop Relat Res* 1991;266:259-270.
- [27] Mark Richards, Barbara A. Huibregtse, Arnold I. Caplan, James A. Goulet, Steven A. Goldstein. Marrow-derived progenitor cell injections enhance new bone formation during distraction. *Journal of Orthopaedic Research* 1999;17(6):900-908.

- [28] Takafumi Yoshikawa, Hajime Ohgushi, Susumu Tamai. Immediate bone forming capability of prefabricated osteogenic hydroxyapatite. *Journal of Biomedical Materials Research* 1996;32(3):481-492.
- [29] Breitbart Arnold S., Grande Daniel A., Mason James M. Tissue engineering and gene therapy in facial plastic surgery. *Current Opinion in Otolaryngology & Head and Neck Surgery* 1998;6(4):226-231.
- [30] Hutmacher Dietmar W. Scaffolds in tissue engineering bone and cartilage. *Biomaterials* 2000;21:2529-2543.
- [31] Murugan R., Ramakrishna S. Nanoengineered Biomimetic Bone-Building Blocks. *Molecular Building Blocks for Nanotechnology*, 2007. p. 301-352.
- [32] R Mowlem. Cancellous chip bone-grafts. Report on 75 cases. *Lancet* 1944;1:746-748.
- [33] Macewen William. The Role of the Various Elements in the Development and Regeneration of Bone. *Proc R Soc Lond B*;doi:10.1098/rspb.1907.0034.
- [34] Stevenson S., Horowitz M. The response to bone allografts. *J Bone Joint Surg Am* 1992 July 1, 1992;74(6):939-950.
- [35] Centres for, Disease, Control. Epidemiologic Notes and Reports Transmission of HIV Through Bone Transplantation: Case Report and Public Health Recommendations Morbidity and Mortality *Weekly Reports* 1988;37:597-599.
- [36] Meek'ren J. Heel- en geneeskunstige aanmerkingen. Posthumous publication; Amsterdam, Casparus Commelijn 1668.
- [37] Van de Putte KA Urist MR. Experimental mineralization of collagen sponge and decalcified bone. *Clin Orthop Rel Res* 1965;40:48-56.
- [38] Urist MR Dawson E. Intertransverse process fusion with the aid of chemosterilized autolyzed antigen-extracted allogeneic (AAA) bone. *Clin Orthop Rel Res* 1980;154:97-113.
- [39] MP Bostrom. An unexpected outcome during testing of commercially available demineralized bone graft materials: How safe are the nonallograft components? *Spine* 2001;26:1425-1427.
- [40] Niinomi Mitsuo. Recent metallic materials for biomedical applications. *Metallurgical and Materials Transactions A* 2002;33(3):477-486.
- [41] Brune Dag, Hultquist Gunnar. Corrosion of a stainless steel with low nickel content under static conditions. *Biomaterials* 1985;6(4):265-268.
- [42] Hildebrand Hartmut F., Veron Christian, Martin Pierre. Nickel, chromium, cobalt dental alloys and allergic reactions: an overview. *Biomaterials* 1989;10(8):545-548.

- [43] Reclaru L., Lüthy H., Ziegenhagen R., Eschler P. Y., Blatter A. Anisotropy of nickel release and corrosion in austenitic stainless steels. *Acta Biomaterialia* 2008;4(3):680-685.
- [44] Schriver William R., Shereff Richard H., Domnitz Jeffrey M., Swintak Edward F., Civjan Simon. Allergic response to stainless steel wire. *Oral Surgery, Oral Medicine, Oral Pathology* 1976;42(5):578-581.
- [45] Mölders M., Fischer A., Wiemann M. Biocompatibility of a nickel-free austenitic steel assayed by osteoblastic MC3T3-E1 cells. *Materialwissenschaft und Werkstofftechnik* 2002;33(12):775-778.
- [46] Bernard N. Stulberg, Katharine Merritt, Thomas W. Bauer. Metallic wear debris in metal-backed patellar failure. *Journal of Applied Biomaterials* 1994;5(1):9-16.
- [47] Pohler Ortrun E. M. Unalloyed titanium for implants in bone surgery Reintitan für Implantate in der Knochenchirurgie Le titane pour les implants osseux Titanio para implantes en cirugía ósea. *Injury* 2000;31(Supplement 4):D7-D13.
- [48] DeGarmo PE. *Materials and processes in manufacturing*. 5th ed New York: Collin Macmillan 1979.
- [49] Saris NEL. Magnesium: an update on physiological, clinical and analytical aspects. *Clin Chim Acta* 2000;294:1-26.
- [50] Vormann J. Magnesium: nutrition and metabolism. *Mol Aspects Med* 2003;24:27-37.
- [51] Lewandrowski Kai-Uwe, D. Gresser Joseph, Wise Donald L., Trantolo Debra J. Bioresorbable bone graft substitutes of different osteoconductivities: a histologic evaluation of osteointegration of poly(propylene glycol-co-fumaric acid)-based cement implants in rats. *Biomaterials* 2000;21(8):757-764.
- [52] Mark P. Staiger Alexis M. Pietak, Jerawala Huadmai, George Dias. Magnesium and its alloys as orthopedic biomaterials: A review. *Biomaterials* 2006;27:1728–1734.
- [53] Hentrich RL Jr Graves GA Jr, Stein HG, and Bajpai PK. An evaluation of inert and resorbable ceramics for future clinical applications. *J Biomed Mater Res* 1971;5:25–51.
- [54] Park JB., Lakes, RS. *Biomaterials: An Introduction* 2nd edition, Plenum Press, New York Biomaterials 1992.
- [55] Hench L. L., Splinter, R. J., Allen, W. C. & Greenlee Jr, T. K. Bonding mechanism at interface of ceramic prosthetic materials. *J Biomed Mater Res Symp* 1971;2:117–141.
- [56] Navarro M, Michiardi, A, Castaño, O, Planell J.A. Biomaterials in orthopaedics. *J R Soc Interface* 2008;5:1137-1158.

- [57] Villiermaux F. Zirconia–alumina as the new generation of ceramic–ceramic THP: wear performance evaluation including extreme life conditions. In Transactions of the Sixth World Biomaterials Congress, Society for Biomaterials 2000.
- [58] Oonishi H. Orthopaedic applications of hydroxyapatite. *Biomaterials* 1991;12(2):171-178.
- [59] Klein Christel P. A. T., de Blicck-Hogemrst J. M. A., Wolket J. G. C., de Groot K. Studies of the solubility of different calcium phosphate ceramic particles in vitro. *Biomaterials* 1990;11(7):509-512.
- [60] Kuhne JH Bartl R, Frisch B, Hammer C, Jansson V, Zimmer M. Bone formation in coralline hydroxyapatite—effects of pore size studied in rabbits. *Acta Orthop Scand* 1994;65(3):246-252.
- [61] Holmes R Mooney V, Bucholz R, and Tencer A. A coralline hydroxyapatite bone graft substitute. *Clin Orthopaed Related Res* 1984;188:252–262.
- [62] Khavari F Bajpai PK Coralline-sulfate bone substitutes. *Biomed Sci Instrum* 1993:65-69.
- [63] Guillemin G Patat J, Fournié J, Chetail M. The use of coral as a bone graft substitute. *J Biomed Mater Res* 1987;21:557-567.
- [64] Kokubo T. & Takadama, H. How useful is SBF in predicting in vivo bone bioactivity? *Biomaterials* 2006;27:2907–2915.
- [65] Eyerer P, Ellwanger R, Federolf HA, Kurt M, Mädler H. Polyethylene. In: Williams DF, editor. Concise encyclopaedia of medical and dental materials. Oxford: Pergamon 1990:271–280.
- [66] Champion AR Saum K, Simmons W, Howard E. Enhanced ultra-high molecular weight polyethylene for orthopedics applications. In: Wise DL, et al. . *Encyclopedic Handbook of Biomaterials and Bioengineering Part B, vol1* New York: Marcel Dekker 1995:453–486.
- [67] Goldman M Gronsky R, Long GG, Pruitt L. The effects of hydrogen peroxide and sterilization on the structure of ultra high molecular weight polyethylene. *Polym Degrad Stab* 1998;62:97–104.
- [68] Rushton N Rae T. The intra-articular response to particulate carbon fiber reinforced high density polyethylene and its constituents: an experimental study in mice. *Biomaterials* 1984;5:352–356.
- [69] Saha S Pal S. Mechanical properties on bone cements: a review. *J Biomed Mater Res* 1984;18:435-462.

- [70] R Feith. Side effects of acrylic bone cement implanted to bone. *Acta Orthop Scand (Suppl)* 1975;161.
- [71] Athanasiou KA Agrawal CE, Barber FA, Burkhart SS. Orthopaedic applications for PLA, PGA biodegradable polymers. *Arthrosc: J Arthrosc Relat Surg* 1998;14(7):726-737.
- [72] Athanasiou KA Niederauer GG, Agrawal CM. Sterilization, toxicity, biocompatibility and clinical applications of polylactic acid polyglycolic acid copolymers. *Biomaterials* 1996;17:93–102.
- [73] Vert M. Bioresorbable polymers for temporary therapeutic applications. *Angewandte Makromolekulare Chemie* 1989;166(1):155-168.
- [74] S.L. Ishaug-Riely G.M. Crane, A.Gurlek, M.J.Miller, A.W.Yasko, M.J.Yaszemski, A.J.Mikos. *J Biomed Mater Res* 1997;36(1).
- [75] Scatzaker J Sanderson R, Murnaghan JP. The holding power of orthopedic screws in vivo. *Clin Orthop* 1975;108(115).
- [76] Ashammakhi N., Mäkelä E. A., Törmälä P., Waris T., Rokkanen P. Effect of self-reinforced polyglycolide membrane on osteogenesis: an experimental study in rats. *European Journal of Plastic Surgery* 2000;23(8):423-428.
- [77] Meinig RP Rahn B, Perren SM, Gogolewski S. Bone regeneration with resorbable polymeric membranes: treatment of diaphyseal bone defects in the rabbit radius with poly(L-lactide) membrane. A pilot study. *J Orthop Trauma* 1996;10:178-190.
- [78] Dunnen WFA Schakenraad JM, Zondervan GJ, Pennings AJ, van der Lei B, Robinson PH. A new PLLA/PCL copolymer for nerve regeneration. *J Mater Sci Mater Med* 1993;4:521-525.
- [79] Nakamura T Shimizu Y, Matsui T, Okumura N, Hyon SH, Nishiya K. A novel bioabsorbable monofilament surgical suture made from (ε-caprolactone, L-lactide) copolymer. In: Planck H, Dauner M, Renardy M, editors. *Degradation phenomena on polymeric biomaterials*. Springer: Berlin 1992:153-162.
- [80] Ekholm M Hietanen J, Lindqvist C, Rautavuori J, Santavirta S, Suuronen R. Histological study of tissue reactions to ε-caprolactone- lactide copolymer in paste form. *Biomater* 1999;20:1257-1262.
- [81] Wang YW Wu QO, Chen GQ. Attachment, proliferation and differentiation of osteoblasts on random biopolyester poly(3-hydroxybutyrate-co-3-hydroxyhexanoate) scaffolds. *Biomaterials* 2004;25:669–675.

- [82] Bonfield W., Gryn timer M. D., Tully A. E., Bowman J., Abram J. Hydroxyapatite reinforced polyethylene -- a mechanically compatible implant material for bone replacement. *Biomaterials* 1981;2(3):185-186.
- [83] Wang M., Joseph R., Bonfield W. Hydroxyapatite-polyethylene composites for bone substitution: effects of ceramic particle size and morphology. *Biomaterials* 1998;19(24):2357-2366.
- [84] Evans S. L., Gregson P. J. Composite technology in load-bearing orthopaedic implants. *Biomaterials* 1998;19(15):1329-1342.
- [85] Fujihara K., Huang Zheng-Ming, Ramakrishna S., Satknanantham K., Hamada H. Performance study of braided carbon/PEEK composite compression bone plates. *Biomaterials* 2003;24(15):2661-2667.
- [86] Fujihara K., Huang Zheng-Ming, Ramakrishna S., Satknanantham K., Hamada H. Feasibility of knitted carbon/PEEK composites for orthopedic bone plates. *Biomaterials* 2004;25(17):3877-3885.
- [87] Beals N. B., McDowell D. L., Spector M. Fatigue behaviour of porous polysulphone surface coatings for orthopaedic applications. *International Journal of Fatigue* 1987;9(4):211-216.
- [88] Brooks R. A., Jones E., Storer A., Rushton N. Biological evaluation of carbon-fibre-reinforced polybutyleneterephthalate (CFRPBT) employed in a novel acetabular cup. *Biomaterials* 2004;25(17):3429-3438.
- [89] Brandwood A., Noble Kathryn R., Schindhelm K. Phagocytosis of carbon particles by macrophages In vitro. *Biomaterials* 1992;13(9):646-648.
- [90] McKenna G. B., Bradley G. W., Dunn H. K., Statton W. O. Mechanical properties of some fibre reinforced polymer composites after implantation as fracture fixation plates. *Biomaterials* 1980;1(4):189-192.
- [91] Cochran G. V. B., Palmieri V. R., Zickel R. E. Aramid-epoxy composite internal fixation plates: a pilot study. *Clinical Biomechanics* 1994;9(5):315-322.
- [92] Bradley J. S., Hastings G. W., Johnson-Nurse C. Carbon fibre reinforced epoxy as a high strength, low modulus material for internal fixation plates. *Biomaterials* 1980;1(1):38-40.
- [93] Kokubo Tadashi. Bioactive glass ceramics: properties and applications. *Biomaterials* 1991;12(2):155-163.
- [94] Matsuda T., Davies J. E. The in vitro response of osteoblasts to bioactive glass. *Biomaterials* 1987;8(4):275-284.

- [95] Di Silvio L., Dalby M. J., Bonfield W. Osteoblast behaviour on HA/PE composite surfaces with different HA volumes. *Biomaterials* 2002;23(1):101-107.
- [96] Rawlings Rees D. Bioactive glasses and glass-ceramics. *Clinical Materials* 1993;14(2):155-179.
- [97] Sanderson P. J. Infection in orthopaedic implants. *Journal of Hospital Infection* 1991;18(Supplement 1):367-375.
- [98] Freed Lisa E., Vunjak-Novakovic Gordana, Biron Robert J., Eagles Dana B., Lesnoy Daniel C., Barlow Sandra K., et al. Biodegradable Polymer Scaffolds for Tissue Engineering. *Nat Biotech* 1994;12(7):689-693.
- [99] Hutmacher Dietmar W. Scaffolds in tissue engineering bone and cartilage. *Biomaterials* 2000;21(24):2529-2543.
- [100] Ranucci Colette S., Kumar Ajay, Batra Surendra P., Moghe Prabhas V. Control of hepatocyte function on collagen foams: sizing matrix pores toward selective induction of 2-D and 3-D cellular morphogenesis. *Biomaterials* 2000;21(8):783-793.
- [101] Aubert J. H., Clough R. L. Low-density, microcellular polystyrene foams. *Polymer* 1985;26(13):2047-2054.
- [102] Ch Schugens, Maquet V., Ch Grandfils, Jerome R., Ph Teyssie. Polylactide macroporous biodegradable implants for cell transplantation. II. Preparation of polylactide foams by liquid-liquid phase separation. *Journal of Biomedical Materials Research* 1996;30(4):449-461.
- [103] Schugens Ch, Maquet V., Grandfils C., Jerome R., Teyssie Ph. Biodegradable and macroporous polylactide implants for cell transplantation: 1. Preparation of macroporous polylactide supports by solid-liquid phase separation. *Polymer* 1996;37(6):1027-1038.
- [104] Ruiyun Zhang, Peter X. Ma. Poly(alpha-hydroxyl acids)/hydroxyapatite porous composites for bone-tissue engineering. I. Preparation and morphology. *Journal of Biomedical Materials Research* 1999;44(4):446-455.
- [105] Gogolewski S., Pennings A. J. Resorbable materials of poly(L-lactide). *Colloid & Polymer Science* 1983;261(6):477-484.
- [106] Yoon Sung Nam, Jun Jin Yoon, Tae Gwan Park. A novel fabrication method of macroporous biodegradable polymer scaffolds using gas foaming salt as a porogen additive. *Journal of Biomedical Materials Research* 2000;53(1):1-7.
- [107] Lam K. H., Nieuwenhuis P., Molenaar I., Esselbrugge H., Feijen J., Dijkstra P. J., et al. Biodegradation of porous versus non-porous poly(L-lactic acid) films. *Journal of Materials Science: Materials in Medicine* 1994;5(4):181-189.

- [108] de Groot J. H., Nijenhuis A. J., Bruin P., Pennings A. J., Veth R. P. H., Klompmaker J., et al. Use of porous biodegradable polymer implants in meniscus reconstruction. 1) Preparation of porous biodegradable polyurethanes for the reconstruction of meniscus lesions. *Colloid & Polymer Science* 1990;268(12):1073-1081.
- [109] Holy CE Shoichet MS, Davies JE. Biodegradable polymer scaffold. PCT;WO 99/25391,1999.
- [110] Donggang Yao, Aaron Smith, Pratapkumar Nagarajan, Adrian Vasquez, Loan Dang, Chaudhry G. Rasul. Fabrication of polycaprolactone scaffolds using a sacrificial compression-molding process. *Journal of Biomedical Materials Research Part B: Applied Biomaterials* 2006;77B(2):287-295.
- [111] Georg. H. Michler. *Electron Microscopy of Polymers*. Springer Laboratory Manuals in Polymer Science 2008.
- [112] Steinbüchel Alexander, Füchtenbusch Bernd. Bacterial and other biological systems for polyester production. *Trends in Biotechnology* 1998;16(10):419-427.
- [113] Brandl Helmut, Gross Richard, Lenz Robert, Fuller R. Plastics from bacteria and for bacteria: Poly(β -hydroxyalkanoates) as natural, biocompatible, and biodegradable polyesters. *Microbial Bioproducts*, 1990. p. 77-93.
- [114] Sudesh K., Abe H., Doi Y. Synthesis, structure and properties of polyhydroxyalkanoates: biological polyesters. *Prog Polym Sci* 2000;25(10):1503-1555.
- [115] Khanna Shilpi, Srivastava Ashok. Repeated Batch Cultivation of *Ralstonia eutropha* for Poly (β -hydroxybutyrate) Production. *Biotechnology Letters* 2005;27(18):1401-1403.
- [116] Braunegg G., Bogensberger B. Zur Kinetik des Wachstums und der Speicherung von Poly-D(-)-3-hydroxybuttersäure bei *Alcaligenes latus*. *Acta Biotechnologica* 1985;5(4):339-345.
- [117] Senior P. J., Dawes E. A. The regulation of poly-beta-hydroxybutyrate metabolism in *Azotobacter beijerinckii*. *Biochem J* 1973 May;134(1):225-238.
- [118] Anderson A. J., Dawes E. A. Occurrence, metabolism, metabolic role, and industrial uses of bacterial polyhydroxyalkanoates. *Microbiol Rev* 1990 Dec;54(4):450-472.
- [119] Lemoigne M. Etudes sur l'autolyse microbienne. Origine de l'acide β -oxy-butyrrique forme par autolyse. *Anninstpasteur* 1927;41:148-165.
- [120] Manfred Zinn , Bernard Witholt, Thomas Egli. Occurrence, synthesis and medical application of bacterial polyhydroxyalkanoate. *Advanced Drug Delivery Reviews* 2001;53:5-21.

- [121] Wallen Lowell L., Rohwedder William K. Poly-.beta.-hydroxyalkanoate from activated sludge. *Environmental Science & Technology* 1974;8(6):576-579.
- [122] Engelberg Israel, Kohn Joachim. Physico-mechanical properties of degradable polymers used in medical applications: A comparative study. *Biomaterials* 1991;12(3):292-304.
- [123] Pouton Colin W., Akhtar Saghir. Biosynthetic polyhydroxyalkanoates and their potential in drug delivery. *Advanced Drug Delivery Reviews* 1996;18(2):133-162.
- [124] Barnard Glenn N., Sanders Jeremy K. M. Observation of mobile poly([beta]-hydroxybutyrate) in the storage granules of *Methylobacterium* AM1 by in vivo ¹³C-NMR spectroscopy. *FEBS Letters* 1988;231(1):16-18.
- [125] Poirier Yves, Nawrath Christianae, Somerville Chris. Production of Polyhydroxyalkanoates, a Family of Biodegradable Plastics and Elastomers, in Bacteria and Plants. *Nat Biotech* 1995;13(2):142-150.
- [126] Jarcho M. Calcium phosphates ceramics as hard tissues prosthetics. *Clin Orthop Relat Res* 1981;157:259–278.
- [127] Aoki H. *Medical Applications of Hydroxyapatite*. Tokyo: Ishiyaku EuroAmerica 1994.
- [128] Murugan R, Ramakrishna, S. Nanostructured biomaterials. In: Nalwa, H.S., Ed. *Encyclopedia of Nanoscience and Nanotechnology*. California: American Scientific 2004;7:595–613.
- [129] Black J, Hastings, G.W. *Handbook of Biomaterials Properties*. London: Chapman and Hall 1998.
- [130] De Groot K. In: Yamamuro, T. and Hench, L.L., Eds. *Chemistry of Calcium Phosphates*. Boca Raton, FL: CRC 1990.
- [131] Kay M.I., Young, R.A., Posner, A.S. Crystal structure of hydroxyapatite. *Nature* 1964;204:1050-1052.
- [132] Werner. Gerhard's Grundr 1786:281.
- [133] Daubree A. *Comp Rend Acad Sci, Paris* 1851;32:625.
- [134] Murugan R., Ramakrishna S. Aqueous mediated synthesis of bioresorbable nanocrystalline hydroxyapatite. *Journal of Crystal Growth* 2005;274(1-2):209-213.
- [135] Li Zirong, Li Xueliang, Zhang Xiaoxi, Qian Yitai. Hydrothermal synthesis and characterization of novel flower-like zinc-doped SnO₂ nanocrystals. *Journal of Crystal Growth* 2006;291(1):258-261.

- [136] Chen Chun-Wei, Riman Richard E., TenHuisen Kevor S., Brown Kelly. Mechanochemical-hydrothermal synthesis of hydroxyapatite from nonionic surfactant emulsion precursors. *Journal of Crystal Growth* 2004;270(3-4):615-623.
- [137] Yeong K. C. B., Wang J., Ng S. C. Mechanochemical synthesis of nanocrystalline hydroxyapatite from CaO and CaHPO₄. *Biomaterials* 2001;22(20):2705-2712.
- [138] Bhaskaran K. A., Roth P. The shock tube as wave reactor for kinetic studies and material systems. *Progress in Energy and Combustion Science* 2002;28(2):151-192.
- [139] Sampath Kumar T. S., Manjubala I., Gunasekaran J. Synthesis of carbonated calcium phosphate ceramics using microwave irradiation. *Biomaterials* 2000;21(16):1623-1629.
- [140] Morgan E. F., Bayraktar, H. H. & Keaveny, T. M. Trabecular bone modulus–density relationships depend on anatomic site. *J Biomech* 2003;36:897–904.
- [141] Jae-Young Rho Liisa Kuhn-Spearing , Peter Zioupos. Mechanical properties and the hierarchical structure of bone. *Medical Engineering & Physics* 1998;20:92-102.
- [142] S. Henning; R., Adhikari;, G.H. Michler; P. Seidel; B. Sandner; A. Bernstein; H.-J. Hein. . Analysis of the bone-implant interface of a partially resorbable bone cement by scanning electron and scanning force microscopy G Bischoff and H-J Hein (eds): *Micro- and nanostructures in biological systems*; Shaker, Aachen 2001:109-120.
- [143] Bullough P. *Atlas of orthopaedic pathology*. New York: Gower Medical Publishing 1992.
- [144] Luo J. J., Daniel, I.M. Characterization and Modeling of Mechanical Behavior of Polymer/Clay Nanocomposites. *Compos Sci Technol* 2003;63(11):1607–1616.
- [145] Park C., Park, O., Lim, J. Kim, H. The Fabrication of Syndiotactic Polystyrene/Organophilic Clay Nanocomposites and Their Properties. *Polymer* 2001;42:7465–7475.
- [146] Thostenson E., Li, C.,Chou, T. Review Nanocomposites in Context. *Journal of Composites Science & Technology*;65:491–516.
- [147] Holliday L. *Composite Materials*. New York: Elsevier 1966.
- [148] Bonfield W., Grynblas, M.D., Tully, A.E., Bowman, J., and Abram, J. Hydroxyapatite reinforced polyethylene: A mechanically compatible implant material for bone replacement. *Biomaterials* 1981;2:185-186.
- [149] Bonfield W., Doyle, C., and Tanner, K.E. In: Cristel, P., Meunier, A., and Lee, A.J.C., Eds. *Biological and Biomechanical Performance of Biomaterials*. Amsterdam: Elsevier 1986:p. 153.

- [150] TenHuisen K.S., Martin, R.I., Klimkiewicz, M., and Brown, P.W. Formation and properties of a synthetic bone composite: Hydroxyapatite-collagen. *J Biomed Mater Res* 1995;29(803-810).
- [151] G. Larsen R. Velarde-Ortiz, K. Minchow, A. Barrero, I.G. Loscertales. A method for making inorganic and hybrid (organic/inorganic) fibers and vesicles with diameters in the submicrometer and micrometer range via sol-gel chemistry and electrically forced liquid jets. *J Am Chem Soc* 2003;125:1154-1155.
- [152] Li Dan, Xia Younan. Fabrication of Titania Nanofibers by Electrospinning. *Nano Letters* 2003;3(4):555-560.
- [153] Li P., Ohtsuki C., Kokubo T., Nakanishi K., Soga N., Nakamura T., et al. Process of formation of bone-like apatite layer on silica gel. *Journal of Materials Science: Materials in Medicine* 1993;4(2):127-131.
- [154] Wadcharawadee Noohom, et al. Understanding the roles of nanoparticle dispersion and polymer crystallinity in controlling the mechanical properties of HA/PHBV nanocomposites. *Biomedical Materials* 2009;4(1):015003.
- [155] Li D., Neumann A. W. A reformulation of the equation of state for interfacial tensions. *Journal of Colloid and Interface Science* 1990;137(1):304-307.
- [156] Grundke K Bogumil T, Gietzelt J, Jacobash H.J, Kwok D.Y, Neumann A.W. *Progress in colloid & Polym Sci* 1996;Steinkopf Verlag, Darmstadt:1-11.
- [157]] Girifalco L.A Good, R.J. *J Phys Chem* 1957;61:904-909.
- [158] Ge Yuebin, Chen Dawei, Xie Liping, Zhang Rongqing. Enhancing Effect of Daidzein on the Differentiation and Mineralization in Mouse Osteoblast-like MC3T3-E1 Cells. *Yakugaku Zasshi* 2006;126(8):651-656.
- [159] Kim Hae-Won, Kim Hyoun-Ee, Salih Vehid. Stimulation of osteoblast responses to biomimetic nanocomposites of gelatin-hydroxyapatite for tissue engineering scaffolds. *Biomaterials* 2005;26(25):5221-5230.
- [160] Lincks J., Boyan B. D., Blanchard C. R., Lohmann C. H., Liu Y., Cochran D. L., et al. Response of MG63 osteoblast-like cells to titanium and titanium alloy is dependent on surface roughness and composition. *Biomaterials* 1998;19(23):2219-2232.
- [161] Price RL Gutwein LG, Kaledin L. Osteoblast function on nanophase alumina materials: influence of chemistry, phase and topography. *J Biomed Mater Res*;67A:1284-1293.
- [162] Barham P.J., Keller, A. Otun, E.L, Holmes,P.A. Crystallization and Morphology of Bacterial Thermoplastic: Poly-3-hydroxybutyrate. *J Mater Sci* 1984;19:2781-2794.

- [163] Schultz J.M. . Transient effects in crystallization of polyethylene. J Polym Sci-Polym Phys 1969;7:821-827.
- [164] Xu J., Guo,B.H., Zhang, Z.M, Zhou,J.J., Jiang,Y., yan,S., Li,L., Wu,Q., Chen,G.Q, Schultz,J.M. Direct AFM observation of crystal twisting and organization in Banded spherulites of chiral poly(3-hydroxybutyrate-co-3-hydroxyhexanoate) Macromolecules 2004;37:4118-4123.
- [165] Duan YX Jiang Y, Jiang SD, Li L,Yan SK, Schultz JM. Depletion-induced nonbirefringent banding in thin isotactic polystyrene thin films. Macromolecules 2004;37(24):9283-9286.
- [166] Duan YX Zhang Y, Yan SK, Schultz JM. *In situ* AFM study of the growth of banded hedritic structures in thin films of isotactic polystyrene. Polymer 2005;46:9015-9021.
- [167] Wang Zongbao, Hu Zhijun, Chen Yongzhong, Gong Yumei, Huang Haiying, He Tianbai. Rhythmic Growth-Induced Concentric Ring-Banded Structures in Poly($\hat{\mu}$ -caprolactone) Solution-Casting Films Obtained at the Slow Solvent Evaporation Rate. Macromolecules 2007;40(12):4381-4385.
- [168] Bassett DC Hodge AM. On the morphology of the melt-crystallized polyethylene. Proc R Soc Lond 1981;377(1768):25-61.
- [169] Tjong S. C. Structural and mechanical properties of polymer nanocomposites. Materials Science and Engineering: R: Reports 2006;53(3-4):73-197.
- [170] Guosheng Zhang, Deyue Yan. Crystallization kinetics and melting behavior of nylon 10,10 in nylon 10,10-montmorillonite nanocomposites. Journal of Applied Polymer Science 2003;88(9):2181-2188.
- [171] Yunchuan Xie, Demei Yu, Jie Kong, Xiaodong Fan, Wenqiang Qiao. Study on morphology, crystallization behaviors of highly filled maleated polyethylene-layered silicate nanocomposites. Journal of Applied Polymer Science 2006;100(5):4004-4011.
- [172] Cheng Chen Bin Fei, Shuwen Peng, Yugang Zhuang, Lisong Dong , Zhiliu Feng. Nonisothermal crystallization and melting behavior of poly(3-hydroxybutyrate) and maleated poly(3-hydroxybutyrate). European Polymer Journal 2002;38:1663-1670.
- [173] Avrami. Melvin. Kinetics of Phase change. II Transformation-Time relations for random distribution of nuclei. J Chem Phys 1940(8):212-224.
- [174] Jeziorny Andrzej. Parameters characterizing the kinetics of the non-isothermal crystallization of poly(ethylene terephthalate) determined by dsc. Polymer 1978;19(10):1142-1144.

- [175] Pehlivan H., Balköse D., Ülkü S., Tihminlioglu F. Characterization of pure and silver exchanged natural zeolite filled polypropylene composite films. *Composites Science and Technology* 2005;65(13):2049-2058.
- [176] Kamiya N Sakurai M, Inoue Y, Chujo R, Doi Y. *Macromolecules* 1991;24:2178.
- [177] Ozawa T. Kinetics of nonisothermal crystallization. *Polymer* 1971;12:150-158.
- [178] Papageorgiou George Z., Achilias Dimitris S., Bikiaris Dimitris N., Karayannidis George P. Crystallization kinetics and nucleation activity of filler in polypropylene/surface-treated SiO₂ nanocomposites. *Thermochimica Acta* 2005;427(1-2):117-128.
- [179] Weng Wengui, Chen Guohua, Wu Dajun. Crystallization kinetics and melting behaviors of nylon 6/foiled graphite nanocomposites. *Polymer* 2003;44(26):8119-8132.
- [180] Weibing Xu, Mingliang Ge, Pingsheng He. Nonisothermal crystallization kinetics of polypropylene/montmorillonite nanocomposites. *Journal of Polymer Science Part B: Polymer Physics* 2002;40(5):408-414.
- [181] Cannillo V., Bondioli F., Lusvardi L., Montorsi M., Avella M., Errico M. E., et al. Modeling of ceramic particles filled polymer-matrix nanocomposites. *Composites Science and Technology* 2006;66(7-8):1030-1037.
- [182] Schaefer Dale W., Justice Ryan S. How Nano Are Nanocomposites? *Macromolecules* 2007;40(24):8501-8517.
- [183] Fukuda Hiroshi, Kawata Kozo. On Young's modulus of short fibre composites. *Fibre Science and Technology* 1974;7(3):207-222.
- [184] Smallwood Hugh M. Limiting Law of the Reinforcement of Rubber. *Journal of Applied Physics* 1944;15(11):758-766.
- [185] Kausch H. H., Michler G. H. Effect of nanoparticle size and size-distribution on mechanical behavior of filled amorphous thermoplastic polymers. *J Appl Polym Sci* 2007;105(5):2577-2587.
- [186] G.H. Michler F, J, Balta Calleja Mechanical properties of polymers based on nanostructure and morphology. Boca Raton: CRC Press 2005.
- [187] Kim G. M., Michler G. H. Micromechanical deformation processes in toughened and particle filled semicrystalline polymers: Part 2. model representation for micromechanical deformation processes. *Polymer* 1998;39(23):5699-5703.
- [188] Schaefer DW Justice RS. *Macromolecules* 2007;40(24):8501-8517.
- [189] Dalby M. J., Di Silvio L., Harper E. J., Bonfield W. Increasing hydroxyapatite incorporation into poly(methylmethacrylate) cement increases osteoblast adhesion and response. *Biomaterials* 2002;23(2):569-576.

- [190] Baumgarten PK. Electrostatic spinning of acrylic microfibers. *J Colloid Interface Sci* 1971;36:71-79.
- [191] Zhang Chunxue, Yuan Xiaoyan, Wu Lili, Han Yue, Sheng Jing. Study on morphology of electrospun poly(vinyl alcohol) mats. *Eur Polym J* 2005;41(3):423-432.
- [192] Ramakrishna S.; Fujihara, K.; Teo, W.; Lim, T.; Ma, Z. *Introduction to Electrospinning and Nanofibers*. World Scientific:Singapore 2005.